1.1 Introduction

The research on electron transport in semiconductor is of fundamental importance from the point of view of understanding and developing basic physics and also to get benefit with their applications in electronic devices. Such researches help us to gain the knowledge of interesting properties and various phenomena of the semiconductor systems, for example the nature and shape of band gap, Fermi level, distribution of carriers etc. The variation of such properties with various external factors such as temperature, pressure, some external perturbation etc., which cause phenomena as transport, photoelectric effect etc. The phenomena such as conduction can be taken as the macroscopic property, whereas the cause for the transport phenomena is the various scattering mechanisms. These scattering mechanisms are microscopic property. Hence, when one has the knowledge of microphysics can easily understand the macrophysics and vice versa. Such knowledge not only helps to understand the physics of the existing devices such as transistor, Hall generators etc, but also helps to develop new efficient devices.

Transport of carriers in semiconductors be broadly classified into two categories,

1.1 (a) Classical or Bulk Transport

Classical transports in semiconductors occur without changing the wave functions and energy levels. Such transports take place in the presence of certain low perturbing fields like electric field, magnetic field, temperature gradient etc such as mobility, conductivity etc, which are easy to understand.

The study of bulk transport in compound semiconductors is important due to their applications point of view. Such as GaN, a direct and large band gap compound semiconductor is a very useful material for various electronic devices such as, short wavelength emitters, laser printers, high power and high temperature transistors etc. Due to its strong bond strength it is useful for high power devices also. But the problem of using GaN is that it is not available in a single crystal form. So it has to be grown on some substrate such as sapphire with large lattice mismatched. The mismatch causes large density of dislocations in the interfacial layer. The highly dislocated carriers also take part in various electronic and thermal transport properties of the

material. Hence such GaN grown on substrate can be considered as made up of two layers, one as the bulk GaN and the second as the dislocation layer. The detail study of it has been done in Chapter III.

1.1 (b) Quantized Low Dimensional Transport

The quantum transport is quite different from that of the classical transport due to the modification of the energy bands and the scattering probability [Roth and Argyers, 1966]. In the case of quantum transport (QT) the scattering probability depends on applied field, whereas for the classical transport it does not. The present nanoscale devices are totally base on QT phenomena, hence it helps to understand and develop the operation of the new and efficient devices [Patel and Shaw, 1970].

Quantum transport [Landau, 1930; Schieffer 1957] phenomena deal with transport parameters observed in the presence of strong external field such as electric or magnetic field or temperature gradient or a spatial variation in the crystal composition. The potential developed due to the spatial variation cannot be treated as external perturbation and therefore is taken as unperturbed states of the electron. The most important effects of strong external potential is to reduce the number of degrees of freedom and to change the continuous energy spectrum of electrons into discrete energy levels, which reduces the scattering mechanisms. Further, the quantization of the energy levels causes constrain on the degrees of freedom, due to which the efficiency of the devices highly increases.

Present technological development of crystal growth from vapor phase epitaxy was introduced in 1960, as Molecular Beam Epitaxy [MBE] [Cibert et al., 1986], Metal Organic Chemical Vapor Deposition [MOCVD] [Fujui and Saito, 1987] etc. The various crystal growth techniques made possible to reduce the size of the devices of dimensions to $10^{-8} m$ or lesser. Hence, the possibility to fabricate structures like quantum well (QW), quantum well wire (QWW) and quantum dot (QD) along with other perfect periodic structures like superlattice (SL) and multiple quantum well (MQW), made it possible to control the amount and the direction of flow of electrons according to our need. Recent publications also show that several types of QWs, QWWs and QDs have been investigated for various purposes. Such (Low dimensional device) LDDs are gaining the attention of researchers.

When two different band gap semiconductors of perfect lattice matched are arranged in such a way that the lower band gap semiconductor is sandwiched in between the higher band gap semiconductors. The carriers from higher band gap fall into the lower band gap due to the difference in the energy band offset or energy level variation. The carriers can never over come the barriers until and unless it is excited by some suitable external energy. Hence the electrons get trapped into the well. If the width of the well is of the order of the deBroglie wavelength or less, the electron motion gets quantized into various energy levels forming various energy eigen values. Hence, the motion of the carriers is restricted to move along the height of the well. The carriers can move only in the plane perpendicular to the interface of the junction or parallel to the surface of the well of the particular level. Such a structure is called quantum well (QW).

A structure called heterojuncation [Anderson, 1960] can be obtained by using low and high band gap materials, in which the electrons from higher band gap fall to the lower band gap. The carriers or electrons in the higher band gap remain uncovered near the interface, hence form the surface charges. Due to the surface charges in the higher band gap and the accumulation of charges in the lower band gap, the band bending takes place. As a result a triangular well is formed at the junction. Electrons which get trapped into the triangular well get quantized in the various energy levels. Such quantized electrons can move only in the plane of the quantized level or perpendicular to the surface of the junction.

The advantage of QW over single heterojunction is the modulation doping. The doping is possible in both sides of the QW, so that more concentration of carriers can be possible to collect into the QW.

In the year 1960, the idea of heterojunction was forwarded by Anderson. It is followed by the concept of (one dimensional electron gas) 1D EG or QWW [Sakaki, 1980], where electrons can flow only along one direction i.e one more dimension of the QW is quantized. Such 1D EG or quasi-one dimensional (Q1D) brought the concept of new devices of very high mobility. It was found much more improved in the transport parameters than two-dimensional (2D) devices or QW devices.

A similar quantization effect can be observed in the case of magnetic quantization also. In the presence of a strong magnetic field, the electrons or holes, the majority carries in a semiconductor perform an orbital motion on

the plane perpendicular to the magnetic field. The motion becomes quantized and equally spaced ladder of energy levels, called Landau levels [Landau, 1930] are formed. Thus continues energy spectrum of the electrons changes into discrete energy levels-so called energy band quantization. The charge carriers are still free to move on the direction along the magnetic field and so they behave as if they have only one dimensional motion called quasi-one dimensional (Q1D).

In simple words, we can say that two contributions to the electron energy relation are observed, i.e. the translational energy along the direction of the magnetic field and the quantized energy of cyclotron motion in the plane perpendicular to the field. It is exactly the case of the motion of carriers in the QWW.

In both the cases, QWW and Q1D systems when the magnitude of the perturbation is very high, then only one level is considered to be occupied by carries, the condition is said to be extreme quantum limit [EQL]. This condition is achieved at low temperatures depending on the effective mass of the semiconductor for magnetic quantization so that $\hbar\omega_c \rangle\rangle k_B T$ is satisfied. Where, $\hbar\omega_c$ is the cyclotron energy and $k_B T$ is the thermal energy.

The classical Boltzmann [Roth and Argyres, 1966] transport equation can be used to study the transport parameters in the longitudinal configuration under quantizing magnetic field with reasonable success. This is because the motion along the direction of the magnetic field remains unaffected. However, the Boltzmann equation cannot be applied to the transverse configuration because there is a quantization in the plane. The method usually adopted for the calculation of transverse parameters is Kubo formalism or density matrix formalism [Baker, 1972; Dworin, 1965].

The quantization of energy in one more direction of QWW or Q1D system leads the QD structure. Obviously, the transport of carriers in such system is not possible because there is quantization of energy levels in all the three directions. i.e. the motion in all three dimensions (3D) are restricted. In the magnetically confined system, when the sample is replaced by a thin film, the thickness of which is of the order of deBroglie wave length the system behaves as QD.

Such confined Q1D and QD systems can be fabricated by latest technological achievements such as MOCVD, MBE etc. These efficient technologies made it

possible to fabricate dimensionally perfect system. The structural systems formed in such a manner are called geometrically confined low dimensional systems.

On the transverse plane of magnetically confined and geometrically confined Q1D systems as well as geometrically and magnetically confined QD system the motion of carries across the quantized levels is not possible. In the case of QD the carries in such systems are localized just like atoms into their lattices. The electronic applications of such systems as nano-scale devices, like single electron transistors (SET) etc are becoming an interesting research topic.

The phenomena of photoemission and absorption are known from long time. It was observed in metal and Semiconductor of 3D. However, the studies of the phenomena in low dimensional systems are still interesting for the research point of view.

As discussed earlier, the quantization of the energy levels formed by magnetically and geometrically confinement leads the carriers to be in various quantized energy levels. When such carriers are subjected to an external photon of suitable wavelength, photoelectric emission takes place. Hence we have also included the photoelectric effect due to the quantized energy levels of Q1D and quasi-zero dimensional (Q0D) systems in our present work.

1.1 (c) Effect of Band Structures on the Transport Properties

The magnetically quantization energy dispersion relations used in Q1D system to calculate various transport parameters is not applicable in the case of narrow band gap semiconductors such as Mercury Cadmium Telluride (MCT). In MCT the interactions between s-type conduction band and p-type valence band causes the dispersion relation to be modified different from the usual parabolic band relation, as given by the equation (1.1).

For such low band gap semiconductors with magnetic quantization, the energy relation becomes [Bowers and Yafet, 1959] as given below,

$$E = -\frac{E_g}{2}\left[-\frac{E_g^2}{4} + E_g\left(\frac{\hbar\omega_c}{2} - |g|\frac{\mu_B B}{2} + \frac{\hbar^2 k_Z^2}{2m^*}\right)\right]^{1/2} \qquad \ldots (1.1)$$

Where E_g and $\hbar\omega_c$ are band gap energy and the cyclotron energy due to magnetic confinement of magnetic flux density (B) respectively. The other symbols have their usual meanings.

The nonparabolic energy dispersion relation has been obtained by Kane in the absence of magnetic field. The theory of nonparabolicity in semiconductors has also been studied in the presence of quantizing magnetic field. Furthermore, the nonparabolic dispersion relation in the presence of quantizing magnetic field has been simplified and expressed in the parabolic form by Sharma and Phakde [Phadke and Sharma, 1975]. The relation obtained by Sharma and Phadke is valid at low temperatures for narrow gap semiconductors and it has been used in the present thesis.

Recent studies of AB Chen and A Sher [Krishnamurthy and Sher, 1995] showed that the band structure of MCT is more hyperbolic in nature. Hence considering the recent trend of hyperbolic band structure we have included the hyperbolic band structure of MCT in our study.

1.1 (d) Effect of Broadening on the Transport Property

The quantized energy levels so far we have discussed is found only in the case of an ideal system, but practical real systems are found to be full of impurities and imperfections; and are quite natural also. Such impurities and imperfections increase the scattering mechanisms and are important while calculating various transport parameters.

The impurities and imperfections cause the singularity in the density of states which diverges transport parameters. To overcome this divergence in the transport parameters, the Landau level broadening due to electrons-impurity interactions has been considered. The electron-impurity interactions in semiconductors under magnetic quantization introduce the uncertainty in the energy levels leading to removal of sharpness of the energy levels. So, it causes the broadening of the Landau energy levels and makes the density of states finite at the point of singularity. The difficulties of broadening have been removed by incorporating the broadening effect. The inclusion of broadening is expected to modify the photoelectric emission (PE) current density due to enhance scattering. The effect of broadening on quantized system produced by magnetic field and spatial confinement has been studied to access the effect on the optical properties.

1.2 Scope of the Thesis

Chapter-II deals with the literature review on the electronic transport in bulk and quantized low dimensional semiconductor systems reported to past and present work.

In the beginning of the chapter, a description about bulk material and the practical limitations to grow such type of material like GaN on a substrate as sapphire is given. The probability of various types of scattering mechanisms to be present in the interface, the layer between the bulk GaN and the sapphire is also discussed.

In the next part the various techniques of quantization of energy levels such as spatial quantization, magnetic quantization and quantum size effect are discussed along with the detail study of the energy band quantization and the modification of the density of stares (DOS) due to the quantization of various dimensions, such as Q2D, Q1D and Q0D of the device system is also done.

The energy dispersion relation of low band gap materials is also highlighted.

The importance of various transport parameters are also discussed such as ac mobility, thermoelectric power etc.

Finally, the broadening of the quantized energy levels due to the presence of the impurities and imperfections in the real systems are also discussed briefly.

Chapter-III deals with low field electrical and thermal transport in lattice mismatched n-GaN grown on sapphire. GaN with band gap of 3.5V [Pankove and Moustakas, 1998] is grown on sapphire, with a band gap mismatch of 14% as well as 34% mismatch in the coefficient of thermal expansion. The mismatch causes a large amount of carriers to be collected in the interface, in between the GaN and the sapphire. Due to the density of the dislocations, being very high in the order of 10^{14} m^{-2} [Look and Sizelove, 1999], carriers also take part in various transport phenomena, which cause the transport characteristic of the materials to be highly affected. The complexity has been solved by DC Look [Look and Molnar, 1997], according to which the current passing through such GaN grown on the sapphire can be considered as two layers. Later on, the model was called two-layer model [Look and Molnar,

1997] with one layer as the bulk GaN and the second layer as the interface of GaN and sapphire

Hence in chapter III, we have carried out the study of the effect of the dislocations in the transport parameters of n-GaN grown on the sapphire. Considering the two-layer model of n-GaN grown on sapphire, we have calculated various transport parameters such as mobility, Seebeck coefficient, thermal conductivity due to electrons. The thermal conductivity due to lattice is calculated separately considering the Callaway's phenomenological theory [Callaway, 1959]. Finally, the figure of merit Z is also calculated.

We have also calculated the combined real and imaginary parts of ac mobility values of the system.

Considering various nonphonon scattering mechanisms such as ionized impurity and neutral impurity scattering mechanisms and phonon scattering mechanisms such as acoustic phonon, piezoelectric phonon via deformation potential scattering mechanisms and polar optical phonon scattering mechanism the various transport parameters mentioned above are calculated.

We have compared our results with some available experimental data and found the results satisfactory.

Chapter-IV deals with comparative studies on reduced dimensionality on the heterojunctions of GaAs/$Al_xGa_{(1-x)}As$ and $Ga_xIn_{(1-x)}As$/InP systems at low temperatures. The heterojunction is a junction formed by interfacing a perfectly matched lattice of high and low band gap materials. Due to the band gap, electrons flow from higher band gap to the lower band gap. Hence, near the interface towards the higher band gap will have space charges whereas the low band gap has accumulated charges due to which the band bending takes place. Hence a triangular well is formed near the junction, where electrons get accumulated into various quantized energy levels. The system behaves as quasi-two dimensional (Q2D) system. Such system has very high value of mobility due to the charge getting separated from the parent donor, reducing the scattering mechanisms as well as due to confinement in the direction of motion of the carriers.

Further, quantization in one more direction by reducing the length of the one more dimension of the well in the order of deBroglie wavelength makes the system to be quasi-one dimensional (Q1D).

Such systems show the further improved transport parameters such as mobility. Hence in the chapter IV, studies on the dc mobility of the Q2D and Q1D systems have been carried out.

Due to the larger applications of ac microwave mobility in the present electronic devices in communication, we have also calculated the ac mobility values of the Q2D and Q1D systems considering various nonphonon scattering mechanisms such as ionized impurity, alloy disorder (only in the case of Q2D InGaAs heterojuction) and surface roughness scattering mechanisms with phonon scattering mechanisms such as acoustic phonon and piezoelectric phonon via deformation potential scattering mechanisms.

A comparative study of ac microwave mobility between Q2D and Q1D systems has also been carried out.

Chapter-V deals with study of the effect of band structures of n-$Hg_{0.8}Cd_{0.2}Te$ (MCT), parabolic, nonparabolic and hyperbolic on various transport parameters such as mobility, conductivity, Seebeck coefficient, thermal conductivity including the thermoelectric figure of merit under magnetic quantization at low and high temperatures. For the lattice part of the thermal conductivity, the phone scatterings due to boundary scatterings [Puri and Geballe, 1966] have been taken. The effect of various nonphonon scattering mechanisms such as ionized impurity and alloy disorder scattering mechanisms and phonon scattering mechanisms, such as, acoustic phonon and piezoelectric phonon via deformation potential scatterings are also observed. In the higher temperature region, the effect of polar optical phonon scattering mechanism is also included.

The effect of degeneracy, arising due to the higher density of concentrations of carriers on the various transport parameters mentioned above are also observed. To simplify our model, the assumption of the extreme quantum limit (EQL) is taken. The variation of the above parameters with temperature and the magnetic field is also observed.

Chapter-VI deals with study of the photoemission from magnetically and geometrically confined Q1D and QD systems. QD in case of the magnetically

confined system has been done by confining the longitudinal direction by size quantization i.e. the thickness of the sample is taken to be of the order of deBroglie wavelength, called thin film. For geometrically confined system we have considered the dimension of the sample to be same as that of the magnetically confined dimension of the sample.

We have also studied the effect of broadening on the geometrically and magnetically confined systems, which arises due to the presence of impurities and imperfection. The effect of broadening on the photoemission properties in geometrically confined Q1D system and magnetically confined QD system are observed and compared with the photoemission with and without broadening.

Chapter-VII deals with the conclusions of our entire work and future scope.

References

Anderson R.L, IBM, J. Res. Dev. 4, 283 (1960).
Baker J. R., J. Phys C: Solid State Phys. 5, 1657 (1972).
Bowers R. and Yafet Y., Phys. Rev. 115, 1165 (1959).
Callaway J., Phys. Rev. 113, 1046 (1959).
Cibert J., Petroff P.M., Dolan G.J., Pearton S.J., Gossard A.C. and English J.H., Appl. Phys. Lett. 49, 1275 (1986).
Dworin L, Phys. Rev. 140 A, 1689 (1965).
Fujui T. and Saito H., Appl. Phys. Lett. 50, 824 (1987).
Krishnamurthy S. and Sher A., J. Elec. Mater. 24 641 1121 (1995).
Look D.C., Molnar R.J., Appl. Phys. Lett. 70, 3377 (1997).
Look D.C., Sizelove J.R, Phys. Rev. Lett. 82, 1237 (1999).
Landau L.D., S. Physik 64, 629 (1930).
Phadke U.P. and Sharma S., J. Phys. Chem. Sol. 36, 1 (1975).
Pankove J.I., Moustakas T.D., Gallium Nitride GaN I. edited by (Academic, New York) pp.175, (1998).
Patel C.K.N. Patel and Shaw E.D., Phys. Rev. Lett. 24, 451 (1970).
Puri S.M. and Geballe T.H., in Semiconductors and Semimetals, ed. by R.K. Willardson and A.C. Beer (Academic, New York), 1, 245 (1966).
Roth L.M. and Argyres P.N., Semiconductors and Semimetals (ed. By R.K. Willardson and AC Beer (Academic press, NY) V1, 159 (1966).
Sakaki H., Jpn. J. Appl. Phys. 19, L735 (1980).
Schrieffer J.R., Semiconductor surface Physics, ed: R.H. Kingston, ed. University of Pennsylvania Press Philadephia, 55 (1957).

2.1 Introduction

In this section, we will discuss the electronic transport properties in bulk and low dimensional systems. Low dimensional systems are formed by spatial confinement of semiconductors or due to the presence of external perturbation i.e. in presence of magnetic field, electric field, temperature gradient etc. The reported literatures in the above field are also reviewed and presented here.

Semiconductors are considered to be of two types, first one as an **elemental semiconductor** such as semiconductor of Si and Ge, having indirect band gap and the second one as **compound semiconductors** formed by combining periodic table III+V or II+VI elements such as GaN, GaAs, InP, HgCd, HgTe etc. The compound semiconductors of such type are also called **binary compound semiconductors** which are generally intrinsic in nature. Whereas, combining the compound semiconductors of suitable type forms **ternary semiconductors** such as AlGaAs, GaInAs, HgCdTe etc. They are also called **alloy semiconductors**.

The compound semiconductors are gaining the attention of researchers due to their direct band gap, which made their transport and the photoelectric properties to be very interesting. Hence, they are good for fast operating devices. In such direct band gap materials all the transport parameters such as effective mass, dielectric screening and band nonparabolicity depends strongly upon the energy gap [Nag, 1980; Rode 1975]. For indirect band gap semiconductors, neither the effective mass nor the dielectric functions are strong functions of the band gap.

2.2 Important Compound Semiconductors

The transport properties of the bulk materials such as GaN, GaAs, HgCdTe are very interesting and important.

2.2 (a) GaN

GaN is a direct and large band gap material. The band gap of GaN is of the order of $3.5\,\mathrm{eV}$ [Pankove and Moustakas, 1998]. Due to its wide band gap and strong bond strength it can be used for violet, blue and light emitting devices and for high temperature transistors. InN, band gap $1.9\,\mathrm{eV}$ and AlN, band gap $6.2\,\mathrm{eV}$ when alloyed with GaN, the band gap can be tuned. The

variation of the band gap can modify the wavelength of photoemission. Higher bond strength of GaN made it to withstand higher temperatures and it has made GaN devices processing easier. High power transistors are needed for automobile engineers.

The thermal conductivity of GaN is also good, hence, it can work in hostile environment also. GaN has high break fields of the order of $3\times10^{8}V/m$. High breakdown voltage is necessary for high power devices [Pankove, 1997].

2.2 (b) GaAs

After Si, GaAs has become one of the most important semiconductors because of band structure which is large and direct. Its larger bandgap also ensures better and high temperature performance and better radiation hardness (i.e. better immunity from α particles and γ rays). Due to its direct bandgap, it ensures excellent optical properties as well as superior electron transport in the conduction band. The conduction band edge states have an s-type symmetry of the central cell. The band edge E vs. k relation is quite isotropic leading to spherical equal energy surfaces.

It is also important that the band gap of semiconductors in general decreases as the temperature increases. The band gap of GaAs, for examples, is 1.51eV at $T=0K$ and 1.43eV at room temperatures. These changes have an importance for both electronic and optoelectronic devices. The temperature variation alters the laser frequency in solid state lasers, which alters the response of modulators and detectors. It also has effects on intrinsic carrier concentration in semiconductors. The material has high mobility suitable for high speed devices.

The main problem to use GaAs is, it does not have an oxide which could form high quality insulator-semiconductor interface and is much more difficult to process also. The basis consists of two atoms hence it is easier to introduce defects (e.g. a Ga atom on the As sublattice, the so called antisite defect).

2.2 (c) MCT

MCT is a II-VI ternary semiconductor compound comprised of the elements, mercury, cadmium and tellurium. The x mole ratio form, its chemical composition, $Hg_{(1-x)}Cd_xTe$ is defined as the ratio of $CdTe$ to $HgTe$. Hence, it

is an alloy semiconductor. Very important property of MCT is that it has an adjustable bandgap which can respond to spectra wavelength from $0.7\,\mu$m to $25\mu m$. MCT has a very narrow and direct bandgap for intrinsic operation, as it is associated with a high absorption coefficient and a moderate dielectric coefficient/index of refraction. $Hg_{0.8}Cd_{0.2}Te$ (MCT), hence it is a good applicant in various electronics and optoelectronics devices for different applications, such as infrared detectors [Shakouri and Chris, 1999]. Due to low effective mass of MCT, electrons would occupy the lowest Landau levels at a reasonable high magnetic field. Hence the mobility of MCT is very high. High mobility made it a good applicant for thermoelectric devices such as cooler, refrigerator etc.

Due to very low band gap, the band structure of MCT is nonparabolic and the nonparabolicity has been calculated by Kane's model [Phadke and Sharma, 1975].

Recent study of AB Chen and A Sher [Chen and Sher, 1982] shows that the band structure of MCT is more hyperbolic in nature rather than nonparabolic as described by Kane. The presence of magnetic field in MCT with hyperbolic band also allows us to manipulate the effective mass as required for figure of merit consideration for thermoelectric cooler.

The different transport phenomena due to its hyperbolic band structure in the presence of magnetic field are compared with that of nonparabolic and the prarabolic by some authors [Ghose, Chakrabory, Benerji and Sarkar, 2000].

2.3 Transport Properties in Bulk Semiconductors

Several techniques as molecular beam epitaxy (MBE) [Cibert et al., 1986], metal organic chemical vapor deposition (MOVCD) [Fujui and Saito, 1987] etc have been reported to use for the epitaxial growth of III-V nitride semiconductors. However, MOCVD is more suitable for high-volume production for III-V nitrides due to two main reasons as reported by Steigerwald et al. [Steigerwald et al., 1997]: higher throughput (lower cost) and demonstrated superior material quality [Steigerwald et al., 1997].

Although, the MOCVD epitaxial growth principle is simple, researchers faced several challenges in the 1980s to achieve good device-quality of nitride thin films. One of these was that ammonia is a very stable molecule, and its cracking efficiency is low. The next problem for growing III-V nitride films is

the lack of a suitable substrate that matches the lattice constant and thermal expansion coefficient of the GaN films. Heteroepitaxially grown GaN films on sapphire substrates contain high densities of structural line and planar defects. The density of dislocation ranges between 10^{12} dislocations/m^{-2} to 10^{14} dislocations/m^{-2} even after several micrometers of film growth [Ponce, 1997]. Depending on the substrate preparation, stacking faults and edge dislocations are also present near the interface with the sapphire substrate [Liliental Z. and Weber et al., 1996].

Over all, the main problem in fabricating GaN devices of *nm*-scale is to get perfect matched substrate. The presently available substrates are sapphire or Alumina (Al_2O_3) and SiC having 14% and 4% mismatch in their lattice size respectively with GaN. Due to the mismatch large amount of wells, dislocation sites, edges are created where carriers are easily accumulated. These accumulated carriers or electrons take part in various electron transport phenomena of the material. Hence, the electron transport parameters get highly affected.

The presence of electron impurities in GaN itself is an open issue for researchers. Electron concentration and Hall mobility in such undoped GaN films grown by epitaxial method have been measured from long time by several researchers. It is found that both parameters depend not only on the thickness of the buffer layers but also on the thickness of the epilayers [Look and Molnar, 1998; Goltz et al., 1998]. Magnetic field dependent Hall effect measurement has been done to determine the parameters of different layers [Saxier, 2001].

D. C. Look [Look and Molnar, 1997] put a suitable approach in this context. The author [Look and Molnar, 1997] suggested the **two-layer** model. This model assumes the low mobility, degenerate layer retains its properties in all ranges of temperature, so that the presence of interfacial layer can always be subtracted simply by knowing the properties at low enough temperature while calculating the bulk layer to be frozen out. The result was found to be very reliable for the bulk sample.

In the interfacial layer, electron transport parameters are highly affected by the presence of dislocations. Hence, some argued that the dislocation scattering may become a dominant scattering mechanism. The dislocation scattering mechanism depends on the density of dislocation and the free

carrier concentration. Dislocation scattering in n-GaN is prominent in undoped or lightly dope GaN with carrier concentration, less than $10^{24} m^{-3}$ [Choi at el., 2001]. The scattering mechanism due to dislocation was also described by Ng et al. [Ng et al., 1998]. The dislocation with an edge component introduces acceptor centers along the dislocation lines which captures electrons from the conduction band of n-GaN sample. For example, a dislocation density of $10^{14} m^{-2}$ is expected to have $2 \times 10^{23} m^{-3}$ dangling bonds along the dislocation lines. The dislocation lines become negatively charged and a space charge is formed around in which electrons are scattered and thus reduces the mobility.

The electron mobility due to scattering by dislocation is given by [Pödör B., 1966],

$$\mu_{dis} = \frac{30\sqrt{2\pi}\varepsilon^2 d^2 (k_B T)^{3/2}}{N_{dis} e^3 f^2 \lambda_d m^{1/2}} \quad \ldots(2.1)$$

where, d is the distance between acceptor centers (dangling bonds) along the dislocation line. f, N_{dis} and λ_d are the occupation rate of the acceptor centers, density of dislocation and Debye screening length respectively. Where, $\lambda_d = (\varepsilon k_B T / e^2 n)^{1/2}$ with n as net carrier concentrations.

Hence, at the lower carrier concentration regime the scattering is dominated by the dislocations. The relation (2.1) shows that the electron mobility due to scattering by dislocations should increase monotonically with net carrier concentration.

Zhu et al. [Zhu, 200] proposed the scattering model of nitrogen vacancy. Nitrogen vacancy with the lowest formation energy is believed to exist in GaN epilayer in large amounts. The exact nature of nitrogen-vacancy induced scattering potential is not known till now but roughly is assumed to be a square well potential.

Hence the mobility due to nitrogen vacancy scattering is given as,

$$\mu_{NV} = \frac{9}{16\sqrt{3}} \frac{h^4 e}{m^{*5/2}} \frac{1}{N_V} \frac{1}{U_o^2 a^6} (k_B T)^{-1/2} \quad \ldots(2.2)$$

N_V, U_o and a are Nitrogen vacancy concentration, well depth and well width respectively.

Apart from various composition ratios, growth condition, heat treatment and in homogeneity, the mobility is found to be dependent on the influence of dislocations as well as point defects.

Huang [Huang, 2002] has calculated the mobility, Hall mobility of GaN grown on sapphire with the two-layer model and compared the value with her experimental result also. Different authors [Huang, 2002,] have also calculated Hall coefficient and mobility of GaN grown on sapphire.

Huang et al. [Huang et al., 2001] theoretically calculated and also measured with experimental results of the electron transport in a freestanding GaN substrate grown by Hydride Vapor Phase Epitaxy [HVPE].

The role of dislocation scattering in the bulk n-GaN films has been observed by Ng et al. [Ng et al., 1998]

The lattice thermal conductivity of bulk n-GaN and the effects on the thermal conductivity due to dislocations have been calculated theoretically by many authors [Zou, Kotchtkov and Balandin, 2002; Kotchetkov et al., 2002; Kotchtkov, Zou and Balandin, 2001].

The thermopower investigation of n-GaN as well as p-GaN, grown by MBE along with Hall effect, conductivity and Seebeck coefficient have been carried out by Brandt et al. [Brandt et al., 1998]

2.4 Important Transport Parameters

2.4 (a) ac transport

With the development of the semiconductor devices, the generation and amplifying microwave signals in high as well as [Gunn, 1963] in low field ac transport in semiconductors is widely investigated. Prior to the development of microwave semiconductor devices, transport coefficients at microwave frequencies had been extensively studied mainly for two reasons,

The ac transport coefficients may be measured without attaching constant leads to the sample [Hambleton and Gartmer, 1959; Ramsa, Jacobs and

Brand, 1959; Dutta and Nag, 1970]. Where making ohim contact is technologically not viable, microwave methods provide a good alternative. At the same time, by using the high Q-value of microwave cavities, the sensitivities of the measuring instruments may also be much improved for microwave signals.

There are examples that the conductivity of small sized samples and the Hass mobility in low mobility samples have been conveniently measured by the microwave method [Pething and South, 1974; Sayed and Westgate, 1975]. The change in the transport coefficient at microwave frequencies give rise to interesting phenomena viz. cyclotron resonance [Dresselhaus, Kip and Kittle, 1953; Lax, Zeiger, Dexter and Rosenblum, 1954; Dexter, Zeiger and Lax, 1954; Spietzer and Fan, 1957; Lax and Wright, 1960] and change in electron susceptibility [Benedict, 1953].

The electron effective mass and the relaxation time can be accurately determined from the study of the phenomena. The high frequency conductivity in semiconductor is an important tool in obtaining information on different scattering mechanisms and band structures [Kranzer, 1971; Loschner, 1972; Nag and Dutta, 1975].

Moravec et al. [Moravec et al., 2001] have calculated galvanometric and thermoelectric parameters as Hall coefficient (R_H) and conductivity and Seebeck coefficient of undoped $p\text{-}Hg_{0.78}Cd_{0.22}Te$ at temperature range 4.2K-300K.

Small signal AC response of hot electrons in narrow-gap semiconductors in the EQL at low temperatures has also been calculated [Bahumik and Sarkar, 1992].

2.4 (b) Figure of Merit

There were number of theoretical papers published on the theory of thermo-electrics [Price, 1956; Chasmar and Stratton, 1959; Littman and Davidson, 1961; Simon, 1962 Rittner and Neumark, 1963]. Those of Price [Price, 1956] and Chasmer [Chasmar and Stratton, 1956] are note worthy. The author [Mahan, 1989] claims that he had reexamined those theories and suggested some modest changes in the analysis. According to Mahan the maximum value of the Z, depends exclusively upon two parameters, one is the energy band gap and other is the β coefficient, a combination of parameters. β

coefficient was introduced by Chasmar and Straton [Chasmar and Stratton, 1956], where $\beta = (1/k_B T)$. The authors also suggested that the best thermoelectric has a gap which is ten times the thermal energy.

When electrons flow from the material in which they have average transport energy smaller than the Fermi energy to another material in which the average transport energy is higher, they absorb thermal energy from the lattice and this will cool down the junction between the two materials [Shakouri and Bowers, 1997]

The vacuum diode thermionic generators were also proposed for refrigeration [Mahan, 1994], the efficiency of which was predicted to be over 80% of the Carnot value, but the operating temperature was still limited to greater than 500K. Shaukari et al. [Shakouri et al., 1998] proposed the thermionic emission cooling in heterostructures to overcome the limitations of vacuum thermionics at lower temperatures. With current epitaxial growth techniques as MBE or MOCVD it is possible to control the thickness of layer and composition of heterostructure. In conjunction with bandgap engineering, these techniques allow for the design of a new class of semiconductor thrmionic emission devices with improved cooling capacities [LaBounty, 2001].

2.5 Transport Properties in Quantized Semiconductor Systems

Present technological development made us able to fabricate structures that exhibit reduced dimensionality, the dimension of which are of the order of deBroglie wavelength. The studies on the reduced dimensional devices became very interesting due to their wider applications in electronics and optical devices. When the size of the devices decreases the transport in such low dimensional (LD) devices can be explained only by their energy relations and the wave function.

The lowering the dimensionality of semiconductor devices is another interesting part of a research work because LD is not only important for their applications in various electronic devices but the study on LD also helps to understand the physics of the existing devices. By knowing properties of LD devices, their utility can be made in the proper direction.

Lowering dimensionality can be done in different ways, depending on the physical processes being considered. Usually LD involve a physically defined

region of a sample with one or more dimensions small compared to an appropriate physical scale length called deBroglie wavelength.

Before talking about deBroglie wavelength, a glance in the description of transport processes is beneficial to know. Generally, in transport two physical scale lengths are particularly important. One is the **mean free path**, the average distance between successive collisions that change the direction of flow of current. In high-mobility samples this length can be of the order of micrometers or larger.

A second scale length important for transport is the **phase breaking length**, the distance in which wave function coherence is lost. At high temperatures, where phonon scattering dominates, both of these lengths are determined by the phonon scattering rate. At high carrier densities, carrier-carrier scattering may control the inelastic scattering or phase-breaking length. In such case carrier-carrier scattering affects the transport mean free path because scattering among carriers in a simple band does not change the current.

At low temperatures many transport processes depend on the inelastic scattering length, which is an average distance carriers diffuse between inelastic collisions in that dimensions.

At sufficiently low temperatures, the inelastic scattering length can be of order of 1 to 10 μ in the low-dimensionality regime for transport. Corrections to transport properties at low temperatures occur for all dimensionalities but are more pronounced in lower-dimensional systems. This subject is often called weak localizations, it has been developed in last ten years ago and has led to a large literatures. Samples with higher free path smaller than the phase breaking length are in the ballistic regime.

Fermi wavelength is $\left(2\pi/k_F\right)$. Where k_F is the carrier wave vector at the Fermi surface. When a sample dimension is comparable to this distance, also called deBroglie wavelength the motion in that direction becomes quantized. The quantization changes the energy spectrum relation and the dynamical properties of the system.

When only one dimension of the sample is small compared to this distance the system behaves like two-dimensional. Many properties of such two-dimensional systems are described in the article by Ando et al. [Ando, Fowler and Stern, 1982]. The systems constrained in more than one dimension

dynamically are one dimensional or zero-dimensional. A dynamically two, one and zero-dimensional systems are often called as quantum well (QW), quantum well wire (QWW), and quantum dot (QD) or quantum box respectively. The detail study in these systems is presented in the section **spatially quantized semiconductor systems.**

2.5 (a) Spatially Quantized Semiconductor Systems (SQSS)

One method of lowering the dimension of devices is by spatial confinement. When perfect lattice matched semiconductor of lower band gap is sandwiched between higher band gap semiconductors a rectangular quantum well (QW) is formed. Hence, the carriers are transferred into the lower band gap within the potential well. In other words, the electrons from wider and doped material are transferred themselves across the barrier to the lower and undoped material. The electrons into the well, a rectangular and quantum well get quantized and the system is called quasi-two dimensional system (Q2D). Here the wave nature of the carriers leads to the quantization of the energy levels in only one direction forming two dimensional electron gas (2D EG) as given in Fig. 2.1.

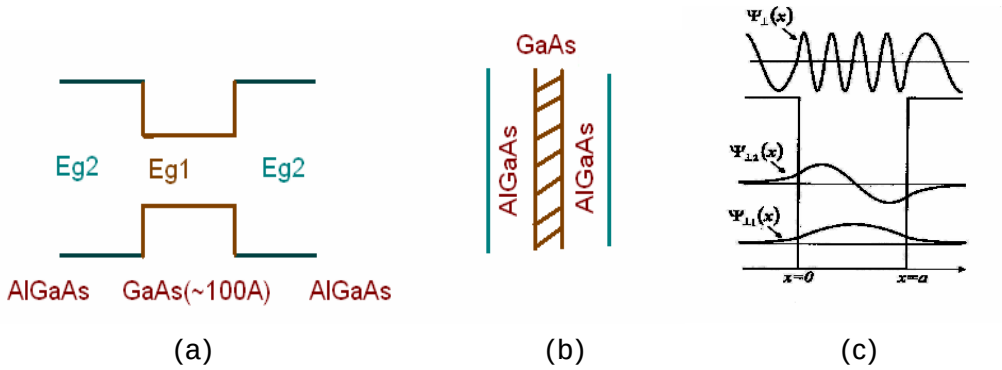

Fig. 2.1 (a) & (b) Lower band gap semiconductor is sandwiched between two higher band gap semiconductors-rectangular quantum well (QW) (c) Quantized energy levels and wave functions into the rectangular QW.

Fig. 2.1 (a) and (b) show the lower band gap semiconductor GaAs is being sandwiched between AlGaAs, doped and higher band gap semiconductor. The size of the QW is shown to be $100\,\overset{0}{\mathrm{A}}$. Fig. 2.1 (c) shows the three quantized energy levels and the corresponding wave functions into the rectangular QW.

Schrieffer [Schriffer, 1957] first anticipated the possibility of the quantized condition in the surface potential well and is verified experimentally by Fowler et al [Fowler et al., 1966].

Fig. 2.2 (a) shows the heterojunction of a lower band gap and higher band gap semiconductors. Fig. 2.2 (b) shows the two quantized energy levels into the triangular potential well formed at the heterojunction. The Fig. 2.2 (b) shows that the Fermi energy is in between the two quantized energy levels.

The shape and the size of the potential well will determine the separation of the quantized energy levels. Triangular potential well, potential of which is given as, $V(z) = eFz$ is formed at a heterojunction of different band gap materials as given in Fig. 2.2 (b).

(a) (b)

Fig. 2.2 Heterojunction (a) a junction of higher band gap and lower band gap semiconductors (b) Quantized energy levels at the heterojunction.

Like rectangular quantum well, in the case of triangular quantum well also the electrons are accumulated at the lower band gap material. Such electrons accumulated into the well create an excess of space charges that disturbs the electron distribution and causes the bending of the energy band towards the Fermi level. Whereas, in the upper band gap side the atoms are uncovered over a certain region near the junction between the semiconductors and is shown by positive sign in the Fig 2.2 (b). The uncovered atoms are ionized and form space charges due to electrons transferred into the lower band gap. Depletion charge density appears into the well which leads the band to bend into the depletion layer. The higher bending in the space-charge layer causes the charge inversion to take place. Hence almost triangular nature of the well is formed.

In the quantum mechanical calculation, the above quantum well may be rectangular or triangular the potential energy values are used in the Schrödinger equation with the appropriate modifications. The simple Schrödinger equation for rectangular quantum well of depth V_o is given as,

$$\frac{\hbar^2}{2m^*}\frac{d^2}{dz^2}\psi(z)+V_o\psi(z)=E\psi(z) \qquad \ldots(2.3)$$

Using equation (2.3) with the appropriate potential energy the wave function, representing the status of the quantized energy levels is obtained.

The properties of the 2D EG, formed into rectangular and triangular well are being utilized by the technologists to devise fast switching communication networks, for designing optical supercomputers [Solomon and Morkoc, 1984], efficient lasers [Wilt, Schwartz, Tell, Beebe and Nelson, 1984; Tsang, 1984)], detectors and a host of other modern devices. The physics of low-dimensional system is specially sensitive in the transport. Optical, thermal and magnetic properties of the 2D EG are very important in order to understand and characterize devices and for further development of their performances.

Quantum well wire (QWW) [Sakaki, 1980] is formed by trapping the electron into QW of width dimension equal to that of the deBroglie wavelength. Hence, there will be quantization in one more direction, that causes the transport to be possible only in one dimension, forming quasi-one dimensional (Q1D) structure. Such a system quantizes the energy levels of electron gas in two directions and is also called one-dimensional electron-gas (1D EG). Sakaki [Sakaki, 1980] has proposed that 1D EG could also be realized in ultrathin wires or suitably modified high electron mobility transistor (HEMT). The system promises of even higher mobility and hence provides better device possibilities than their two dimensional counterpart. Due to reduction of the scattering the various transport properties of the system is very high. Other structures like the NIPI [Dohler, 1972; Dohler, 1972], the MOSFETs and the (Junction Field effect transistor) JFETs also support the low-dimensional electron gas.

The thermoelectric power of 1D EG system at the heterojunction of AlGaAs/GaAs has been calculated by Kundu et al. [Kundu, Sarkar and Basu, 1988].

The various pairs of materials used for the fabrication of heterostructures of 2D EG and 1D EG are GaAs/$Al_xGa_{(1-x)}As$, InAs/GaSb-AlSb, PbTe/PbSnTe, InAlAs/InGaAs, InP-lattice matched alloys and other lattice matched pairs of III-V compounds. In the present thesis, however, the samples studied are mainly made of GaAs/AlGaAs and GaInAs/InP semiconducting pair because most of the practical samples used are made of these materials. GaAs has the advantage of ensuring genuine intimate contact with AlGaAs. So the pair of GaAs and AlGaAs eliminates interfacial dangling bonds leading to charge traps and recombination centers at the interface states. The growth technique of GaAs has improved greatly because of its potential to use in device fabrication. Due to very low effective mass, the mobility of GaAs is very high.

The transport properties of the charge carriers at the low dimensional semiconductor surface are interesting because such properties differ from the bulk for several reasons [Dorda, 1957] like,

- The scattering probability of charge carriers at the surface is modified by the reduced dimensionality and altered band structures,
- Free carriers drifting along the surface are subjected to boundary scattering and
- The transport of the carriers in the inversion layers can be controlled by changing the surface carrier density by an external gate field specially in the case of MOSFET. Transport studies have been carried out for both accumulation and inversion layers.

When there is further quantization in one more direction of QWW then there is no possibility of the flow of carriers or electrons means that the carriers get localized or restricted into a certain space. The system is called (Quantum Dot) QD or Quantum-zero Dimensional (Q0D) system. It means that in Q0D all 3 dimensions of the device is of deBroglie wavelength or less than that.

2.5 (a) i. Energy Band Quantization of SQSS

The confinement of the carriers in various directions causes the change in the energy dispersion relation and also the density of state (DOS) of the material. Hence, confinement causes the transport properties to vary as compared to the bulk material. In bulk semiconductors, the energy-momentum relation for electrons can be written as,

$$E_k^c = E_c + \frac{\hbar^2\left(k_x^2 + k_y^2 + k_z^2\right)}{2m^*} \qquad \ldots(2.4)$$

Where E_c is the conduction band edge and m^* is the electron effective mass. $k = \left(k_x, k_y, k_z\right)$ is the three dimensional wave vector which can have any value between $-\infty$ to $+\infty$.

In a QW electrons are confined in only one direction say Z-axis so that the confined size is less than the de-Broglie wavelength. Discrete values of energy called eigen values for electrons become,

$$E_n = \frac{\hbar^2 n^2 \pi^2}{2m^* l} \ldots \qquad \ldots(2.5)$$

Where n gives values of the quantized energy levels. Hence the energy dispersion relation for QW becomes,

$$E_{nk} = E_c + \frac{\hbar^2\left(k_x^2 + k_y^2\right)}{2m^*} + n^2 E_{0z} \qquad n = 1,2,3\ldots \qquad \ldots(2.6)$$

For the ground state energy level, with the confinement in Z-direction we take n=1 hence,

$$E_{oz} = \frac{\pi^2 \hbar^2}{2m^* L_z^2} \qquad \ldots(2.7)$$

Here, E_{oz} the zero point energy or ground state energy is the shift in the conduction band edge. The confinement considered here is due to infinite boundaries, it can be changed into finite by replacing L_z by effective thickness [Barker et al., 1991], which depends on the band gap discontinuity and is always larger than actual thickness because of leakage of the wave functions in the barrier regions. The electrons in this case behave as if they are traveling in two-dimensional surface and hence, the name quantum two dimensional electron gas (Q2D EG). If the confinement is strong, only the lowest quantized state is appreciably populated by carriers and we have quantum limit situations as in the equation (2.6) for infinite potential well. Such type of QW can be observed in modulation doped field effect transistor (MODFET), quantum well laser etc.

Similar type of confinement can be achieved in the case of heterojuncion also with triangular quantum well. In case of heterojunction, the potential in one direction is infinite and the direction opposite to that is a function of distance.

The detail study of triangular quantum well has been done by the author in section **Chapter IV**.

The repetition of the rectangular quantum well in equal interval gives a particular pattern called superlattice or multiple quantum well. Such multiple quantum well structure is obtained by growing a series of quantum wells that are separated from each other by insulating barriers. A superlattice is a special type of MQW structure where the barrier layers are made very thin so that the wave function of the electrons trapped in the adjacent potential wells over lap to some extent.

In the late 1960's, Esaki and Tsu of IBM [Esaki and Tsu, 1969] pioneered the work on superlattices (SLs). This work has led to the appearance of a new transistor made of GaAs-$Al_xGa_{(1-x)}As$, holds the record of the fastest switching devices with switching speed close to ten trillionths of a second. This device is known by various names i.e. Modulation Doped Field Effect Transistor (MODFET), High Electron Mobility Transistor (HEMT), Two-Dimensional Electron Gas FET (TEGFET) or Selectively Doped Heterojunction Transistor (SDHT). The different research groups have undertaken the study in this field in 1980.

Confinement again in one more dimension in the two dimensionally confined semiconductor leads the formation of quantum well wire (QWW), originally suggested by Sakaki [Sakaki, 1980].

Hence, the quantized energy levels in QWW is observed as,

$$E_{nk} = E_c + \frac{\hbar^2 k_x^2}{2m^*} + m^2 E_{oy} + n^2 E_{oz} \qquad m,n = 1,2,3... \qquad ...(2.8)$$

where E_{oy} is same as E_{oz} except that L_z is replaced by effective L_y. Electrons confined in QWW are predicted to have very high mobility due to reduction of the scattering mechanisms and confinement of the energy in two dimensions.

Further reduction in the dimensionality is also possible by confining in all three dimensions, i.e. all three dimensions of the device be about or less than the deBroglie wavelength. Such nanostructure sized system is known as quantum dot (QD). In QD electron loses its semi classical character in all

three directions and therefore exhibits quantum-zero dimensional (Q0D) behavior with eigen values given by,

$$E_{nk} = E_c + l^2 E_{ox} + m^2 E_{oy} + n^2 E_{oz} \qquad l,m,n = 1,2,3.. \qquad ...(2.9)$$

where E_{ox} is quantized energy for effective length of quantum well in $x-$direction.

Further enhancing the speed of nanotransistors, Sakaki has proposed novel QWW and quantum box arrays [Sakaki, 1980; Arora and Sakaki, 1991]. The eigen values in the coupled QWW array can be written as,

$$E_{nk} = E_c + \frac{E_b}{2}\left(1-\cos\left(k_x d\right)\right) + m^2 E_{oy} + n^2 E_{oz} \qquad ...(2.10)$$

where E_b is the width of the miniband in a superlattice of period d.

2.5 (a) ii. Density of States (DOS) of SQSS

The concept of density of states (DOS) is extremely powerful and important as various physical properties of low dimensions, such as optical absorption, emission, electrons transports etc are influenced by it. DOS is defined as the number of available electronic states per unit volume per unit energy around energy. The DOS is highly influenced by the confinement of the dimensions of devices. The DOS per unit volume per unit energy $N(E)$can be easily evaluated from its definition as,

$$N(E) = \frac{1}{L_x L_y L_z}\sum_{\alpha s}\delta\left(E - E_\alpha\right) \qquad ...(2.11)$$

Where α stands for quantum numbers, $\alpha = \left(k_x, k_y, k_z\right)$, $\left(n, k_x, k_y\right)$, $\left(n, m, k_x\right)$ and $\left(n, m, l\right)$ for $3D$, $Q2D$, $Q1D$ and QD systems respectively. s stands for the two spin states of the electron. Summation over k's can be converted to integration by using k space density of states factor $\left(L_i/2\pi\right)$, where $i = x, y, z$. However, on discrete quantum numbers summation itself is performed. This gives the density of states for various 3D, Q2D, Q1D and QD systems as,

$$\alpha = (k_x, k_y, k_z), \quad N_{3D}(E) = \frac{\left[m^{*3/2}\right]^{1/2} E^{1/2}}{\pi^2 \hbar^3} \qquad \ldots(2.12)$$

$$\alpha = (n, k_y, k_z), \quad N_{2D}(E) = \frac{m^* E^0}{\pi \hbar^2} \qquad \ldots(2.13)$$

$$\alpha = (n, m, k_z), \quad N_{1D}(E) = \frac{\left[m^{*1/2}\right]^{1/2} E^{-1/2}}{\pi \hbar} \qquad \ldots(2.14)$$

$$\alpha = (n, m, l) N_{0D}(E) = \delta(E - E_0) \qquad \ldots(2.15)$$

Fig. 2.3 gives variations of DOS with energy for 3D, Q2D, Q1D and QD systems i.e. comparison of the density of states as a function of energy. We noticed that as the dimensionality of the system changes, the energy dependence of the DOS also changes. In three dimensional systems DOS is dependent on $E^{1/2}$, given by equation (2.12). In two dimensional system DOS has a step function due to E^0 dependences, and is given by equation (2.13). In one dimensional system DOS have $E^{-1/2}$ dependence, as in equation (2.14). While in zero-dimensional system the DOS has a peak (i.e. delta function) as is given by the equation (2.15).

DOS for the triangular quantum well in the case of 2D EG is,

$$N_i = \int D(E) f(E) dE$$

$$N_i = \frac{m^* k_B T}{2\pi \hbar^2} \ln\left[1 + \exp\left(\frac{E_F - E_i}{k_B T}\right)\right] \qquad \ldots(2.16)$$

DOS for triangular quantum well in case of 1D EG is,

$$N_i = \frac{m^*}{\sqrt{2 k_B T}\, \pi \hbar} \int \frac{\left(E / k_B T\right)^{-1/2}}{\left(1 + e\left(\frac{E_i - E_F}{k_B T}\right)\right)} \partial\left(\frac{E}{k_B T}\right) \qquad \ldots(2.17)$$

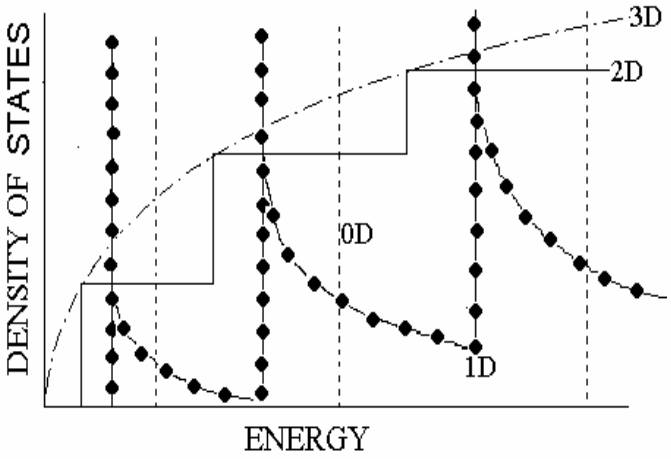

Fig. 2.3 The parabolic curve, step curves, oscillating and delta function curves indicate the variations of DOS versus energy for 3D, Q2D, Q1D and QD system respectively.

DOS for quantum well array is given by,

$$N_{SL} = \frac{2}{\pi E_d d L_y L_z} \frac{1}{\left[1 - z\left[1 - \frac{1}{E_b}\left(E - E_{nm}\right)\right]\right]^{1/2}} \qquad \ldots(2.18)$$

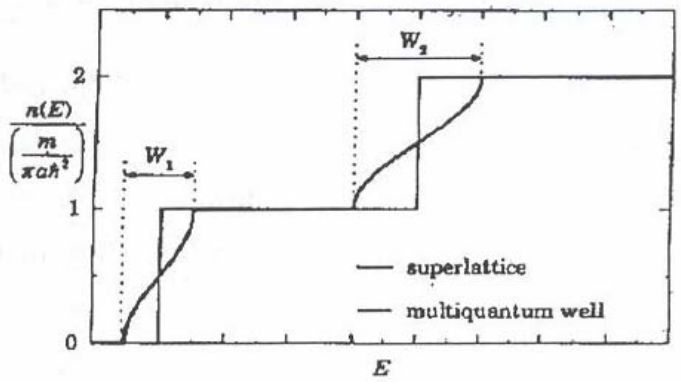

Fig. 2.4 DOS for a superlattice (thick line) and a multiquantum well (thin line).

DOS versus energy for a SL and MQW are shown in Fig. 2.4. As quantization takes place the conduction band lifts higher, whereas, the holes push down the valence band edge. This effectively increases the band gap and causes decrease the number of intrinsic carriers (Quantum Freeze Out Effect). The

decrease in intrinsic carrier concentration may affect the noise properties of nanostructure devices.

Considering all the low dimensional device (LDD) system various electronic properties are determined. Some of their reviews are given below.

The general expressions for S, σ and κ_e for bulk (3D), QW (2D), and QWW (1D) were derived using the relaxation-time approximation by various authors [Hicks and Dresselhaus, 1993; Hicks and Dresselhaus, 1993].

Balandin [Balandin, 2000] reviewed the thermal and thermoelectric properties of semiconductor low-dimensional structures i. e. QWs and QWWs.

In the case of LDD, the reduction of the dimensionality leads the electronic DOS to accumulate near the subband transitions. Appropriate doping step and even delta doping change the available states for electrons results in a strong asymmetry in the differential conductivity [Shakouri and LaBounty, 1999; Broido and Reinecke, 2000]. The consequence of this strong asymmetry is an enhanced thermopower which corresponds to the numerator of the ZT factor.

When designing lower dimensional structures, superlattices are typically used since they provide the additional benefit of reducing the thermal conductivity [Hyldgaard and Mahan 1997; Chen, 1998; Venkatasubramanian, 2000] i.e. the denominator of the ZT factor. With careful designing of the materials, thickness and period of superlattices, phonon blocking electron-transmitting sourced can be realized [Venkatasubramanian, 1999].

The advantages of heterostructure thermionic cooling can be combined with that of lower dimensional structures by using multi quantum-well structures. The added constraint on the number of available electronic states should provide additional electron filtering and further improve the thermopower [LaBounty, 2001].

The advantage of thin film cooler is the dramatic gain in cooling power density as it is inversely proportional to the length of the thermoelements. Thin films of the order of microns should provide cooling power densities greater than 1000 W/cm^2. This capability for large cooling capacities is paramount for cooling of optoelectronic devices.

The second convenience of using thin films is that they allow for the possibility of monolithic integration. Besides the lower cost and higher reliability, monolithic integration enables precise control over temperature anywhere on the surface of the substrate where the devices to be cooled and located. The small thermal mass of the cooler also permits a very fast cooling response.

Along with these advantages, several disadvantages also become apparent and must be considered when we move from bulk to thin film coolers. The reduction in the thermal resistance between the cold and hot sides of the cooler is one of them. The trade-off for increased cooling power is a reduced temperature differential and efficiency. Other non-ideal effects such as, contact resistance, thermal resistance of the heat sink and heat generation in the current carrying connections are secondary effects in the bulk Thermoelectric coolers, but they all must be considered for thin film coolers [LaBounty, Shakouri and Bosers, 2001].

Recently, there have been inceasing number of studies on the modification of thermal conductivity [Walkauska et al., 1999] and the enhancement of the thermoelectric figure of merit of QW [Hilcks and Dresselhaus, 1993; Broido and Reinecke, 1995]. A large value of ZT, up to 14 at room temperature was predicted for Bi_2Te_3 quantum wire with side $a = 5\,\mathring{A}$ [Hilcks and Dresselhaus, 1993]. The figure of merit of quantum wire superlattice $a = 20\,\mathring{A}$ was also found to increase about 2.5 times from its bulk value of $ZT_{3D} = 0.53$ [Broido and Reinecke, 1995]

2.5 (b) Magnetically Quantization Semiconductor Systems (MQSS)

The quantization of energy levels described above due to spatial confinement of semiconductors can be achieved by external perturbation like electric field, magnetic field also. Here, we see the quantization due to magnetic field.

When a semiconductor is subjected to a magnetic field, electrons get deviated from its original path due to the Lorentz force. The direction of the Lorentz force is always perpendicular to the direction of travel of the particle as well as to the direction of the magnetic field. In such situation, provided the magnitude of the magnetic field is high, the motion of the electrons will be circular on the surface perpendicular to the direction of the magnetic field. The angular velocity gained by the electron due to the high magnetic field is

given as $\omega = Be/m^*$. The particles do not gain or lose any energy due to the angular acceleration of the magnetic field since the acceleration is uniform.

In the quantum mechanics, the circular orbits associated with the Lorentz force must be quantized in various orbits. The quantization occurs about a constant potential like that of electrons in various orbits with the nucleus at the centre of an atom. The particles execute time-harmonic motion similar to the motion in a harmonic oscillator potential. The energy associated with the motion in the plane perpendicular to the magnetic field is expected to be quantized and forms various Landau energy levels.

In Hamiltonian mechanics, the equations of motion are formulated in terms of potentials rather than in terms of the electric and magnetic fields. The potential associated with a magnetic field is a vector potential.

2.5 (b) i. Energy Band Quantization of MQSS

If we consider a large magnetic field is applied along z-axis, the motion along the xy plane gets quantized and various levels of energy levels are formed called Landau levels [Landau, 1930]. The equation (2.8) gets modified due to the magnetic quantization. Hence, the $\vec{E} \cdot \vec{k}$ relation will be,

$$E\left(\vec{k}\right) = \frac{\hbar^2 k_z^2}{2m^*} + \hbar\omega_c\left[\left(n + \frac{1}{2}\right)\right] \qquad \ldots(2.19)$$

The equation (2.19) shows that in the presence of a large magnetic field, the kinetic energy due to motion along the direction of the magnetic field i.e. along the z-axis is still free for motion and hence be $\hbar^2 k_z^2 / 2m^*$.

Whereas, on the xy-plane, the conduction and the valence bands of a semiconductor split into equally spaced energy levels are called Landau levels. It is given by second part of the equation (2.19). The separation between each Landau level is given by $\hbar\omega_c$. Hence, the scenario be quasi one dimensional (Q1D) and is exactly, as that, in the case of quantization due to spatial confinement of 1D EG.

The corresponding energy eigen values are independent of the center coordinate (and thus the transverse momentum, k_y) and are given by the well-known expression for a harmonic oscillator,

$$E_n = \hbar\omega_c\left[\left(n+\frac{1}{2}\right)\right], \qquad n = 0,1,2,3,4 \qquad \text{...(2.20)}$$

Where n the energy levels of the quantized Landau states, is an integer including zero. $\hbar$ and ω are the Plank's constant divided by 2π and cyclotron frequency. The corresponding cyclotron radius (r_n) to the classical orbit associated with the energy equation is,

$$r_n = \left[2\hbar\left(n+\frac{1}{2}\right)\Big/ eB\right]^{1/2} \qquad \text{....(2.21)}$$

Where B is the magnitude of magnetic flux. For $n = 0$, we have $r_0 = l_m$, the magnetic radial length at ground state of the Landau level. The integer n corresponds to different Landau levels associated with different magnetic subbands, is given in Fig. 2.5

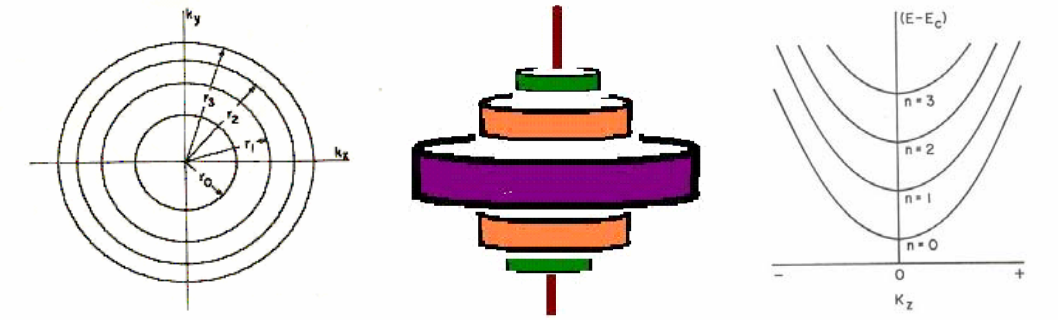

(a) (b) (c)

Fig. 2.5 (a) A cross-section view of quantized Landau levels along the xy-plane with different radii of curvatures (b) The longitudinal view of co-centric circles along z-direction (c) Variation of energy versus wave vector along z direction. The various quantized Landau energy levels are represented by n=0, 1, 2, 3…

Fig 2.5 (a) shows the quantized Landau levels on xy- plane with various radii shown by r_1, r_2, r_3…..in the figure, (b) shows the concentric cylinders of the correspond radii along the z-axis, where the direction of the magnetic field is along z axis, Fig 2.5 (c) shows the energy versus wave vector along z-axis.

When the applied magnetic field is very strong, the condition be $\hbar\omega_c \rangle\rangle k_B T. E_F$, the Fermi energy of electrons occupy the lowest Landau level i.e. the energy level corresponding to Landau quantum number $n = 0$. The condition is called the extreme quantum limit (EQL).

The transverse and longitudinal conductivities of the electrons in the EQL in the case of Fermi statistics was being studied by various authors [Argyres and Adams, 1956; Abrikosov and Ryzhkin, 1978; Muzrin and Golovkov, 1991]

Argyres et al. [Argyres and Adams, 1956] studied theoretically the longitudinal conductivity in EQL and suggested that the resistively in the EQL is lower than the resistively in the absence of a magnetic field.

The thermoelectric power (TEP) in the presence of a longitudinal quantizing magnetic field has been studied by some other authors also [Anslem and Askerov, 1982; Askerov, Babaev and Dzhafarov, 1989].

First time the reverse sign of magnetic TEP in n-$Hg_{0.8}Cd_{0.2}Te$ in longitudinal direction in the presence of magnetic fields 5T~at temperature gradient of 10K-30K is observed by Lashkarev et al. [Lashkarev et al., 1991].

The longitudinal magneto-Seebeck coefficient (magneto thermo power) in polar semiconductor in EQL has been calculated by Sarkar and Chattopadhyah [Sarkar and Chattopadhyah, 1979]. The authors have also shown that the Seebeck coefficient increases with magnetic field. They used an iterative solution of the Boltzman equation leaving the concept of relaxation time. The effect of electron spin [Sarkar and Chattopadhyay, 1978] on TEP of polar semiconductors in EQL is also being studied by the same authors.

2.5 (b) ii. Density of States (DOS) of MQSS

The splitting of the energy band causes modification of the density of states i.e. the density of states in the absence of a magnetic field is a parabola and is given by $D(E) = E^{1/2} dE$, now it becomes the sum of a set of one dimensional density of states, each starting at the bottom of each Landau levels.

DOS in presence of a magnetic field [Blakemore, 1980] is given as,

$$N_B = \frac{1}{(2\pi)^2}\left(\frac{2m^*}{\hbar^2}\right)^{3/2}\hbar\omega_c \sum_n \left[E - E_c - \left(n+\frac{1}{2}\right)\hbar\omega_c\right]^{-1/2} \qquad ...(2.22)$$

Fig 2.6 presents the variation of DOS versus quantizing magnetic field. Also mentioned earlier that the quantization of energy levels due to magnetic field gives Q1D system hence, the nature of the curve for 1D system, in Fig. 2.3 is similar to that of Fig. 2.6.

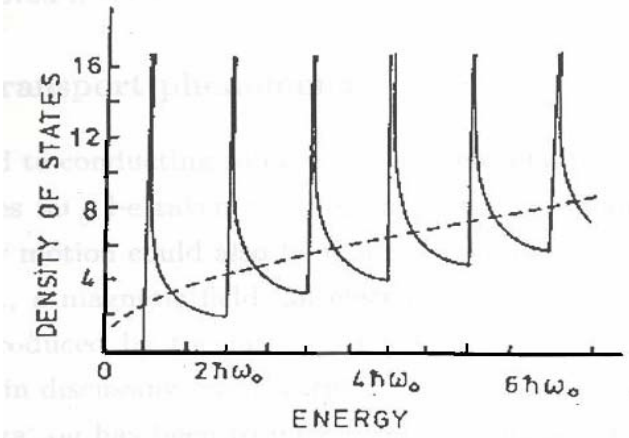

Fig. 2.6 The variation of DOS with energy in a quantizing magnetic field.

With the help of the parabolic potential and Schödinger equation, given by equation (2.3), various transport parameters in magnetically Q1D system is determined.

Santra and Sarkar [Santra and Sarkar, 1993] have theoretically calculated the energy loss rate of hot electron in the narrow band gap semiconductors in EQL assuming electric-field dependent perturbation phonon distribution.

For narrow band gap semiconductor such as MCT, the nonparabolic nature of the Landau subbands will have an influence on the transport parameters in two ways. First, there will be a modification of the effective mass. Second, a factor known as over lap function appears in the expression for the scattering rate. This is because in a nonparabolic semiconductor the cell periodic part of the Bloch functions is no longer spherically symmetric but is a mixture of p-type valence band wave function. In the calculations given by different

workers, the nonparabolicity of the subbands in the EQL is incorporated by considering only the change in effective mass. In other words, the overlap function is taken to be unity.

Baumik and Sarkar [Baumik and Sarkar, 1994] observed the transient response of hot electrons in narrow-gap semiconductors at low temperatures in the presence of a longitudinal quantizing magnetic field.

Electrical conductivity of hot electrons in narrow-gap semiconductors [Bahumik and Sarkar, 1993] and small signal AC response of hot electrons in $n-Hg_{0.8}Cd_{0.2}Te$ [Bahumik and Sarkar, 1992] in the EQL at low temperatures have also been studied.

2.6 Scattering Mechanisms

Boltzmann transport equation provides a semiclassical description of a quantum mechanical system. Though it has certain limitations, most of the results on electron transport in semiconductors are derived from this equation [Nag, 1980].

Transition probability

The knowledge of probability of transitions of electrons from the state k to the state k' per unit time to obtain the expression for $(\delta f/\delta t)_{coll}$ for a particular scattering process are very essential while dealing various transport characteristics of electronic devices. The probability, denoted by $P(k,k')$ is calculated by the time dependent perturbation theory [Schiff, 1968].

When electron is scattered from k to k' by absorbing or emitting a phonon of energy $\hbar\omega_Q$, we can write [Ehrenreich, 1957],

$$P(k,k') = \frac{2\pi}{\hbar}\left|M\left(k,k^1\right)\right|^2\left\{\delta\left[E(k') - E(k) \pm \hbar\omega_Q\right]\right\} \qquad \ldots(2.23)$$

In the equation (2.23), the positive sign is taken for absorption and the negative sign is taken for emission. Where $\left|M\left(k,k^1\right)\right|$ is the matrix element of

the scattering potential. $\delta(x)$ is the Dirac delta function, implying energy conservation.

In a crystal with perfect periodicity, an electron is expected to move freely and the transport is determined by electron dynamics as that in the case of vacuum tubes. It is the imperfections which scatter the electrons and cause scattering dominated transport. The effective scattering processes are lattice scattering of various kinds, i.e. deformation potential acoustic phonon (ac), piezoelectric phonon (pz) and polar and non-polar optical phonon scatterings. These are nonelastic scattering mechanisms where the exchange of energy takes place. The elastic scattering mechanisms are ionized (in), neutral impurity scattering (nue) and alloy disorder scattering (all) in the case of mixed or alloy compounds.

The **acoustic phonon** (ac) via deformation potential scattering mechanism is caused by the perturbing potential arising from the strain produced in the crystal lattice by the acoustic vibrations.

In crystals lacking inversion symmetry, other than the deformation potential interactions, piezoelectric coupling occurs with acoustic modes. The displacements of the ionized atoms associated with the acoustic vibrations in these crystals produce an electrical polarization giving rise to **piezoelectric scattering** of the carries. Both transverse and longitudinal vibrations contribute, but only the longitudinal electric fields produced by these vibrations are significant [Hutson, 1961].

Piezoelectric scattering (pz) is important for weak-field transport at low temperatures [Zook, 1964]. At high fields however, the important of this type of scattering deceases since the corresponding scattering rate diminishes with increasing electron energy.

The dipole moments formed by the interaction of the ionic charges on the atoms with the optical mode lattice vibrations due to excess temperature gives rise **polar optical phonon** (pop) scattering mechanism. In compound semiconductors, two types of optical phonons are present, polar optical phonon and non polar or intervalley optical phonons.

The calculation of the relaxation times and mobility of electrons in the semiconductor layers in the presence of phonon scattering has been performed earlier by several workers [Riddley, 1982; Price, 1981]. The

relaxation time in the quantum well structure has also been calculated by Chaubey et al [Chaubey and Singh, 1984]

The uniform periodic potential distribution of an ideal crystal lattice is distributed by the presence of impurities on atoms which are usually ionized at ordinary temperatures. These periodic impurity potentials give rise to scattering centers for the electron gas. This type of scattering is called **impurity scattering**. The impurity potential is Columbic in nature. When the impurities are embedded in the semiconductor narrow channel through which the electors move, it is know as **back ground** impurity.

When the electrons are scattered by the Columbic field of the far-off impurities embedded in the cladding, it is called remote impurity scattering. For a sufficiently thick spacer the effect of the far remote impurities would be rather small [Tsubaki, Sugimura and Kumabe, 1985].

In compound semiconductors, the scattering of the electrons by ionized impurities limits the mobility of the sample [Stern and Howard, 1987]. Since very little energy is exchanged in the process of scattering to electrons by the massive ionized centers, the scattering is essentially elastic and can be described by a relaxation time. The different modes of ionized impurity scattering have been given by Chattopadhyah and Queisser [Chattopadhyah and Queisser, 1981]. The effects of the background impurities as well as the remote impurities are important for LDD. The size effects and the degeneracy or carrier distribution functions are also incorporated.

It is known from the study of two-dimensional electron gas (2D EG) that the interface between Si and SiO_2 in a FET or between GaAs and AlGaAs in a HEMT is not perfectly smooth. The deviation from non-planarity gives rise to additional scattering mechanism known as **surface roughness** scattering mechanism, which plays an important role in limiting the mobility at low temperatures and high carrier densities. It is also found to be effective in increasing the cyclotron resonance and photoluminescence line width in heterojunctions.

Several authors [Ando and Uemura, 1974; Ridley, 1982; Prasad and Fajita, 1978] have calculated the transport and optical properties of the electrons in the inversion layers of MOSFET's and superlattices at low temperatures by assuming the scattering of the electrons by the surface roughness or the impurity ions.

In alloy semiconductors, the dissimilar of the compounds leads to distortions in the band structure at the points in the crystal where the two kinds of compounds meet. These discontinuities act as scattering centers and give rise to the so called **alloy scattering** [Makowski and Glicksman, 1973; Glicksman et al., 1974]. This alloy occurs in addition to the usual scattering processes along with other non alloy scattering mechanisms. Marsh [Marsh, 1982] proposed a new theory of alloy scattering which assumed the presence of compositional clusters in alloy semiconductors. This was used in electron transport calculation for $Ga_{0.47}In_{0.53}As$ and a good agreement was obtained with experimental velocity field date, measured upto the threshold electric field.

Sarkar and Banerji [Sarkar and Banerji, 1989] estimated the alloy scattering potential in $\mathrm{Ga_{0.47}In_{0.53}As}$ using cyclotron resonance measurement. The authors [Sarkar and Banerji, 1992] also observed the effect of alloy scattering on the cyclotron resonance linewidth in $\mathrm{Ga_{0.47}In_{0.53}As}$ at low temperatures.

The authors [Banerji and Sarkar, 1991] also estimated the alloy scattering strength in MCT from the magnetic field dependence of the longitudinal resistivity in $n-Hg_{0.8}Cd_{0.2}Te$. In the same material the authors have observed the effect of alloy scattering [Banerji and Sarkar, 1994] in the EQL at low temperatures.

When an electron passes close to a neutral atom, there may be transferred in the momentum of the electron with a bound electron on the atom. Such transfer of momentum gives rise the momentum scattering due to **neutral impurity** scattering.

When a number of scattering mechanisms are present in a system then the total of them is obtained by using Mathiessen's [Matthiessen, 1964] rule.

The characteristics of the quantum transport differ from the classical transport due to the modification of the energy band structures, DOS and the scattering probability [Roth and Argyres, 1966]. Important transport parameters are determined by using Boltzman transport equation with the above appropriate scattering mechanisms under various types of quantized conditions. Under such quantized considerations the scattering rates as well as the transport coefficients are highly altered due to the change in the

density of states. However, the general characteristics of the band–structure remain unaltered.

The electron mobility imposed by lattice vibrations in the inversion layers of MOS structures was studied by different workers [Ando et al., 1982; Lee et al. 1991].

Sakaki [Sakaki, 1980] has studied theoretically, the transport properties of electrons in ultrafine wire structures. He calculated the scattering probability of such size quantized electrons for Coulomb potential and the scattering probability is found to be suppressed drastically because of the one dimensional (1D) motion in the wire.

2.7 Photoelectric Emission under Spatial and Magnetic Quantization: Optical Properties

Optoelectronics is related to study of generation, control and reflection of light by electronic materials. The research on optoelectronic is very important due to its higher application in present electronic devices, without which we can not imagine our daily life. The original idea of investigation on QWs was given by Esaki and Tsu [Esaki and Tsu, 1970]. They were interested for electronic transport phenomena in multiple QWs. The multiple periodic structures of QWs are called superlattice (Sl). Latter on MQW, superlattice is also found to be useful in optoelectronic devices. It is found that the use of superlattice to produce laser is far efficient. Sl improves the performance of devices such as laser diodes, light-emitting diode (LEDS), solar cells, optical logic gates and intersubband infrared detectors. The quantized LDD are important from the view point of optoelectronic devices, because:

1. The quantization of energy levels due to the confinement restricts the motion of the carriers to flow and it shifts the band edge to higher energy value.
2. The confinement keeps the electrons and holes closer together than in the case of 3D devices.
3. DOS becomes independent of energy, whereas for 3D materials DOS is proportional to $E^{1/2}$

2.7 (a) Optical Properties

Many theoretical and experimental studies on the linear and nonlinear optical properties of II-VI microcrystalline in quantum region have been already carried out by various authors [Ekimov et al. 1982; Brus et al. 1984; Ekimov, 1985; Sandroff 1986; Masumoto, 1988]. The studies of the III-V semiconductors as Q1D, QD is still untouched because of difficulties to fabricate uniform arrays of quantum-size structures [Sandroff et al., 1989].

In Q1D and QD, due to the confinement the nature of DOS changes. The increased differential gain and the gradually increased in the modulation bandwidth of the laser due to such change in DOS has been observed in QW lasers in the presence of magnetic field by many authors [Arakawa et al. 1982; Yairv A., 1988].

When the thermal broadening of the carrier energy distribution is reduced, the narrower line width is observed. The minimum threshold currents required for optically confinement as well as by carrier confinement is found to be almost two orders of magnitude lower for QWW lasers of GaAs to that of QW GaAs [Yariv, 1988]. Sakaki [Sakaki, 1989] observed that uniformity of the structure is essential to obtain the above advantage in lasers made from wires and dots. He also predicted that the inhomogeneous broadening of energy levels due to size fluctuation is much smaller than the thermal broadening and the energy level pacing be much larger than the average KE of the particles.

The confinement modifies DOS as well as Coulomb interaction. The effects of confinement on the Coulumb energy of the exciton fall into three size regimes [Efros and Efros, 1982]. In the regime of smallest sizes, strong confinement occurs where both electron and the hole zero-point energies are much larger than the exciton binding energy. The zero-point motion of the exciton is determined by its reduced mass. Schmitt Rink et al. [Schmitt-Rink, 1987] discussed QD in this limit for which the lack of a quasi contribution of single particle states has major consequences. Screening, exchange and band-gap renormalization are absent and the only serving sources of nonlinear absorption near the band is state filling [Schmitt, 1987]. In quantum wires, the correlation of the electrons and hole in the confined direction is enhanced by the increased overlap of the wave functions in the confined direction [Bryant, 1988].

For both wires and dots, binding energies and oscillator strengthens for free excitons and impurities located at the centers of the structures are enhanced,

but for infinite barriers diverge as the structure size is reduced [Suemune and Coldren, 1988; Baryant, 1984; Baryant, 1985; Kodama, Osaka and Yamanishi, 1985; Kayanuma, 1986; Houdre et al., 1986].

Optical properties mainly deal with emission and absorption properties of a system. Optical emission is mainly photoelectric emission caused by the external photo energy on the electrons, whereas optical absorption creates an electron and hole pair. The interaction between these oppositely charged particles can not be neglected. The mutual interaction between them causes bound state and is called exciton. The excitons modify the strength of optical absorption strongly near the band gap and they become more important as the number of dimensions of the system be reduced. Quantum confinement of the carriers leads to the formation of quantized energy levels which modifies the optical properties particularly of the photo absorption and photo emission [Chiang, Ludeke, Eastman, 1982; Bacher et al., 1988; Miller et al., 1984].

2.7 (b) Photoemission Process

The optical spectroscopy is a very powerful tool in studying the electric structures of solids. The potential of the phenomena of photoelectric emission for investigating electronic levels are recognized by Roninson and deBroglie, after the discovery of the phenomena by Hertz [Hertz, 1887] and its interpretation by Einstein [Einstein, 1905]. The phenomena is described as follow,

When a sample is placed into a vacuum chamber and irradiated with monochromatic photons of sufficient energy to excite electrons into unbound states, the electrons emitted into the vacuum will have the information about the sites they left behind. The information is very important to know the initial status of the electrons.

When photons of a certain energy $(h\nu)$ are incident on a sample, having electrons in quantized energy levels E_i, E_i should be below the Fermi energy (E_F) according to Fermi Dirac Statistics the electrons, in the quantized energy levels absorb the energy in the form of photon and ejects electrons with a certain KE (E_k). After absorbing the photon of energy $h\nu$, the quantized electrons overcome the work function (ϕ) to escape from the solid with the KE (E_k).

Hence, the expression is,

$$h\nu = (E_F - E_i) + \phi + E_k$$

$$\text{or } E_b = (E_F - E_i) = h\nu - \phi - E_k \quad \ldots (2.24)$$

Where E_b is the electron binding energy.

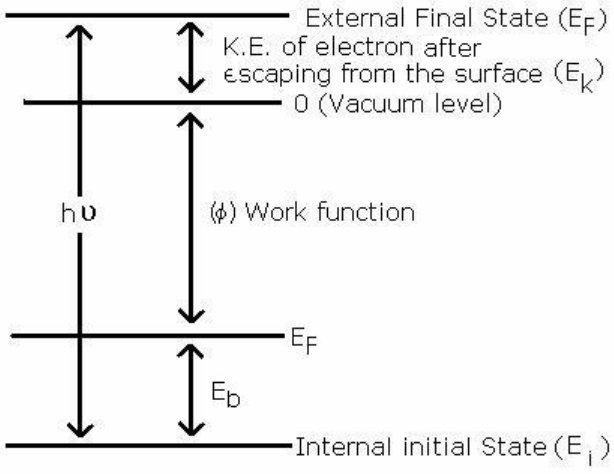

Fig 2.7 Electronic transitions in photoelectron spectroscopy.

The three step mode of Spicer [Spicer, 1958] is used to explain the process of PE as shown in Fig 2.7. The phenomena have been studied in 3D electron gas in metals and semiconductors [Cardon and Ley, 1978]. The influence of disorder due to scattering on the DOS, due to the presence of level broadening at low temperature for 2DEG was investigated [Kramer and Mackinnon, 1993; Lifshitz, 1965; Altshuler and Aaron, 1985; Fertin and Sharma, 1989; Leo and Mac, 1990; Berkovits and Feng, 1992].

Berkovits [Berkovits, 1995] has calculated the explicit form for the broadening of the DOS peaks as a function of disorder taking a perturbation diagrammatic method.

Similarly to Q2DEG structure, the Q1D wire has also the broadening of the unperturbed energy levels due to impurities. Research on electron-optical effects in such QD system is attracting attention due to their wide applicability in the field of optoelectronic [Schmitt-Rink et al., 1987; Arakawa and Sakaki, 1982; Weisbuck and Nagle, 1990; Baryant, 1990].

2.7 (c) Effect of Broadening on Spatially and Magnetically Quantized Semiconductor Systems

Till now, we have observed the ideal cases of quantization, but in real material, impurities or other nonidealities are present in the systems. Hence, the delta-function density of states of the ideal system is broadened as shown in Fig. 2.6. Using the so-called self consistent Born approximation in perturbation theory. Ando et al. [Ando, Fowler, Stern, 1982] has shown that the DOS in the presence of short range potential impurities has the form,

$$D(E) = \frac{1}{2\pi l_m^2} \sum_n \left[1 - \left(\frac{E - E_n}{\Gamma_n} \right)^2 \right]^{1/2} \ldots \qquad \ldots(2.25)$$

Where Γ_n is a broadening factor associated with the sort-range impurities.

The quantization of energy band structure causes the DOS function to possess a very sharp singular structure which should subsequently be reflected through the step like nature in various optical and electronic transport parameters. Due to the presence of impurities and imperfections in real system the measurement techniques for the above parameters do not exactly match with the predicted nature. These imperfects and impurities significantly influence the motion of electrons giving rise to broadened energy levels, otherwise sharp and consequently modify the DOS. To assess the effect of disorder due to electron-impurities interactions on the ideal system, the modified DOS must be taken into account while investigating optical processes from QLD systems [Roth and Argyres, 1966].

Chakraborty et al. has [Chakraborty , Bose and Sarkar, 1997] observed the effect of level broadening on the photo-electric emission from a single quantum well in ultrathin film under the influence of a quantizing magnetic field. The same author has also studied induced shifts of electronic energy levels in spherical quantum dot by electric field [Chakraborty, Bose and Sarkar, 1997].

Authors [Mutusuddi, Bose and Sarkar, 2004] also showed that the energy level broadening on the photoemission current density is oscillatory in the nature in the case of geometrically confined Q1D system.

References

Abrikosov A. A. and Ryzhkin I. A., Adv. Phys. 27, 254 (1978).
Altshuler B.L. and Aaron A.G., in Electron- Electron Interactions in Disorder System, ed. Al Efros and M. Pollak {Elsevier, Amstrang} (1985).
Ando T., Fowler A.B. and Stern F., Rev. Mod. Phys. 54, 437 (1982).
Ando T. and Uemura Y., J. Phys. Soc. Jpn. 36, 959 (1974).
Ando T., Fowler A.B. and Stern F., Rev. Mod. Phys. 54, 437 (1982).
Anslem A.I. and Askerov B.M., Sov. Phys. Solid. State 4, 1154 (1982).
Arakawa Y. and Sakaki H., Appl. Phys. Lett. 40, 939 (1982).
Argyres P.N. and Adams E.N., Phys. Rev. 104, 900 (1956).
Arora V.K. and Sakaki H., Proceeding of the Inter. Workshop on Semiconductor Devices, Dec.2-6, 1991, Tata Mc. Graw Hill, New Delhi 38, (1991).
Askerov B.M., Babaev M.M. and Dzhofarov M.I., Phys. Stat. Sol. (b) 151, K157 (1989).
Bacher F.R., Blakemore J.S., Ebner J.T. and Arthur J.R., Phys. Rev. B 37, 2551 (1988).
Bahumik S. and Sarkar C.K., Czechoslovak Journal of Physics 44, (9), 871 (1994).
Bahumik S. and Sarkar C.K., Semicond. Sci. Technol. 7, 311-314 (1992).
Balandin A., Phys. Low-Dim. Struct., ½ (2000) pp1-28 (2000).
Banerji P. and Sarkar C.K., J. Appl. Phys. 70, 1467 (1991).
Banerji P. and Sarkar C.K., J. Appl. Phys. 72, 1231 (1994).
Banerji P. and Sarkar C.K., Solid State Communications 90, 5, 325, (1994).
Barker B.I., Rayborn G.H., Ioup J.W. and Ioup G.E., Ann. J. Phys. 59, 1038 (1991).
Baryant G.W., Phys. Rev. B 29, 6632 (1984).
Baryant G.W., Phys. Rev. B 31, 7812 (1985).
Baryant G.W., Phys. Rev. B 37, 8763 (1988).
Baryant G.W., Science and Engineering of One and Zero-Dimensional Semiconductors, Beanmont S. P. and Sotomajor C. M., Eds. NY, Plenum, 243-524 (1990).
Benedict T.S., Phys. Rev. 91, 1565 (1953).
Berkovits R. and Feng S., Phys. Rev. B 45, 97 (1992).
Berkovits R., Phys. Rev. B 51, 4653 (1995).
Blakemore J.S., Semiconductor Statistics, Dover Publications, INC, New York (1986).
Brandt M.S., Herbst P., Angerer H., Ambacher O. and Stutzmann M., Phys. Rev. B 58, 7786 (1998).

Broido D.A. and Reinecke T.L., Appl. Phys. Lett. 67, 100 (1995).
Broido D. A. and Reinecke T.L., Appl. Phys. Lett. 77, 705 (2000).
Brus L. E., J. Chem. Phys. 80, 4403 (1984).
Cardona M. and Ley L., Photoemission in Solids I & II Topics in Appl. Phys. 26, 27, Springer, New York (1978).
Chen A.B. and Sher A, J. Vac. Sci. Technol. 21, 138 (1982).
Chen G., Phys. Rev. B 57, 14958, (1998).
Chakraborty C., Bose C. and Sarkar C.K., Solid State Electronics 41, 1386 (1997)
Chakraborty C., Bose C. and Sarkar C.K., Nanostructured Materials 8, 83, (1997)
Chasmar R. and Stratton R.J., Electron Control 7, 52 (1959).
Chattopadhyah D. and Queisser H. L., Rev. Mod. Phys. 53, 745 (1981).
Chaubey M.P. and Singh M., Phys. Rev. B 29, 4803 (1984).
Chiang T.C., Ludeke R. and Eastman D.E., Phys. Rev. B 25, 6518 (1982).
Choi H.W., Zhang J. and Chua S.J., Material Science in Semiconductor Processing 4, 567 (2001).
Cibert J., Petroff P.M., Dolan G.J., Pearton S.J., Gossard A.C. and English J.H., Appl. Phys. Lett. 49, 1275 (1986).
Dexter R N., Zeiger H. J. and Lax B. , Phys. Rev. 95, 557 (1954).
Dohler G.H., Status Solidi B 52, 79 (1972a).
Dohler G.H., Status Solidi B 52, 533 (1972b).
Dorda G., Electron Fisc. Apli. 17, 55 (1957).
Dresselhaus G., Kip A.F. and Kittle C., Phys. Rev. 92, 827 (1953).
Dutta A.N. and Nag B.R. IEEE Tans. MTT 18, 162 (1970).
Efros Al.L. and Efros A.L., Sov. Phys. Semicond. 16, 772 (1982).
Ehrenreich H., J. Phys. Chem. Solids 2, 131, (1957).
Einstein A., Ann. Physic 17, 132 (1905).
Ekimov A.I., Efros Al.L. and Onuschenko A.A., Solid State Comm. 56, 921 (1985).
Ekimov A.I. and Onuschenko A.A., Sov. Phys. Semicond. 16, 775 (1982).
Esaki L. and Tsu R., IBM Res. Report No. Re 2418 (1969).
Esaki L. and Tsu R., IBM, J. Res. Develop. 14, 61 (1970).
Fertin H. A. and Sharma S. Das, Phys. Rev. B 40, 7410 (1989).
Fowler A.B., Fang F.F., Howard W.E. and Stiles P.J., Phys Rev. Lett. 16, 901 (1966).
Fujui T. and Saito H., Appl. Phys. Lett. 50, 824 (1987).
Ghose M., Chakraborty C., Benerji P. and Sarkar C.K., Indian J. Phys. 74 A (4), 399-401 (2000).

Glicksman M,, Enstrom R. E., Mittleman S. A. and Appert J. R., Phys. Rev. B 9, 1621 (1974).
Gotz W., Romano L.T., Walker J., Johnson N.M. and Molnar R.J., Appl. Phys. Lett. 72, 1214 (1998).
Gunn J.B., Solid State Commu. 1, 88 (1963).
Hambleton G.E. and Gartmer W.W., J. Phys. Chem. Sol. 8, 329 (1959).
Harrison J. W. and Hauser J. R., J. Appl. Phys. 17, 292 (1976).
Hertz H., Ann. Physik 31, 983 (1887).
Hicks L.D. and Dresselhaus M.S., Phy. Rev. B 47, 16631 (1993).
Hicks L.D. and Dresselhaus M.S., Phy. Rev. B 47, 12727 (1993).
Houdre R., Hermann C., Lampel G. and Frijlink P.M., Surface Science 168, 538 (1986).
Huang Y., Temperature Dependent Hall Effect Studies of GaN on Sapphire, M. Phil. Thesis, The University of Hong Kong, (2002).
Huang D., Yun F., Reshchikov M.A., Wang D., Morkoc H., Rode D. L. Farina L.A., Kurdak C., Tsen K. T., Park S. S. and Lee K.Y., Solid-State Electronics 45, 711-715 (2001).
Hutson A.R., J. Appl. Phys. 32, 2287, (1961).
Hyldgaard P. and Mahan G.D., Phys. Rev. B 56, 10754 (1997).
Kayanuma Y., Solid State Commun. 59, 405 (1986).
Kodama T., Osaka Y. and Yamanishi M., Jap. J. Appl. Phys. 24, 1370 (1985).
Kotchetkov Dmitri, Zou Jie and Balandin A. Alexander, Mat. Res. Soc. Symp. Proc. Vol. 731, W5.11.1 (2002).
Kotchtkov D., Zou J. and Balandin A.A., J. Appl. Phys. Lett. 79, 4316, (2001).
Kramer B. and Mackinnon A., Rep. Prog. Phys. 56, 1469 (1993)
Kranzer D., Phys. Stat. Sol. (b) 46, 591 (1971).
Kundu S., Sarkar C.K. and Basu P.K., Phys. Rev. B 38, 5730 (1988).
Kundu S., Sarkar C.K. and Basu P.K., J. Appl. Phys. 68, 1070 (1990).
LaBounty C., Ph. D. Thesis, University of California, Santa Barbara, (2001).
LaBounty C., Shakouri A. and Bosers J.E., J. Appl. Phys. 89, 4059 (2001).
Landau L. D., S. Physik 64, 629 (1930).
Lashkarev G.V., Radchenko M.V., Parenskaya E.S., Niktin M.S. and Yu. I. Rastegin JETP letters. Vol. 53, 431 (1991).
Lax B. and Wright G.B., Phys. Rev. Lett. 4, 16 (1960).
Lax B., Zeiger H.J., Dexter R.N. and Rosenblum E.S., Phys. Rev. 93, 1418 (1954).
Lee K., Uroi J., Sim S. And Kim C., IEEE Trans. Electron Devices, ED-38, 1905 (1991).
Leo J. and Mac Donald A.H., Phys. Rev. Lett. 64, 817 (1990).

Lifshitz I.M., Ups. Fiz Nauk 83, 617 (1965); Sov. Phys. USp 7, 549 (1965)
Liliental Z.- Weber et al. MRS Symp. Proc., 395, 351, (1996).
Littman H. and Davidson B,, J. Appl. Phys. 32, 217 (1961).
Look D.C. and Molnar R.J., Appl. Phys. Lett. 72, 1214 (1998).
Look D.C. and Molnar R.J., Appl. Phys. Lett. 70, 3377 (1997).
Look D.C., Sizelove J.R., Keller S., Wu Y.F., Mishra U.K. and Denbaars S.P., Solid State Commun. 102, 297 (1997).
Loschner H., J. Appl. Phys. 41, 3585 (1972).
Mahan G.D., J. Appl. Phys. 76, 4362 (1994).
Mahan G.D., J. Appl. Phys. 65, 1578 (1989).
Makowski L. and Glicksman M., J. Phys. Chem. Solids 34, 487 (1973).
Marsh J.H., Appl. Phys. Lett. 41, 732 (1982)
Masumoto Y., Yamazaki M. and Sugawara H., Appl. Phys. Lett. 53, 1577 (1988).
Mathiessen A., Ann. Phys. Chem 7, 761, 892 (1964).
Miller D.A.B., Chemla D.S., Damen T.C., Gossard A.C., Wiegmann W., Wood T.H., and Burrus C. A., Phys. Rev. Lett. 53, 2173 (1984).
Moravec P., Grill R. Franc T. and Varghova R., Hoschl P. and Belas E., Semicon. Scie. Tech. 16, 7-13, (2001).
Mutsuddi I., Bose C. and Sarkar C. K., Phys. Stat. Sol. (b) 241, 1053-1057 (2004)
Muzrin S.S. and Golovkov N., JETP Lett. 54, 166 (1991).
Nag B.R., Electron Transport in Compound Semiconductors Vol. II, edited by H.J. Queisser (springer Berlin) (1980).
Nag B.R. and Dutta G.M., Phys. Stat. Sol. (b) 71, 401 (1975).
Ng H.M., Doppalapudi D., Moustakas T.D., Weimann N.G. and Eastman L.F., Appl. Phys. Lett. 73, 821 (1998).
Pankove J.I., Moustakas T.D., Gallium Nitride GaN I. edited by (Academic, New York, pp.175 (1998).
Pething R. and South R.B., IEEE Trans, IE 23, 460 (1974).
Phadke U. P. and Sharma S., J. Phys. Chem. Sol. 36, 1 (1975).
Pödör B., Phys. Status Solidi 16, K167 (1966).
Ponce F.A., MRS Bulletin 22, 51 (1997).
Prasad M. and Fujita, Phisica (Ulrecht) 91A, 1 (1978).
Price P.J., Phys. Rev. 104, 1223 (1956).
Price P.J., Ann Phys. (NY) 133, 217 (1981).
Ramsa A.P., Jacobs H. and Brand F.A., J. Appl. Phys. 30, 1054 (1959).
Ridley B.K., J. Phys. C, 15, 5899 (1982)
Rittner E. S. and Neumark G. F., J. Appl. Phys. 34, 2071 (1963)

Rode D.L, in Semiconductors and Semimetals ed: R. K. Willardson and A.C. Beer (Academic Press, NY), V 10 (1975).

Roth L.M. and Argyres P.N., Semiconductors and Semimetals, edited by R. K. Willardson and Beer A. C., 1, 159 (1966).

Sakaki H., Jpn. J. Appl. Phys. 19, p.L735 (1980).

Sakaki H., GaAs and Related Compounds (1988).

Sandroff C.J., Hwang D.M. and Chung W.M., Phys. Rev. B 33, 5953 (1986).

Sandroff C.J., Harbison J.P., Ramesh R., Andrejco M.J., Hegde M.S., Hwang P.M., Chang C.C. and Vogel E.M., Science 245, 391 (1989).

Santra K. and Sarkar C.K., Phys. Stat. Sol. (b) 161, 329 (1990).

Santra K. and Sarkar C.K., Phys. Rev B 47, 3598 (1993).

Santra K. and Sarkar C.K., Phys. Stat. Sol. (b), V. 176, 459 (1993).

Santra K. and Sarkar C.K., Physics Letters A 153, 390 (1991).

Schmitt-Rink S., Miller D.A.B. and Chemla D.S., Phys. Rev. B 35, 8113 (1987)

Sarkar C.K. and Banerji P., Phys. Stat. Sol. (b), 156, K145 (1989).

Sarkar C.K. and Banerji P., J. Phys. Chem. Solids, v. 53, no.5, pp.713-715 (1992).

Sarkar C.K. and Chattopadhyah, Phys. Rev. B 19, 1121 (1979).

Sarkar C.K. and Chattopadhyay D., Phys. Stat. Sol (b) 88, K109 (1978).

Saxier A., Look D.C., Elhabri S., Sizelove J., Mitchel W.C., Sung C.M., Park S.S. and Lee K.Y., Appl. Phys. Lett. 78, 1872 (2001).

Sayed M.M. and Westgate C.R., Rev. Sci. Instrum 46, 1074 (1975).

Schiff L.I., "Quantum Mechanics", 3rd Edition, p.283, McGraw-Hill, New York, (1968).

Schrieffer J.R., Semiconductor Surface Physics (ed. R. H. Kingston, Univ. of Pennsylvania Press, Philadelphia p. 55 (1957).

Schulman J.N. and Efron U., J. Appl. Phys. 62, 4533 (1987)

Shakouri A. and Bowers John E., Appl. Phys. Lett. 71, 1234 (1997).

Shakouri A., LaBounty C., Proceedings of the 18th Intnat. Conf. of Thermoele., Baltimore, MD, p. 35-39, (1999).

Shakouri A., Lee E.Y., Smith D.L., Narayanamurti V., Bowers J.E., Microscale Thermophysical Engineering, Vol.2, No. 37 (1998).

Simon R., J. Appl. Phys. 33, 1830 (1962).

Solomon P.M. and Morkoc H., IEEE Trans. Electron. Dev ED31, 1015 (1984).

Spietzer W.G. and Fan H.Y., Phys. Rev. 106, 882 (1957).

Spicer W. E., Phys. Rev. 112, 114 (1958).

Spietzer W.G. and Fan H.Y., Phys. Rev. 106, 882 (1957).

Steigerwald Daniel, Rudaz Serge, Liu Heng, Kern R. Scott, Götz Werner and Fletcher Robert, JOM, 49, 18-23 (1997).

Stern F. and Howard W.E., Phys. Rev. 163, 816 (1987).

Suemune I. and Coldren L.A., IEEE J. Quan. Electron. 24, 1778 (1988).

Tsang W.T., Appl. Phys. Lett. 44, 288 (1984).

Tsubaki K., Sugimura A. and Kumabe K.K., Appl. Phys. Lett. 46, 764 (1985).

Venkatasubramanian R., Phys. Rev. B 61, 3091 (2000).

Venkatasubramanian R., Proceedings of the 18th Inter. Conf. of Thermoele., Baltimore, MD, p. 100-3, (1999).

Walkauska S.G., Broido D.A., Kempa K. and Reinecke T.L., J. Appl. Phys. 85, 2579 (1999).

Weimann N.G., Eastman L.F., Doppalapudi D., Ng H.M. and Moustakas T.D., J. Appl. Phys. 83, 3656 (1998).

Weisbuck C. and Nagle J., Science and Engineering of One and Zero Dimensional Semiconductors, Sp Beanmont and C.M. Sotomajor. Eds. NY, Plenum, 309 (1990).

Weisbuch C., in Semiconductors and Semimetals, Academic Press, 24., P-1 (1987).

Wilt D.P., Schwartz B., Tell B., Beebe E.D. and Nelson R.J., Appl. Phys. Lett. 44, 290 (1984).

Yariv A., Appl. Phys. Lett. 53, 1033 (1988).

Zhu Q.S., Nobuhiko S., Appl. Phys. Lett. 76, 1594 (2000).

Zook J.D., Phy. Rev. 136, A869 (1964).

Zou J., Kotchtkov D. and Balandin A.A., J. Appl. Phys. 92, 2534 (2002).

3.1 Introduction

GaN is a direct and large band gap compound semiconductor having the band gap of the order of 3.5 eV [Pankove and Moustakas, 1998]. GaN is an important material for applications in blue, violet and green light emitting diodes. Due to the strong bond strength it has also become the best candidate for high temperature transistors i.e. HEMT, LED etc.

Due to non-availability of single crystalline GaN substrate, it is normally grown on sapphire (Al_2O_3) or SiC substrate with a large lattice mismatch. The GaN grown on substrate sapphire having 14% lattice size mismatch and 34% mismatch in the thermal expansion coefficient [Look and Sizelove, 1999] has been selected for our work. The large lattice mismatch with the substrate as sapphire and GaN ($a_{sapphire}$=4.76 $\mathring{A}$ and a_{GaN}=3.18 $\mathring{A}$), causes heavy dislocations in the interfacial layer, the layer between GaN and the sapphire substrate. But, the density of dislocations decreases very fast as we move away from the interfacial layer towards the GaN epilayer, also called the bulk layer. However, the transport properties of the entire GaN material are dependent on the interfacial layer. Thus, the whole GaN epilayer is considered to be made up of two layers, as suggested by D.C. Look et al. [Look and Molnar, 1997]. The author developed a model, called the two-layer model [Look and Molnar, 1997]. According to the model, current passing through the epilayer of GaN gets divided into two layers as if two parallel resistors. The combined current will be the sum of the currents due to two individual layers. The model has been used to calculate different transport parameters, such as ac & dc mobilities, conductivities, Seebeck coefficient or thermoelectric power, thermal conductivity due to electrons and finally the figure of merit including the influence of various phonon and nonphonon scattering mechanisms. The lattice part of the thermal conductivity has been calculated assuming only single bulk layer with an average density of dislocations present in it. The total contribution to thermal conductivity is obtained by adding the lattice part to the electronic part, is evaluated assuming two-layer model similar to the other transport coefficients.

The Fig. 3.1 represents the schematic representation of the two-layer model of n-type GaN grown on sapphire. Fig. 3.1 represents the top or 1st layer as bulk layer of GaN, the 2nd layer is the interfacial layer. The bottommost layer is the substrate of sapphire which is an insulator layer so it does not take part in any electronic transport phenomena. Due to the high density of dislocations in the interfacial layer, transport properties in the layer are

highly affected by scattering due to the dislocation. Hence, scattering due to dislocation only will be dominant in the interfacial layer whereas various other types of scattering mechanisms are included for the bulk layer such as ionized impurity (ii), neutral impurity (in), acoustic phonon via deformation potential (dp) and piezoelectric scattering (pz). In the higher temperature region, the effect of polar optical phonon scattering mechanism (po) dominates the other scattering mechanisms. The influence of dislocation scattering in the bulk layer has not been considered because of the negligible density of dislocations as compared to that of the interfacial layer.

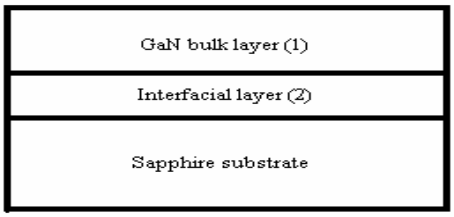

Fig. 3.1 Schematic representation of the model.

3.2 Theoretical Formulation

As mentioned in the section 3.1, before presenting the transport parameters of n-GaN using the two-layer model, a short description about calculations of the transport parameters is given,

3.2 (a) Transport Parameters

3.2 (a) i. Mobility

The mobility for electron in n-type material is given by [Nag, 1980],

$$\mu = \frac{e}{m^*}\langle\tau\rangle \qquad \ldots(3.1)$$

where e and m^* are magnitude of electronic charge and effective mass respectively. As the band gap of GaN is very large and direct, the band structure of GaN is taken to be spherical and parabolic.

The symbol $\langle\tau\rangle$, represents three dimensional k-space average of momentum relaxation time accounting various scattering mechanisms for a spherical and

parabolic band based on Maxwell-Boltzmann distribution function. In the present case GaN is assumed to be nondegenerate material [Look, 1989].

$$\langle \tau \rangle = \frac{\int_0^{\infty} E^{3/2} \tau(E) \frac{\partial f_0}{\partial E} dE}{\int_0^{\infty} E^{3/2} \frac{\partial f_0}{\partial E} dE} \qquad ..(3.2)$$

In the presence of low ac electric field with frequency ω', the momentum relaxation time in ac field is replaced by $\tau^{-1} = \left(\tau^{-1} + i\omega'\right)$ [Nag, 1980]. On substituting the ac relaxation time in the expression of mobility, we get the real (μ_r) and the imaginary (μ_{im}) parts of the ac mobility. The complex ac mobility is related to μ_r and μ_{im} as $\mu = \mu_r + i\mu_{im}$ where,

$$\mu_r = \frac{e}{m^*} \left\langle \frac{\tau}{\left(1 + \tau^2 \omega'^2\right)} \right\rangle \qquad ...(3.3)$$

$$\mu_{im} = \frac{e}{m^*} \omega' \left\langle \frac{\tau^2}{\left(1 + \tau^2 \omega'^2\right)} \right\rangle \qquad ...(3.4)$$

3.2 (a) ii. Electrical Conductivity

The electrical conductivity for n-GaN is obtained by replacing μ by σ/ne in equation (3.1),

$$\sigma = \frac{ne^2}{m*} \langle \tau \rangle \qquad ...(3.5)$$

where n is the concentration of electrons.

3.2 (a) iii. Seebeck Coefficient

Seebeck coefficient is another interesting transport parameter for device characterization and it gives information about the density of state, band structure and different scattering mechanisms. The calculation of thermoelectric power or Seebeck coefficient is based on the mobility theory and is derived from the Boltzmann transport equation. The thermoelectric power obtained from the Boltzmann transport equation is the difference between Fermi energy term and the scattering terms in the form of ratio. Hence is given as [Nag, 1980],

$$S = \frac{\xi}{\nabla_z T} = \frac{k_B}{e}\left[-\frac{E_F}{k_B T} + \frac{\langle \mathrm{E}\tau \rangle}{\langle \tau \rangle k_B T}\right] \qquad ...(3.6)$$

where E_F and E being Fermi energy and the electron energy for electrons respectively. k_B is the Boltzmann's constant, T being temperature in Kelvin.

3.2 (a) iv. Electronic Thermal Conductivity

Thermal conductivity due to the electrons can be expressed as [Smith, 1989],

$$\kappa_e = \sigma \mathrm{L} \mathrm{T} \qquad ...(3.7)$$

Where L, the Lorentz ratio is given as,

$$\mathrm{L} = \mathcal{L}\left(\frac{\mathrm{k_B^2}}{e^2}\right) \qquad ...(3.8)$$

$$\text{where } \mathcal{L} = \frac{\langle \tau \rangle \langle E^2 \tau \rangle - \langle E\tau \rangle^2}{k_B^2 T^2 \langle \tau \rangle^2} \qquad ...(3.9)$$

$\langle \tau \rangle$ has been already defined as given in equation (3.1). In the similar way $\langle E^2 \tau \rangle$ and $\langle E\tau \rangle$ are also obtained.

3.2 (a) v. Lattice Thermal Conductivity

Based on Callaway's phenomenological theory [Callaway, 1959] and Klemens' second-order perturbation theory formulae for phonon scattering rates [Klemens, 1958] the lattice thermal conductivity [Callaway, 1959] is given as,

$$\kappa_{latt} = \left(\frac{k_B}{\hbar}\right)^3 \frac{k_B}{2\pi^2 v} T^3 \int_0^{T_D/T} \frac{x^4 \tau_C e^x}{\left(e^x - 1\right)^2} \partial x \qquad ...(3.10)$$

Where v is an average sound velocity, $x = \hbar\omega / k_B T$, where ω is the phonon frequency. $\tau_C \equiv \tau_C(x)$, is the combined relaxation time and is written as $\tau_C^{-1} = \tau_{DC}^{-1} + \tau_D^{-1}$.

τ_D is the total momentum relaxation time due to edge dislocation scattering (E), screw dislocation scattering (S) and mixed dislocation scattering (M) [Klemens, 1958].

τ_{DC} is the phonon scattering rate at the core of dislocation [Klemens, 1955]. This model assumes Debye-like phonon density of states [Callaway, 1959].

3.2 (a) vi. Figure of Merit

The figure of merit of thermoelectric (Z) is also an important parameter for electronic devices such as refrigerator, generators and coolers etc. The value of ZT signifies the efficiency of a device. A good device is that one, which has highest value of ZT. Z has the dimension of inverse temperature and is defined [Harmon and Honig, 1961; Egli Ed., 1961; Rowe and Bhandari, 1983] as,

$$Z = S^2 \frac{\sigma}{\kappa} \qquad ...(3.11)$$

Thermal conductivity (κ) is the sum of thermal conductivity due to electrons (κ_e), given by equation (3.7) and due to the lattice (κ_{latt}), as given by equation (3.10).

3.2 (b) Transport Parameters based on Two Layer Model

Due to the mismatch between the epilayer of GaN and the sapphire layer, very large number of dislocations is present in the interfacial layer. The transport parameters are highly affected by these dense dislocations. It arises from the effect of band bending at a surface. In the case of epitaxial films it occurs in the interface as a result of trapped charges into the surfaces or in deep states in the substrate. According to the two-layer model, the combined current will be the sum of the currents through two individual layers, hence,

$$I_{com} = I_1 + I_2 \qquad ...(3.12)$$

Where I_1, I_2 and I_{com} are current in the bulk layer, the interfacial layer and the total current respectively.

Fig. 3.2, shows the side view and front view of the model. In the side view, the length of the sample is l for the both 1st layer or bulk layer and also for the 2nd layer or interfacial layer, whereas the thickness of 1st layer is w_1 and the 2nd layer is w_2. Front view diagram shows that the breadth of the sample is b, is also same for both the layers.

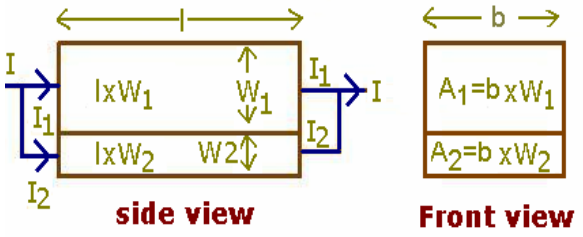

Fig. 3.2, Side view and Front view of the mode.

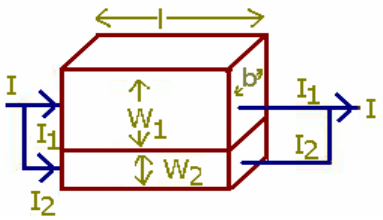

Fig. 3.3, Simplified diagram of the model.

Fig. 3.3 shows the simplified diagram where the current I is shown to be divided into I_1 and I_2 , while passing through the sample via 1st layer and the 2nd layer respectively. The I is defined by I_{com} in our formulation.

3.2 (b) i. Combined or Two Layer Mobility

We have, current density, $J = \frac{I}{A}$, $J = \sigma E$, $E = V/l$ and $\mu = \frac{v_e}{E}$ also $A = b \times w$

This leads to,

$$\therefore I = ne\mu VA/l \qquad ...(3.13)$$

where, A is the surface area perpendicular to the direction of the flow of the current. The current flows along the length, l of the sample, across which the voltage V is applied. Hence, E is the voltage gradient. v_e, b and w are the drift velocity of electrons, breadth and the width of the sample repectively.

Now, substituting the values of currents for the bulk layer, the interfacial layer and for the combined two layer with their respective parameters in equation (3.12) referring to Fig. 3.3, we get the combined mobility, μ_{com} as,

$$ne\mu_{com}\frac{V}{l}bW = n_1 e\mu_1 \frac{V}{l}bW_1 + n_2 e\mu_2 \frac{V}{l}bW_2$$

$$\text{or} \quad \mu_{com} = \frac{(n_1 a\mu_1 + n_2\mu_2)}{(n_1 a + n_2)} \qquad ...(3.14)$$

In equation (3.14) n and μ represent concentration of carriers and mobility respectively. The subscripts 1 and 2 are used for the bulk and the interfacial layers respectively. $a = (W_1/W_2)$: the ratio of the thicknesses of the bulk layer W_1 to the interfacial layer W_2.

The real and imaginary parts of ac mobility given by equations (3.3) and (3.4) have been evaluated for the bulk and the interfacial layers separately by assuming their respective dominant scattering mechanisms as explained earlier. Again, the combined two layer real part (μ_{rcom}) and the combined two layer imaginary part (μ_{imcom}) of the ac mobility are obtained as it has been carried out in the case of dc mobility.

3.2 (b) ii. Combined Conductivity

Substituting σ/ne for the mobility μ with their appropriate subscripts for the bulk and the interfacial layers in equation (3.14), the combined electronic conductivity, σ_{com} is obtained as,

$$\sigma_{com} = \frac{(a\sigma_1 + \sigma_2)}{(a+1)} \qquad ...(3.15)$$

where σ_1 and σ_2 are conductivities in the bulk layer and the interfacial layer respectively.

3.2 (b) iii. Combined Seebeck Coefficient

A temperature gradient along a conductor sets an e.m.f. even when no electric current flows. Hence, the Seebeck coefficient is given as,

$$S = \frac{V}{T} = \frac{IR}{T} = \frac{Il}{T\sigma A} = \frac{Il}{T\sigma Wb}$$

$$\text{or } I = \frac{ST\sigma bW}{l} \qquad ...(3.16)$$

where T is temperature in Kelvin. The voltage V applied across the sample is the product of current (I) and resistance (R). R is equal to $l/\sigma A$. l, σ and A are already defined earlier. Substituting the values of I with their appropriate parameters in equation (3.12) we get the combined Seebeck coefficient, S_{com} as,

$$S_{com} = \frac{S_1\sigma_1 a + S_2\sigma_2}{\sigma_1 a + \sigma_2} \qquad ...(3.17)$$

where S_1 and S_2 are the Seebeck coefficient of the bulk layer and the interfacial layer respectively.

3.2 (b) iv. Combined Electronic Thermal Conductivity

From equation (3.11), $\kappa = \sigma L\left(\frac{k_B}{e}\right)^2 T$

$$\text{or, } \sigma = \frac{\kappa}{L\left(k_B/e\right)^2 T} \qquad ...(3.18)$$

substituting the value of σ, as obtained above in equation (3.15) with their appropriate parameters, we get the combined thermal conductivity due to electrons, κ_{com}^{ele} is,

$$\kappa_{com}^{ele} = \frac{\left(\frac{\kappa_1 a}{L_1}\right) + \left(\frac{\kappa_2}{L_2}\right)}{\left(\frac{a}{L_1}\right) + \left(\frac{1}{L_2}\right)} \qquad ...(3.19)$$

where k_1 and k_2 are electronic parts of the thermal conductivity for the bulk layer and the interfacial layers respectively. L, the Lorentz ratio. The subscripts 1 and 2 show the parameters for bulk layer and the interfacial layer of GaN respectively.

3.2 (b) v. Total Thermal Conductivity

The lattice part of thermal conductivity is very high as compared to the electronic part of the thermal conductivity. Total thermal conductivity, κ_{total} is the sum of the thermal conductivity due to lattice and due to electrons as given by equations (3.10) and (3.19) respectively.

$$\kappa_{total} = \kappa_{latt} + \kappa_{com}^{ele} \qquad ...(3.20)$$

The two-layer model has considered the two assumed layers with different concentration of carries. Obviously, the electron concentration in the interfacial layer is much more higher than the bulk layer. Hence, the average concentration of carriers is used to calculate the phonon scattering rate assuming only the single layer of GaN instead of the proposed two layers.

3.2 (b) vi. Combined Figure of Merit

Substituting the values of combined Seebeck, S_{com} combined conductivity, σ_{com} and the total thermal conductivity, κ_{total} we get the combined figure of merit, which is given as below,

$$Z_{com} = S_{com}^{2} \frac{\sigma_{com}}{\kappa_{total}} \qquad ...(3.21)$$

3.3 Results and Discussions

The author has calculated the various transport properties such as mobility, Seebeck coefficient, thermal conductivity and figure of merit of n-GaN grown on sapphire substrate considering two-layer model. The various parameters of GaN is given in the table Parameters of GaN. The dislocation density in the interfacial layer ($n_{interdis}$), carrier concentrations in the bulk layer (n_{bulk}) and the interfacial layer (n_{inter}) are taken as $7\times10^{14} m^{-2}$ [Look and Sizelove, 1999], $9\times10^{22} m^{-3}$ and $7\times10^{24} m^{-3}$ respectively. The fitting parameters taken for the donor concentration, N_D and the compensated acceptor concentration, N_A are 9×10^{22} m^{-3} and 5.5×10^{22} m^{-3} respectively according to Huang [Huang, 2002]. We have used Erginsoy's [Ergisony, 1950] neutral impurity scattering formula. The various momentum relaxation time [Look, 1989] i.e. ionized impurity (ii), neutral impurity (in), piezoelectric phonon (pe), acoustic phonon via deformation potential (dp) and polar optical phonon (po) scattering mechanisms for bulk layer and dislocation scattering only for interfacial layer, due to high density of dislocation are used. The appropriate relations for the scattering mechanisms are given in **Appendix 3A**.

Fig. 3.4 presents the variation of dc Mobility with temperature for various scattering mechanisms, such as ionized impurity (ii), neutral impurity (in), acoustic phonon via deformation potential (dp), piezoelectric (pe) and polar optical phonon (po) scattering mechanisms individually. The Fig 3.4 also shows the variation of dc mobility for the bulk layer due to the resultant effect of the above scattering mechanisms and the interfacial layer mobility with the scattering due to dislocation only.

The variation of combined dc Mobility with temperature for

thickness ratio 1:1 and 24:1 with the same scattering mechanisms taken before for the bulk layer as ionized impurity (ii), neutral impurity (in) , acoustic phonon via deformation potential (dp), piezoelectric (pe) and polar optical phonon (po) scattering mechanisms and dislocation scattering only for the interfacial layer is given in Fig. 3.5.

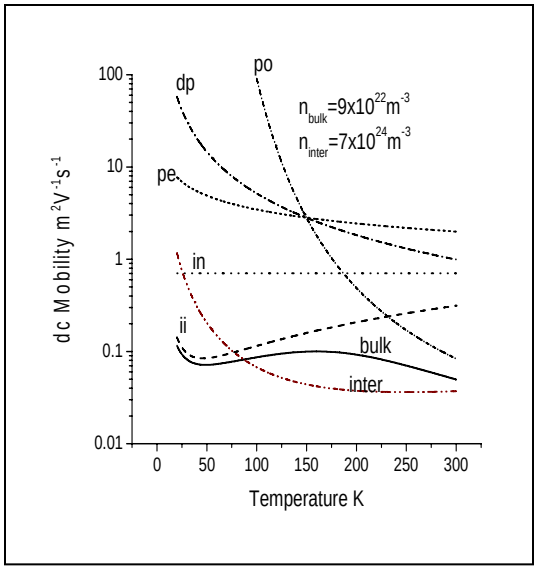

Fig. 3.4: Variation of dc Mobility with temperature for various scattering mechanisms such as ionized impurity (ii), neutral impurity (in), acoustic phonon via deformation potential (dp), piezoelectric (pe) and polar optical phonon (po) separately and the resultant of the all scattering mechanisms in the bulk layer and the interfacial layer mobility due to dislocating scattering only.

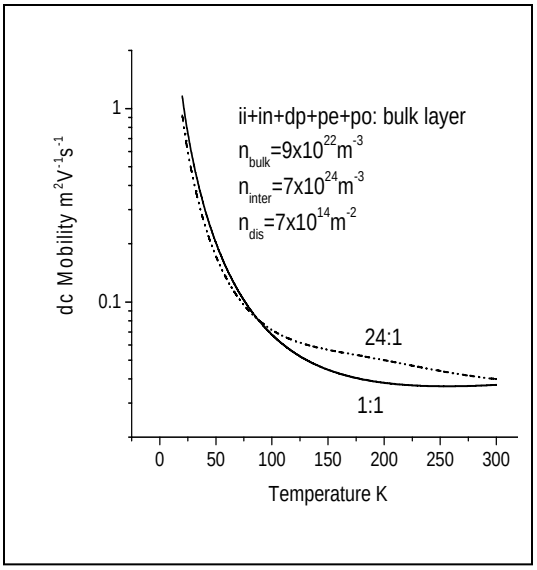

Fig. 3.5: Variation of dc combined Mobility versus temperature for layer thickness in the ratio 1:1 and 24:1 with ionized impurity (ii), neutral impurity (in), acoustic phonon via deformation potential (dp), piezoelectric (pe) and polar optical phonon (po) scattering mechanisms in the bulk layer and dislocation scattering only in the interfacial layer.

A comparative study has been carried out with the available experimental results [Brandt et al., 1998]. In Fig. 3.6, curves A, B, C and D are drawn for dc conductivity versus inverse of temperature (1000/K) with carriers concentration $2\times10^{24}m^{-3}$, as in the above mentioned paper of Brandt [Brandt et al., 1998]. By varying the concentration of carriers of the bulk layer and of the interfacial layer, the total normalized concentration is kept constant as given in the paper i.e. $2\times10^{24}m^{-3}$ and various curves A, B, C and D are plotted. Curve A, represents the conductivity with the carrier concentration of

the bulk and the interfacial layer $1.79\times10^{24}m^{-3}$ and $7\times10^{24}m^{-3}$ respectively with the thickness ratio of the bulk layer to the interfacial layer 24:1.

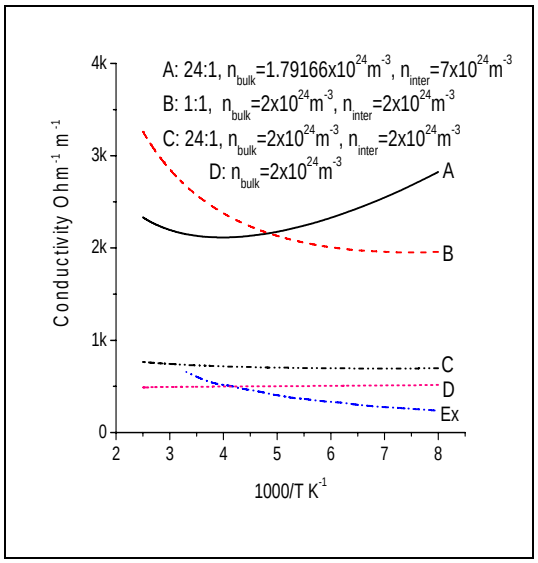

Fig. 3.6: Variation of dc combined Conductivity versus inverse of temperature with ionized impurity (ii), neutral impurity (in), acoustic phonon via deformation potential (dp), piezoelectric (pe) and polar optical phonon (po) scattering mechanisms in the bulk layer and dislocation scattering only in the interfacial layer for layer thickness in the ratio 24:1 and 1:1, represented by curves (A) and (B) respectively. The curves (C), (D) and (Ex) represent the variation for thickness ratio 24:1 with equal concentration of carriers in both the layers, the one-layer model and the experimental curve respectively.

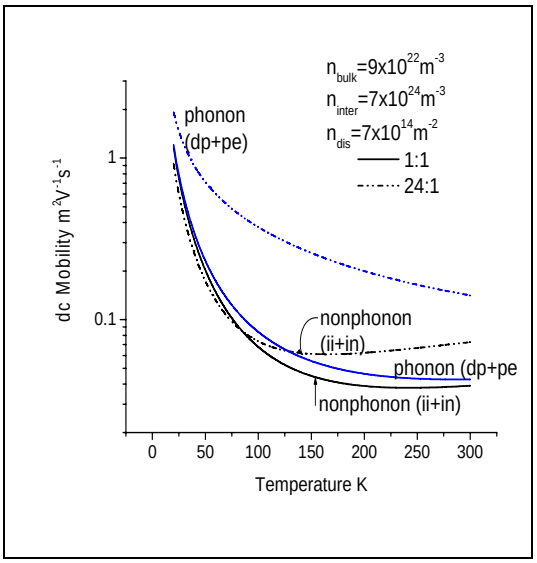

Fig. 3.7: Variation of dc combined Mobility versus temperature for the layer thickness in the ratio 1:1 and 24:1 for nonphonon (ionized impurity (ii) and neutral impurity (in)) and phonon (acoustic phonon via deformation potential (dp) and piezoelectric (pe)) scattering mechanisms separately in the bulk layer and dislocation scattering mechanism only is in the interfacial layer.

Whereas, curves B and C are plotted for the thickness ratio of the bulk layer to the interfacial layer 1:1 and 24:1 with the equal carrier concentration of $2\times10^{24}m^{-3}$ in both the layers. The curve D is plotted for the same concentration as that of B or C but considering only one layer i.e. n-GaN bulk layer only with all scattering mechanisms as ionized impurity (ii), neutral impurity (in), acoustic phonon via deformation potential (dp), piezoelectric

(pe) and polar optical phonon (po) scattering mechanisms in addition to the scattering due to dislocation. While calculating the scattering due to dislocation the average normalized carrier concentration due to the bulk layer and the interfacial layer is taken. For all the curves, the donor concentration of neutral impurity is taken $19\times10^{24}\,\mathrm{m}^{-3}$ as a fitting parameter. Fig. 3.6 shows that the magnitude of the conductivity due to curve C and D are closed to the experimental curve (Ex). However, the nature of the conductivity curve due to B is found to be more similar to that of the experimental curve (Ex). Hence, in the latter portion of our work we have given more importance for the two-layer model with the interfacial layer thickness equal to that of the bulk layer.

The variation of combined dc mobility with temperature for the thickness ratio 1:1 and 24:1 due to effect of nonphonon scattering mechanisms such as ionized impurity (ii) and neutral impurity (in) scatterings in the bulk layer and dislocation scattering only in the interfacial layer is shown in Fig. 3.7 . The Fig. 3.7 also shows the variation of combined dc mobility due to various types of phonon scattering mechanisms, such as acoustic phonon via deformation potential (dp) and piezoelectric scattering mechanisms in the bulk layer and dislocation scattering only in the interfacial layer. The Fig. 3.7 shows that the mobility due to phonon scattering mechanisms in the bulk layer in 24:1 thickness ratio is much higher than that of the mobility due to nonphonon scattering mechanisms. Whereas, in the case of 1:1 thickness ratio the mobility difference between phonon and nonphonon scattering mechanisms in the bulk layer is not much. It is expected due to the bulk mobility being dominated by the interfacial mobility and is constant in both the cases. At the same time we can also say that the mobility due to nonphonon scattering mechanisms dominates the mobility due to phonon scattering mechanisms in lower temperature regions.

Fig. 3.8 shows the variation of combined dc mobility with temperature for thickness ratio 1:1 and 24:1 due to the resultant effect of various scattering mechanisms such as ionized impurity (ii), neutral impurity (in), acoustic phonon via deformation potential (dp) and piezoelectric scattering mechanisms in the bulk layer and dislocation scattering only in the interfacial layer. The Fig. 3.8 also shows variation of combined dc mobility versus temperature due to polar optical phonon (po) scattering mechanism in bulk layer and dislocation scattering only in the interfacial layer. The Fig. 3.8 shows that the mobility in the thickness ratio 24:1, due to polar optical phonon scattering mechanism only is higher as compared to the resultant

effect of other scattering mechanisms in the bulk layer at the lower temperature region, whereas, the reverse nature is seen at the higher temperature region. It is expected due to bulk layer mobility dominating the interfacial layer mobility as the thickness ratio is 24:1 at the same time we can also conclude that the polar optical phonon scattering mechanism dominates the other scattering mechanism at the higher temperature region only.

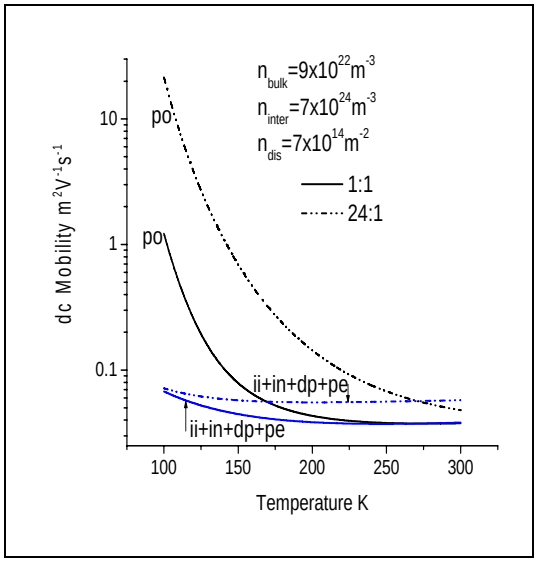

Fig. 3.8: Variation of dc combined Mobility versus temperature for the layer thickness in the ratio 1:1 and 24:1 for the resultant effect of ionized impurity (ii), neutral impurity (in), acoustic phonon via deformation potential (dp) and piezoelectric (pe) scattering mechanisms only, and polar optical phonon (po) scattering mechanism only in the bulk layer and dislocation scattering mechanism only is in the interfacial layer.

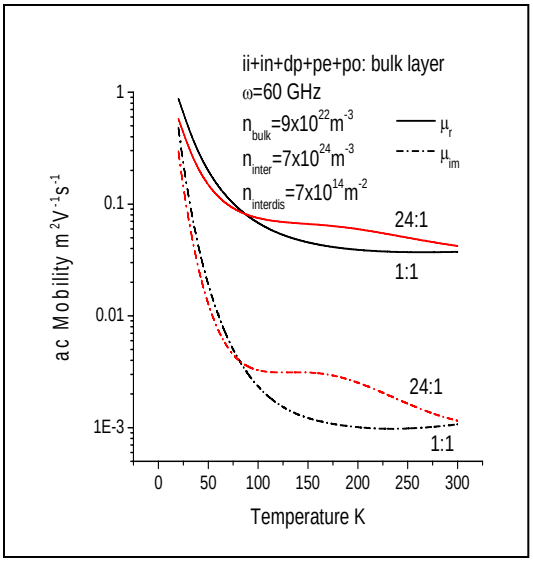

Fig. 3.9: Variation of ac combined Mobility with temperature for thickness ratio 1:1 and 24:1 at frequency 60 GHz with ionized impurity (ii), neutral impurity (in), acoustic phonon via deformation potential (dp), piezoelectric (pe) and polar optical phonon (po) scattering mechanisms in the bulk layer and dislocation scattering only in the interfacial layer.

The temperature dependent ac combined mobility is also studied and is shown in Fig. 3.9. The curve in the Fig. 3.9 shows the variation of ac combined mobility with temperature at a constant frequency of 60 GHz for thickness ratio 1:1 and 24:1 respectively with various scattering mechanisms such as ionized impurity (ii), neutral impurity (in), acoustic phonon via deformation potential (dp), piezoelectric (pe) and polar optical phonon (po)

scattering mechanisms in the bulk layer and dislocation scattering only in the interfacial layer.

Figs. 3.5 and 3.9 show both the dc and ac mobilities decrease with increase in temperature due to more scattering phenomenon becoming more active at higher temperatures. At temperatures above 100K polar optical phonon dominates the other scattering mechanisms, which further decreases the mobility in the bulk layer. It can be seen from Fig. 3.4 also. In the thickness ratio, 24:1 the combined mobility first increases and then decreases due to the mobility being dominated by the bulk layer mobility. Whereas, the interface mobility dominates the bulk mobility in the case of 1:1 ratio hence the mobility in the thickness ratio 1:1 decreases sharply with increasing temperature in lower temperature region.

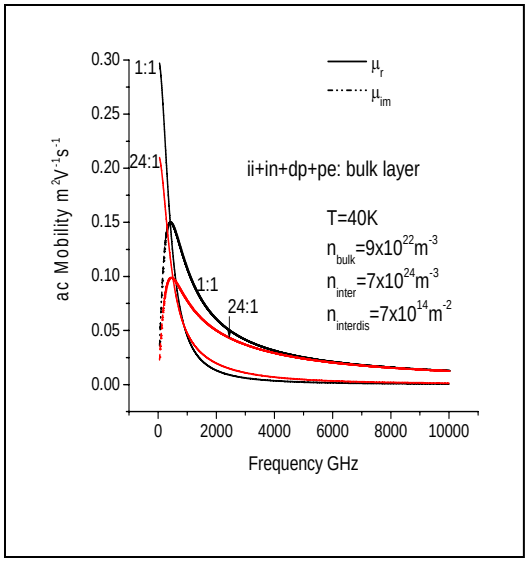

Fig. 3.10: Variation of ac combined Mobility with frequency for thickness ratio 1:1 and 24:1 at temperature 40K with ionized impurity (ii), neutral impurity (in), acoustic phonon via deformation potential (dp) and piezoelectric (pe) scattering mechanisms in the bulk layer and dislocation scattering only in the interfacial layer.

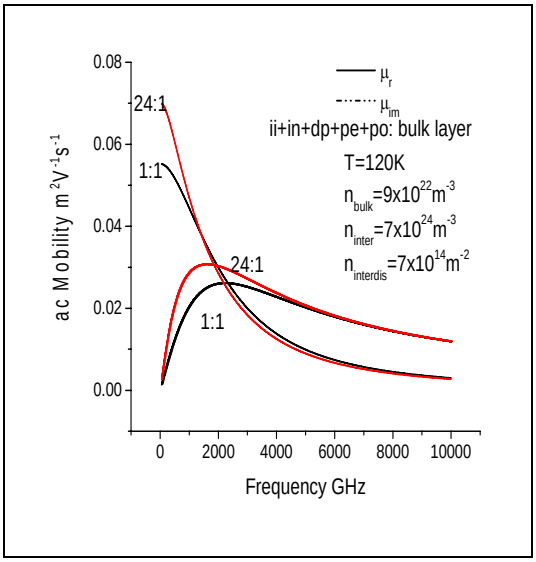

Fig. 3.11: Variation of ac combined Mobility with frequency for the thickness ratio 1:1 and 24:1 at temperature 120K with ionized impurity (ii), neutral impurity (in), acoustic phonon via deformation potential (dp), piezoelectric (pe) and polar optical phonon (po) scattering mechanisms in the bulk layer and dislocation scattering only in the interfacial layer.

The variation of combined real and imaginary parts of ac mobility with frequency is shown in Fig. 3.10, for the thickness ratio 1:1 and 24:1 respectively at temperature 40K with ionized impurity (ii), neutral impurity (in), acoustic phonon via deformation potential (dp) and piezoelectric (pe) scattering mechanisms in the bulk layer and dislocation scattering only in the interfacial layer. The figure shows both the real (μ_r) and imaginary (μ_{im}) parts of ac mobilities for 1:1 ratio is greater than that for 24:1. It is due to the interfacial mobility dominating the bulk mobility.

Similar study has been done for higher temperature including higher temperature scattering mechanism, the polar optical phonon (po) scattering is shown in Fig. 3.11. The Fig. 3.11 shows the variation of combined real and imaginary parts of ac mobility with frequency for the thickness ratio 1:1 and 24:1 at temperature 120K with ionized impurity (ii), neutral impurity (in), acoustic phonon via deformation potential (dp), piezoelectric (pe) and polar optical phonon (po) scattering mechanisms in the bulk layer and dislocation scattering only in the interfacial layer. The figure shows both the real (μ_r) and imaginary (μ_{im}) parts of ac mobilities for 24:1 ratio is greater than that for 1:1. This is due to the higher contribution of bulk layer mobility.

The epitaxial layer of GaN is considered to be two layers for the sake of transport characteristic calculation of GaN. The Fermi level for GaN can be calculated assuming a single eptilayer of GaN with normalized number of carriers per unit volume due to the bulk and the interfacial layers.

The another important calculation of transport parameter i.e. Seebeck coefficient is also calculated considering the two-layer model and is given in Figs. 3.12, 3.14 and 3.15. In the Fig. 3.12, the variation of modulus of combined Seebeck coefficient versus temperature is shown for the thickness in the ratio 24:1 and 1:1 with various types of scattering mechanisms such as ionized impurity (ii), neutral impurity (in), acoustic phonon via deformation potential (dp), piezoelectric (pe) and polar optical phonon (po) scattering mechanisms in the bulk layer and dislocation scattering only in the interfacial layer. The Fig. 3.12 shows the Seebeck coefficient for thickness ratio 24:1 is higher than that of the 1:1 ratio. This is due to the higher contribution of the Seebeck coefficient of the bulk layer. The Seebeck coefficient is a difference between the Fermi energy and the scattering terms in the form of ratio. The ratio term varies very slowly with temperature,

whereas, the Fermi energy decreases faster. Hence, the Seebeck coefficient for nondegenerate semiconductor is effectively determined by the Fermi energy. Obviously, the Fermi energy is a single energy level for the whole system because the two-layers model is an assumption only. Hence, we can say clearly that the scattering term in the form of ratio controls the magnitude of the combined Seebeck coefficient. Fig. 3.12 shows that the Seebeck coefficient increases with the increase in the temperature. The negative values of the Seebeck coefficient as observed is explained due to dominance of scattering ratio term compared to Fermi energy term.

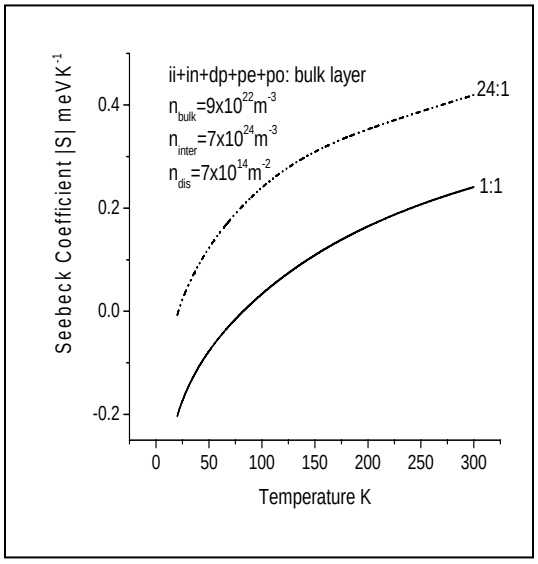

Fig.3.12: Variation of combined Seebeck coefficient versus temperature for layer thickness in the ratio 1:1 and 24:1 with ionized impurity (ii), neutral impurity (in), acoustic phonon via deformation potential (dp), piezoelectric (pe) and polar optical phonon (po) scattering mechanisms in the bulk layer and dislocation scattering only in the interfacial layer.

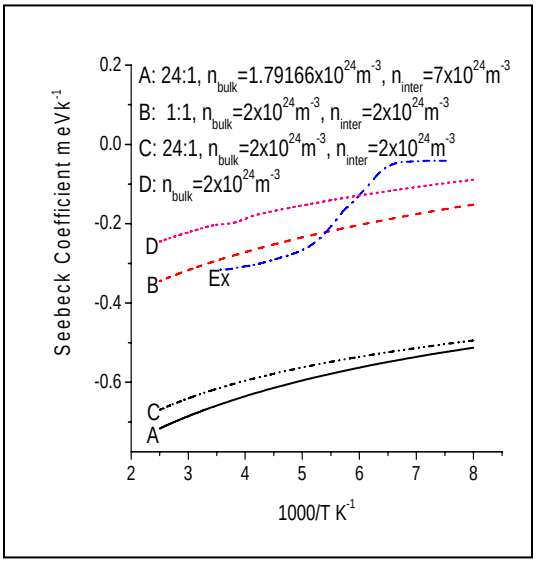

Fig. 3.13: Variation of combined Seebeck coefficient versus inverse of temperature with ionized impurity (ii), neutral impurity (in), acoustic phonon via deformation potential (dp), piezoelectric (pe) and polar optical phonon (po) scattering mechanisms in the bulk layer and only the dislocation scattering in the interfacial layer for layer thickness in the ratio 24:1 and 1:1, represented by curves (A) and (B) respectively. The curves (C), (D) and (Ex) represent the variation for thickness ratio 24:1 with equal concentration of carriers in both layer, the one-layer model and the experimental curve respectively.

One more comparative study has been done with the experimental available values [Brandt et al.,1998] with the same parameters as that used in Fig. 3.6 for various curves A, B, C and D. Fig. 3.13 shows variation of Seebeck coefficient versus inverse of temperature (1000/K) with the normalized concentration of carriers $2\times10^{24}m^{-3}$ with different combination of concentration of carriers in the bulk layer and in the interfacial layer. Curve A, represents the Seebeck coefficient with the carrier concentration of the bulk and the interfacial layer $1.79\times10^{24}m^{-3}$ and $7\times10^{24}m^{-3}$ respectively with the thickness ratio of the bulk layer to the interfacial layer 24:1. Whereas, curves B and C are plotted for the thickness ratio 1:1 and 24:1 respectively with the equal carrier concentrations of $2\times10^{24}m^{-3}$ in both the layers. The curve D is plotted for the same concentration as that of B and C but considering one layer i.e. $\mathrm{n\text{-}GaN}$ bulk layer only with all scattering mechanism as ionized impurity (ii), neutral impurity (in), acoustic phonon via deformation potential (dp), piezoelectric (pe) and polar optical phonon (po) scattering mechanisms plus the scattering due to dislocation with the normalized density of dislocations due to the bulk layer and the interfacial layer as done earlier in case of conductivity. For all the curves the donor concentration of the carriers of neutral impurity is taken $19\times10^{24}\mathrm{m}^{-3}$ as fitting parameter. Fig. 3.13 shows that the magnitude of Seebeck coefficient due to curve B and D are near the experimental curve (Ex). The agreement of curve B and D with the experimental results also suggests the inclusion of the interfacial layer, which is very essential while calculating various parameters of n-GaN grown on sapphire.

The agreement of the results of curve B with the experimental results (Ex) as shown in Fig. 3.6 and Fig. 3.13 for conductivity and the Seebeck coefficient respectively, also justify the two-layer model.

As discussed earlier, the Fig. 3.14 shows the variation of combined Seebeck coefficient with temperature for thickness ratio 1:1 and 24:1 with nonphonon scattering mechanisms such as ionized impurity (ii) and neutral impurity (in) scatterings in the bulk layer and dislocation scattering only in the interfacial layer. The Fig. 3.14 also shows variation of Seebeck coefficient due to resultant various phonon scattering mechanisms such as acoustic phonon via deformation potential (dp) and piezoelectric (pe) scattering mechanisms in bulk layer and dislocation scattering only in the interfacial layer.

Similarly, the Fig. 3.15 also shows the variation of combined two-layer Seebeck Coefficient with temperature for the thickness ratio 1:1 and 24:1 for various scattering mechanisms such as ionized impurity (ii), neutral impurity (in), acoustic phonon via deformation potential (dp) and piezoelectric (pe) in the bulk layer and dislocation scattering only in the interfacial layer. The same Fig. 3.15 shows the variation of Seebeck coefficient due to only polar optical phonon scattering mechanism (po) in the bulk layer and dislocation scattering only in the interfacial layer.

All the Figs. 3.12, 3.14 and 3.15 presented above for Seebeck coefficient versus temperature show the similar nature that Seebeck coefficient increases with the increase in the temperature.

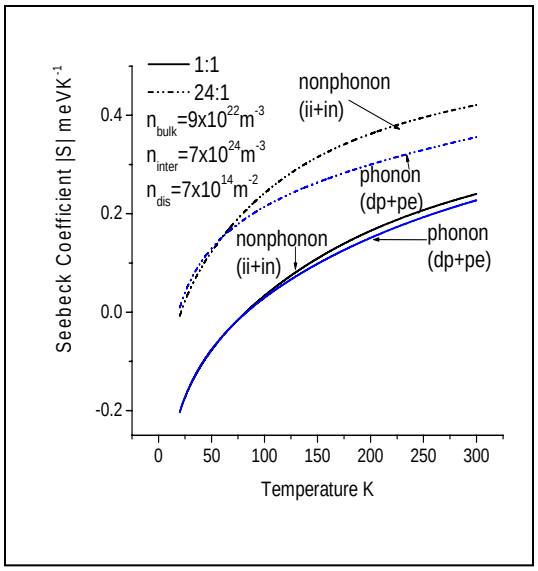

Fig. 3.14: Variation of combined Seebeck Coefficient versus temperature for the layer thickness in the ratio 1:1 and 24:1 for phonon (ionized impurity (ii) and neutral impurity (in)) and nonphonon (acoustic phonon via deformation potential (dp) and piezoelectric (pe)) scattering mechanisms separately in the bulk layer and dislocation scattering mechanism only in the interfacial layer.

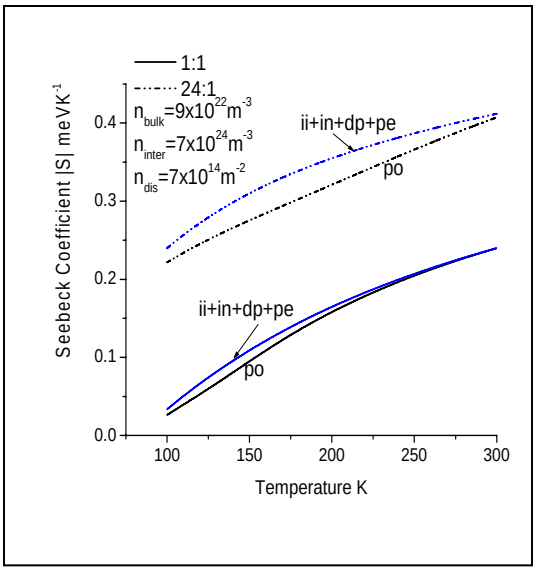

Fig. 3.15: Variation of combined Seebeck Coefficient versus temperature for the layer thickness in the ratio 1:1 and 24:1 for resultant effect of various scattering mechanisms such as ionized impurity (ii), neutral impurity (in), acoustic phonon via deformation potential (dp) and piezoelectric (pe) only, and polar optical phonon (po) only in the bulk layer and dislocation scattering mechanism only in the interfacial layer.

The next important parameter for transport is shown in Fig 3.16. The Fig. 3.16 shows the variation of combined thermal conductivity due to electrons versus temperature for the thickness in the ratio 1:1 and 24:1 with ionized impurity (ii), neutral impurity (in), acoustic phonon via deformation potential (dp), piezoelectric (pe) and polar optical phonon (po) scattering mechanisms in the bulk layer and the dislocation scattering in the interfacial layer only.

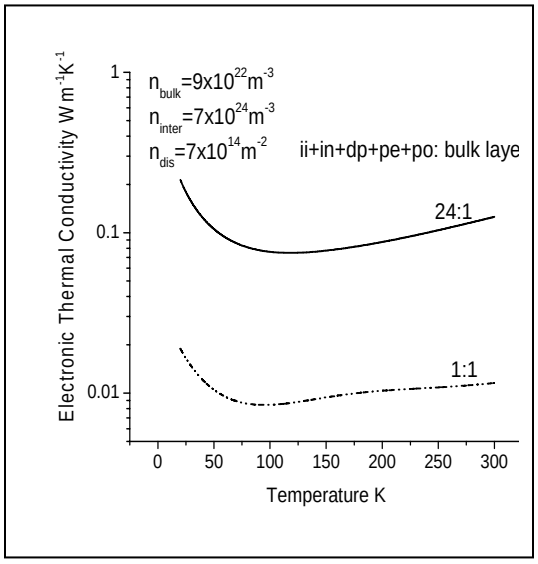

Fig. 3.16: Variation of combined Electronic Thermal Conductivity versus temperature for layer thickness in the ratio 1:1 and 24:1 with ionized impurity (ii), neutral impurity (in), acoustic phonon via deformation potential (dp), piezoelectric (pe) and polar optical phonon (po) scattering mechanisms in the bulk layer and dislocation scattering only in the interfacial layer.

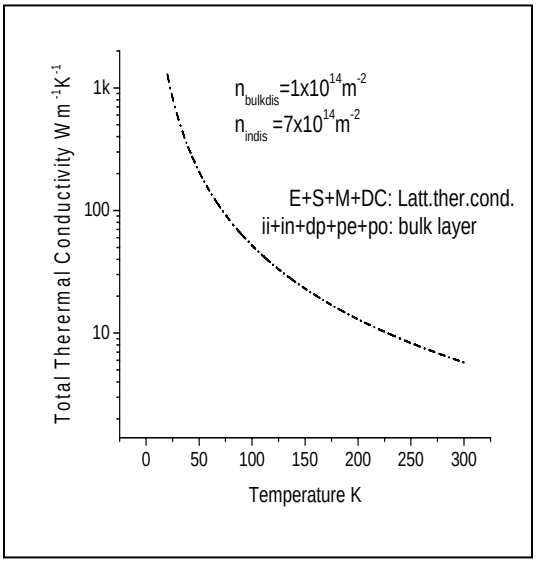

Fig. 3.17: Variation of Total Thermal Conductivity due to lattice and combined electronic thermal conductivity versus temperature with ionized impurity (ii), neutral impurity (in), acoustic phonon via deformation potential (dp), piezoelectric (pe) and polar optical phonon (po) scattering mechanisms in the bulk layer and dislocation scattering in the interfacial layer. The phonon scattering rates due to edge (E), screw (S), mixed (M) dislocations along with the dislocation core (DC) are used for lattice thermal conductivity.

The atoms in lattice also take part in the transport processes. The atoms in lattice are not mobile as electrons due to their heavy mass but get vibrate easily at sufficient temperatures, hence, the atoms conduct heat in the form of vibration, which is the thermal conductivity due to lattice atoms. Hence, is called lattice thermal conductivity. The lattice thermal conductivity is found to

be much more than that of electronic thermal conductivity. Here, the author has shown in the Fig. 3.17 the variation of total thermal conductivity i.e. the sum of thermal conductivity due to lattice and the combined thermal conductivity due to electron, versus temperature for the thickness in the ratio 1:1 and 24:1 with ionized impurity (ii), neutral impurity (in), acoustic phonon via deformation potential (dp) piezoelectric (pe) and polar optical phonon (po) scattering mechanisms in the bulk layer and dislocation scattering only in the interfacial layer. The phonon scattering rates due to edge (E), screw (S), mixed (M) dislocations are taken along with the rate of phonon scattering on dislocation core (DC) for lattice thermal conductivity. The normalized total density of dislocations is taken $4\times10^{14}m^{-2}$ due to the density of dislocations in the bulk layer and in the interfacial layer of the order of $1\times10^{14}m^{-2}$ [Kotchetkov et al. 2002] and $7\times10^{14}m^{-2}$ [Look and Sizelove, 2002] respectively.

Fig. 3.18 shows the variation of the Z_eT with temperature for the ratio of the thickness in 1:1 and 24:1 with ionized impurity (ii), neutral impurity (in), acoustic phonon via deformation potential (dp), piezoelectric (pe) and polar optical phonon (po) scattering mechanisms in the bulk layer and only the dislocation scattering in the interfacial layer. Here, the thermal conductivity due to electron only is taken. Fig. 3.18 shows the value for the thickness ratio 1:1 is greater than that of 24:1.

While calculating the Figure of merit, Z the contribution of the lattice thermal conductivity is found to be very important because the lattice atoms once get heated vibrate and contribute in the heat thermal process. Hence, now onwards our result includes the lattice thermal conductivity along with the electronic thermal conductivity. Fig. 3.19 shows the variation of the ZT with temperature for the ratio of the thickness in 1:1 and 24:1 with ionized impurity (ii), neutral impurity (in), acoustic phonon via deformation potential (dp), piezoelectric (pe) and polar optical phonon (po) scattering mechanisms in the bulk layer and dislocation scattering only in the interfacial layer. Fig. 3.19 shows the value of Z for thickness ratio 1:1 is greater than that of 24:1.

Fig. 3.20 shows the variation of ZT versus temperature for the thickness in the ratio 1:1 and 24:1 due to the effect of nonphonon scattering i.e. ionized impurity (ii) and neutral impurity (in) scattering mechanisms in the bulk and the dislocation scattering in the interfacial layer. Fig. 3.20 also shows the variation of combined ZT due to various phonon scattering mechanisms such

as acoustic phonon via deformation potential (dp) and piezoelectric (pe) scattering mechanisms in the bulk layer and the dislocation scattering only in the interfacial layer.

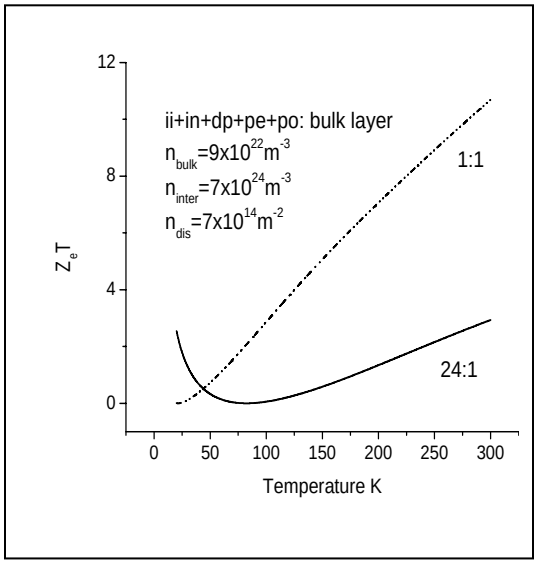

Fig. 3.18: The variation of combined Z_eT versus temperature for layer thickness in the ratio 1:1 and 24:1 with ionized impurity (ii), neutral impurity (in), acoustic phonon via deformation potential (dp), piezoelectric (pe) and polar optical phonon (po) scattering mechanisms in the bulk layer and dislocation scattering only in the interfacial layer with electronic thermal conductivity only.

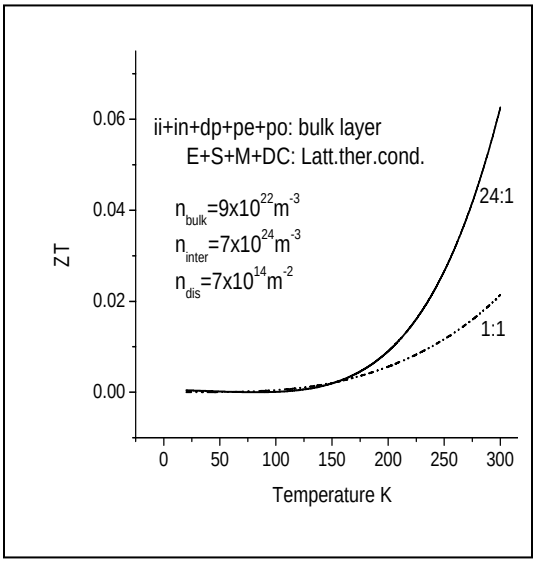

Fig. 3.19: The variation of combined ZT versus temperature for the layer thickness in the ratio 1:1 and 24:1 with ionized impurity (ii), neutral impurity (in), acoustic phonon via deformation potential (dp), piezoelectric (pe) and polar optical phonon (po) scattering mechanisms in the bulk layer and dislocation scattering only in the interfacial layer. The phonon scattering rates due to edge (E), screw (S), mixed (M) dislocations along with the dislocation core (DC) are used for lattice thermal conductivity.

Finally, the author has compared the result with high temperature dominating scattering mechanism, polar optical phonon (po) scattering mechanism with other low temperature scattering mechanism which is shown in Fig. 3.21. The Fig. 3.21 shows the variation of ZT versus temperature for the thickness in the ratio 1:1 and 24:1 with the net effects of various scattering mechanisms such as ionized impurity (ii), neutral impurity (in), acoustic phonon via deformation potential (dp) and piezoelectric (pe) scattering mechanisms in

the bulk layer and dislocation scattering mechanism only in the interfacial layer. The Fig. 3.21 also shows the variation of ZT with temperature for the scattering due to polar optical phonon (po) in the bulk layer and dislocation scattering in the interfacial layer.

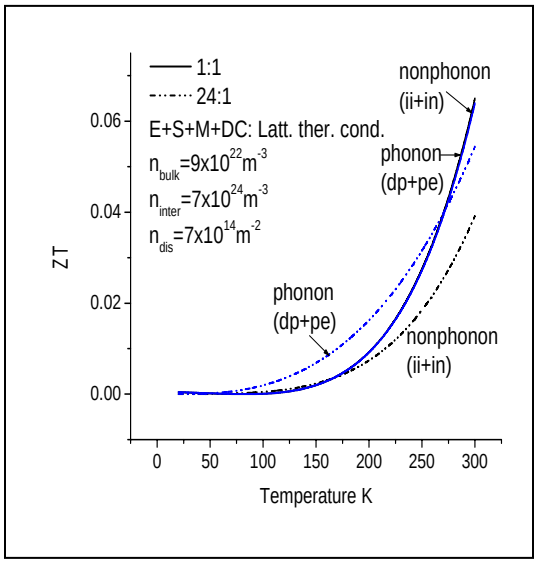

Fig. 3.20: Variation of combined ZT versus temperature for the layer thickness in the ratio 1:1 and 24:1 for phonon (ionized impurity (ii) and neutral impurity (in)) and nonphonon (acoustic phonon via deformation potential (dp) and piezoelectric (pe)) scattering mechanisms separately in the bulk layer and dislocation scattering mechanism only is in the interfacial layer. The phonon scattering rates due to edge (E), screw (S), mixed (M) dislocations along with the dislocation core (DC) are used for lattice thermal conductivity.

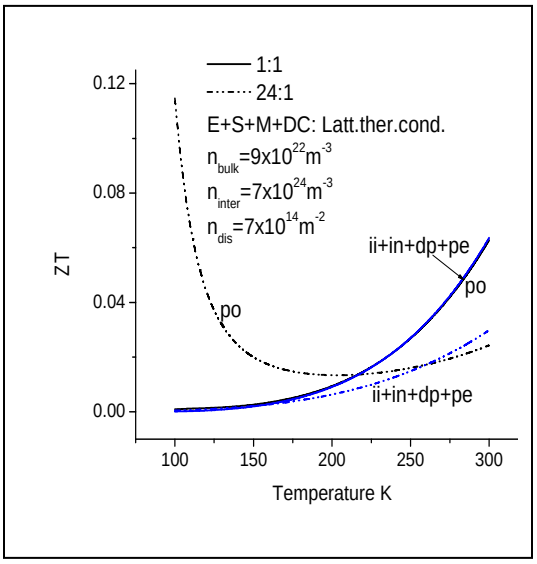

Fig. 3.21: Variation of combined ZT versus temperature for the layer thickness in the ratio 1:1 and 24:1 for various scattering mechanisms such as ionized impurity (ii), neutral impurity (in), acoustic phonon via deformation potential (dp) and piezoelectric (pe) only and polar optical phonon (po) only in the bulk layer and dislocation scattering mechanism only is in the interfacial layer. The phonon scattering rates due to edge (E), screw (S), mixed (M) dislocations along with the dislocation core (DC) are used for lattice thermal conductivity.

Figs. 3.19, 3.20 and 3.21, show that ZT increases with the increase of temperature which is expected due to ZT, being a function of temperature (T), Seebeck coefficient (S), electronic conductivity (σ) and thermal conductivity (κ). S increases with the rise in temperature as shown by Figs.

3.12, 3.14 and 3.15 also, whereas the thermal conductivity in the denominator decreases with rise in temperature shown by Fig. 3.17 due to which over all ZT increases as the temperature increases.

3.4 Conclusions

On the basis of the two-layer model, formulated by Look the author has calculated various electronic transport properties of the GaN, grown on sapphire such a mobility, Seebeck coefficient, thermal conductivity and figure of merit. The lattice thermal conductivity is also calculated considering only a bulk epilayer of GaN, but with an average number of the total carrier concentration combining the bulk and the interface layers. The obtained values are compared with available experimental result. It was found that the values and the trend of the curve of the various electronic parameters are found to be closer to the experimental data when we consider the interfacial layer having the thickness as equal as that of the bulk layer. Hence the presence of the interfacial layer cannot be ignored.

Various methods were performed to separate the electronic properties of the different layers in such GaN grown epitaxially [Huang et al., 2001] but we found that the two-layer model as is suggested by D. C Look strongly supports the experimental results.

References

Brandt M.S. , Herbst P., Angerer H., Ambacher O. and Stutzmann M., Phys. Rev. B 58, 7786 (1998).

Callaway J., Phys. Rev. 113,1046 (1959).

Egli P.Ed., Thermoelectricity (Wiley, New York) (1961).

Erginsoy C., Phys. Rev. 79, 1013 (1950).

Harmon C. and Honig J.M., J. Appl. Phys. 33, 3178-3188 (1962).

Huang Y., Temperature Dependent Hall Effect Studies of GaN on Sapphire, M. Phil. Thesis, The University of Hong Kong, (2002).

Huang D., Yun F., Reshchikov M.A., Wang D., Morkoc H., Rode D.L., Farina L.A., Kurdak C., Tsen K.T., Park S.S. and Lee K.Y., Solid-State Electronics 45, 711-715 (2001).

Klemens P.G., in Solid State Physics, ed. by F.Seitz and D.Turnbull (Academic New York) Vol.7 (1958).

Klemens P.G., Proc. Phys. Soc LXIII, 12-A, 73 (1955).

Kotchetkov Dmitri, Zou Jie and Balandin A. Alexander, Mat. Res. Soc. Symp. Proc. Vol. 731, W5.11.1 (2002).

Look D.C. and Molnar R. J., Appl. Phys. Lett. 70, 3377 (1997).

Look D.C., Electrical Characterization of GaAs Materials and Devices (Johan and Sons Ltd., NY) (1989).

Look D.C. and Sizelove J.R., Phys. Rev. Lett. 82, 1237 (1999).

Nag B.R., Electron Transport in Compound semiconductors, Springer Series in Solid State Sciences, ed. by M.Cardona, P.Fulde and H.J.Ouessier (Springer, Berlin) (1980).

Pankove J.I. and Moustakas T.D., Gallium Nitride GaN I. ed. by (Academic, New York, pp.175 (1998).

Rowe D.M. and Bhandari C.M., Modern Thermoelectrics (Reston, Reston VA), (1983).

Smith R.A., Semiconductors, Academic Publishers, IInd edition pp.147 (1989).

Parameters of GaN: Table 3.1

Quantity	Magnitude	Units	References
Plank's constant $\hbar$	1.055×10^{-34}	J-s	Nag, 1980
Debye temperature T_D	1044	K	Rode, 1975
Dielectric permittivity ε_0	8.85418×10^{-12}	F/m	Nag, 1980
ε_∞	$5.47\varepsilon_0$	F/m	Lin et al., 1993
ε	$10.4\varepsilon_0$	F/m	Wang et al., 1996
Electronic charge e	1.602×10^{-19}	C	Nag, 1980
Effective mass $m^*(4K)$	$0.22(9.109\times10^{-31})$	Kg	Perlin, 1996
$c_L \equiv \rho s^2$	1.45×10^{11}	N/m^2	Nag, 1980
$P \equiv \left(h_{pz}^2 / \rho s^2 \varepsilon\right)^{1/2}$	0.052	Unitless	Nag, 1980
averaged velocity of sound S	6.59×10^3	ms^{-1}	Rode, 1975
k_B	1.380×10^{-23}	J/deg	Nag, 1980
Mass density ρ	6.10×10^3	Kgm^{-3}	Schroeder, 1990
Piezoelectric constant $h_{pz}(\varepsilon_{14})$	$0.5(0.375-0.6)$	Cm^{-2}	Bykhovski, 1996
Acoustic phonon via pote. Def. E_1	9.2	eV	Shan, 1996
Lattice Constant a	3.189	$\overset{o}{A}$	Nakamura, 2000
Lattice Constant c	5.185	$\overset{o}{A}$	Nakamura, 2000
Volume per atom V_o	11.42	$\overset{o}{A}^3$	Zou et al., 2002
Gruneisen parameter γ	0.74		Witek, 1998
Longitudinal elastic constant C_L	265	GPa	Kotchetkov et al., 2001
Transverse elastic constant C_T	44.2	GPa	Kotchetkov et al., 2001

Effective Bohrs radius a_o	24	$\overset{o}{A}$	
Longitudinal sound velocity v_L	6560	ms^{-1}	Zou et al., 2002
Transverse sound velocity v_T	2680	ms^{-1}	Zou et al., 2002
Polarization averaged velocity v	3338	ms^{-1}	Zou et al., 2002
Poisson's ratio λ	0.37		Kotchetkov et al., 2001

References for parameters

Bykhovski A.D., Kaminski V.V., Shur M.S., Chen Q.C. and Khan M.A., Appl. Phys. Lett. 68, 818 (1996).

Kotchetkov D., Zou J., Balandin A.A., Florescu D.I. and Pollak H. Fred, Appl. Phys. Lett. 79, 4316 (2001).

Lin M.E., Sverdiov B.N., Strite S., Morkoc H. and Drakin A.E., Electronics Lett. 29, 1759 (1993).

Nakamura S., Pearton S. and Fasol G., in The Blue Laser Diode: The Complete Story Springer Berlin) (2000); Bougrov V., Levinshtein M., Rumyantsev S.L. and Zubrilov A., Properties of Advanced Semiconductor Materials, edited by M.E. Levinshtein, S.L. Rumyantsev, M.S. Shur, (Wiley, New Your, 2001): S. Strite and H. Markoc J. Vac. Sci. Technol. B 10, 1237 (1992).

Perlin P., Staszewska E.L. and Suchanek B., Appl. Phys. Lett. 68, 1114 (1996).

Rode D.L., Semiconductor and Semimetals, 10 1 (1975).

Schroeder D.K., Semiconductor Material and Device Characterization, Wiley New Your (1990).

Shan W., Schmidt T., Yang X.H., Song J.J. and Goldenberg B., J. Appl. Phys. 79, 3691 (1996).

Wang Y.J., Kaplan R., Ng H.K., Doverspike K., Gaskill D.K., Ikedo T., Amano H., and Akasaki I., J. Appl. Phys. 79, 8007 (1996).

Witek A., Diamond Related Mater. 7, 962 (1998).

Zou J., Kotchetkov D., Balandin A.A., Florescu D.I. and Pollak H. Fred, J. Appl. Phys. 92, 2534 (2002).

Appendix 3A

Different Scattering Mechanisms in the Bulk Layer [Look D.C. 1989]

(i) Ionized impurity

Ionized impurities scatter electrons through their screened Columb potential, given as

$$\Delta V = \frac{Ze^2}{4\pi\varepsilon r} e^{-r/\lambda_D}$$

where Ze is the ionic charge and λ_D is the Debye length in the non-degenerate case

$$\frac{1}{\tau_{ii}(\xi)} = \frac{N_1 Z^2 e^4 \left[\ln(1+y') - \frac{y'}{(1+y')} \right]}{16\sqrt{2}\pi\varepsilon^2 m^{*\frac{1}{2}} \xi^{\frac{3}{2}}}$$

$$y' = \frac{8\varepsilon m^* (k_B T)\xi}{\hbar^2 e^2 n} \ldots\ldots (3A.1)$$

Where $N_1 = 2N_A + n$ and N_A is the compensated acceptor concentration, is a very important fitting parameter, n is the free carriers concentration.

(ii) Neutral Impurities

Erginsoy derived a formula, is independent of energy.

$$\frac{1}{\tau_{in}(\xi)} = \frac{20 N_n \hbar a_o}{m^*} \ldots\ldots (3A.2)$$

Later Sclar considered the additional 'resonant' scattering due to the possibility of negative-ion formation and derived the following formula, where a_o is the effective Bohr radius of the donor and N_n is the concentration of neutral impurities, $N_n = N_D - N_A - n$

$$\frac{1}{\tau_{in}(\xi)} = \frac{\pi N_n e^4}{2^{1/2} m^{*1/2} \xi^{3/2}} \left[\ln(1+k\lambda_D)^2 - \frac{1}{(1+k^{-2}\lambda_D^{-2})} \right] \ldots\ldots (3A.3)$$

(iii) Optical Phonon: Polar

When,

$$0 \le T_{po}/T \le 5 \left(210 \le T \le \infty\right)$$

$$\chi\left(T_{po}/T\right) = 1 - 0.5841\left(T_{po}/T\right) + 0.2920\left(T_{po}/T\right)^2 - 0.03716\left(T_{po}/T\right)^3 .....(3A.4)$$

when,

$$5 \le T_{po}/T \le \infty \left(0 \le T \le 210\right)$$

$$\chi\left(T_{po}/T\right) = \frac{3\pi^{1/2}}{8}\left(T_{po}/T\right)^{1/2} .....(3A.5)$$

The respective relaxation time is written as, Ehrenreich,

$$0 \le \frac{T_{po}}{T} \le 5 :$$

$$\frac{1}{\tau_{po}} = \frac{e^2\left(k_B T_{po}\right) m^{*1/2}\left(\varepsilon_\infty^{-1} - \varepsilon^{-1}\right)\xi^{-1/2}}{2^{3/2}\pi\hbar^2\left(e^{T_{po}/T} - 1\right)\chi\left(\frac{T_{po}}{T}\right)}$$

$$5 \le \frac{T_{po}}{T} \le \infty$$

$$\frac{1}{\tau_{po}} = \frac{e^2\left(k_B T_{po}\right)^{1/2} m^{*1/2}\left(\varepsilon_\infty^{-1} - \varepsilon^{-1}\right)}{2^{3/2}\pi\hbar^2\left(e^{T_{po}/T} - 1\right)} ..... \left(3A.6\right)$$

(iv) Acoustic phonons: piezoelectric potential

$$\frac{1}{\tau_{pe}(\xi)} = \frac{\left(\frac{eh_{pz}}{\varepsilon}\right)^2 m^{*(1/2)}\left(k_B T\right)}{2\sqrt{2}\pi\hbar^2\rho s^2}\xi^{-1/2} = \frac{e^2P^2m^{*1/2}\left(k_B T\right)}{2\sqrt{2}\pi\hbar^2\varepsilon}\xi^{-1/2} .....(3A7)$$

where h_{pz} is the piezoelectric constant and $P = \left(h_{pz}^2/\rho s^2\varepsilon\right)^{1/2}$ is the piezoelectric coupling coefficient. ρ is the crystal density, s is the properly averaged velocity of sound, and E_1 is the deformation potential. Here $\rho s^2 \equiv c_l$, the longitudinal elastic constant.

(v) Acoustic phonon: deformation potential

$$\frac{1}{\tau_{dp}(\xi)} = \frac{\sqrt{2}E_1^{\,2} m^{*3/2}(k_B T)}{\pi\hbar^4 \rho s^2}\xi^{1/2} \ldots\ldots (3A.8)$$

Where, E_1 is the deformation potential

Scattering Mechanisms in the interfacial layer

Dislocation Scattering

Bonch-Bruevich and Kogan solved Poisson's equation in cylindrical coordinates and obtained the relaxation time.

$$\frac{1}{\tau_{disl}} = \frac{N_{disl} e^4 f^2 L_D}{8(\varepsilon\varepsilon_o)^2 a^2 m^{*2} (v_t^{\,2} + \hbar^2/4m^{*2} L_D^{\,2})^{3/2}} \ldots\ldots (3A.9)$$

Where V_t is the component V of perpendicular to the dislocation lines, a is the distance between imperfection centers.

Matthiessen's rule,

The total momentum relaxation time is,

$$\tau^{-1} = \sum_i \tau_i^{-1} \ldots\ldots (3A.10)$$

In the above equations τ_i is individual momentum relaxation time for different scattering mechanisms.

Scattering mechanisms for thermal conductivity due to lattice [Klements P.G., 1958]

The phonon scattering rate at the core of the dislocation is given by,

$$\frac{1}{\tau_{DC}} = \eta N_D \frac{V_0^{4/3}}{v^2}\omega^3 \ldots. (3A.11)$$

Where N_D is the density of the dislocation lines of all types, and η is the weight factor to account for the mutual orientation of the temperature gradient and the dislocation line. $\eta = 0.55$ {if dislocations are completely

random in respect to the temperature gradient [Kotchetkov, Zou and Balandin 2002]}. Since the strength of the acoustic phonon interaction with the elastic strain produced by dislocations depends on the magnitude and orientation of Burgers vector, the phonon scattering rates on screw $(1/\tau_s)$ and edge $(1/\tau_E)$ and mixed $(1/\tau_M)$ dislocations can be written as:

$$\frac{1}{\tau_S} = \frac{2^{3/2}}{3^{7/2}} \eta N_D^S b_S^2 \gamma^2 \omega \quad \text{.....(3A.12)}$$

$$\frac{1}{\tau_E} = \frac{2^{3/2}}{3^{7/2}} \eta N_D^E b_E^2 \gamma^2 \omega \left\{ \frac{1}{2} + \frac{1}{24} \left(\frac{1-2\upsilon}{1-\upsilon} \right)^2 \left[1 + \sqrt{2} \left(\frac{v_L}{v_T} \right)^2 \right]^2 \right\} \quad \text{.....(3A.13)}$$

$$\frac{1}{\tau_M} = \frac{2^{3/2}}{3^{7/2}} \eta N_D^M \gamma^2 \omega \left(b_S^2 + b_E^2 \left\{ \frac{1}{2} + \frac{1}{24} \left(\frac{1-2\upsilon}{1-\upsilon} \right)^2 \left[1 + \sqrt{2} \left(\frac{v_L}{v_T} \right)^2 \right]^2 \right\} \right) \quad \text{.....(3A.14)}$$

where υ is the Poisson's ration, b_S and b_E are magnitudes of Burgers vectors for dislocations in GaN which are equal to $b_S = c$ and $b_E = \left(a\sqrt{2}\right)/3$. N_D^S, N_D^E and N_D^M are the densities of the screw, edge and mixed dislocations, respectively and $1/\tau_D = 1/\tau_S + 1/\tau_E + 1/\tau_M$.

4.1 Introduction

A heterojunction is formed by interfacing two dissimilar semiconductor materials having different band gap energies. The perfect lattice matching is needed at the interface in order to eliminate surface defects, discontinuities and charge traps. The two semiconductors with different physical properties have their different Fermi levels are at different positions with respect to the vacuum level. When they are brought into contact, the Fermi levels align themselves throughout the composite materials. Due to which electrons from doped, wider band gap material transferred themselves across the barrier to the undoped and lower band gap material. In the process, electrons get accumulated near the interface in the lower band gap material creating an excess of space charges. The electron distribution in the space charges causes bending of the energy band towards the Fermi level. Charge neutrality is however maintained over the bulk, away from the interface. In the wider band gap side, the atoms are ionized over a certain region near the interface due to electrons getting transferred. Depletion charge density appears that causes band bending in the depletion region too. If the band bending is sufficiently large in the space-charge layer then charge inversion takes place. A well almost triangular in shape is formed. Perpendicular to the interface, quantum size effects become evident when the size of this well is comparable to electron deBroglie wavelength. Thus, in a heterojunction the electrons are tapped in an almost triangular potential well. Hence, these electrons are restricted to move only in specified direction/ plane. The framework for the treatment of the two dimensional electron transport in a triangular well was originally developed for Silicon inversion layers [Stern and Howard, 1967; Fang and Howard, 1966; Ando, Fowler and Stern, 1982].

4.1 (a) Two-dimensional electron gas (2D EG)

An important feature of an electron gas confined in a two-dimensional (2D) potential well is the quantization of the electron energy in the potential well leading to a splitting of the three-dimensional (3D) conduction band into 2D subbands [Walukiewicz, 1984]. In such a 2D potential well, the energy levels of the electrons are quantized in one direction and are continuous in other two directions. Hence, it is also called quasi-two dimensional (Q2D) system or 2D electron-gas (2D EG). Often, only the lowest level is occupied. All electrons then occupy the same state of motion in the *z*-direction but remain free in the *x*-*y* plane. Such 2D EG mobility is increased both by the reduced

scattering due to the separation of the ions or carriers from the parent donors and also due to the confinement to the lower dimension, i.e. two dimension (2D).

4.1 (b) One-dimensional electron gas (1D EG)

In such Q2D semiconductor structures, electrons are confined to move on the surface perpendicular to the depth of the quantum well as x-y plane. When the quantization is further done in one more direction of Q2D system i.e. along y-direction, the electrons will be able to move only in one direction, the x-direction. Such a system is called quasi-one-dimensional (Q1D) structure or 1D EG system. In Q1D system, electrons are confined to move only along the longitudinal direction, i.e. along the x- direction only [Arora and Prasad, 1983; Sakaki, 1980]. The motion, and thereby, the energy of electrons are quantized in transverse direction.

The concept of separating electrons from their parent donors in semiconducting systems was originally proposed by Esaki and Tsu [Esaki and Tsu, 1969]. Lowering of the dimensionality of semiconductor systems is another interesting part of a research work because it helps to develop new electronic devices as well as to explore the physics related to them. The possibility of having enhanced mobility due to less scattering because of separating the electrons in the quantum well from the wider band gap parent donor material and confining the system to 1D motion has encouraged researches to fabricate ultathin quantum semiconductor wires or quantum well wires (QWW), originally proposed by Sakaki [Sakaki, 1980]. These low dimensional semiconductor structures are quite interesting for their wide range of applications in optical and electronic devices not only due to its highly increased in the mobility, but also will be useful in further fast devices for communication and amplification. Hence, such systems show entirely different behavior from the bulk systems. Practically, it became possible due to latest technological achievements, such as Molecular beam epitaxy (MBE) technology.

In the chapter the low field transport subjected to ac and dc fields have been investigated in two different systems of heterojunctions formed by **GaAs/$Al_xGa_{(1-x)}As$** and **$Ga_xIn_{(1-x)}As$/InP**. The effect of lower temperature scattering mechanisms such as acoustic phonon via potential deformation (ac), piezoelectric (pz), ionized impurity (in) including both back ground and remote impurity scatterings, surface roughness (sr) and alloy disorder (all)

(only in the case of 2D EG GaInAs well) on the frequency dependent mobility is observed. The ac/dc mobilities for both types of heterojunctions are also calculated and observed. The temperature dependent dc mobility for 2D EG and 1D EG systems for heterojunctions of GaAs and GaInAs have been calculated and compared. This comparison helps to understand the dimensionality dependences of transport coefficient.

4.2 Theoretical Formulation

The electron wave functions describing the 2D EG and 1D EG, the subband energies and the subband population are solved by numerical self-consistent method. First, such calculation has been performed by Howard and is further extended by Maeda and Stern [Stern, 1967; Stern, 1972]. In our present studies, the electrons are confined into a triangular potential well, formed by heterojunction. In the model the potential well is along the z-axis, hence, the electrons can move freely along x, y plane forming **2D EG**. In the same model when a square quantum well of infinite height is present along the y-direction then electrons can move freely along x-direction only, gives **1D EG**. Many low dimensional electronic devices are based on such model as FET, MOS etc.

4.2 (a) For 2D EG

In the triangular potential well approximation, the potential energy is given by an infinite barrier for $z\langle 0$ and for $z\rangle 0$ which gives the potential energy to is $V(z) = eFz$. Hence, solution of the Schödinger equation is given by Airy function [Abramowitz and Stegun, 1964] which gives the wavefunction of the quantized energy states as,

$$\xi_i(z) = A_i\left[\left(\frac{2m^* eF_s}{\hbar^2}\right)^{1/3}\left\{z - \left(\frac{E_i}{eF_s}\right)\right\}\right] \qquad \ldots(4.1)$$

with the corresponding energy eigen value (E_i) trapped within the two-dimensional triangular potential well,

$$\text{or, } E_i \approx \left(\frac{\hbar^2}{2m^*}\right)^{1/3}\left[\frac{3}{2}\pi eF_s\left(i + \frac{3}{4}\right)\right]^{2/3} \qquad \ldots(4.2)$$

where m^*, e and $\hbar$ are effective mass, electronic charge and Plank's constant divided by 2π. F_s is the effective field. The exact eigenvalues $i+\left(3/4\right)$ is replaced by 0.7587, 1.7540 and 2.7575 respectively for the three lowest solutions [Ando, Fowler and Stern, 1982].

We generalize the model first put forward by Sakaki [Sakaki, 1980], that the carries occupy only their lowest size quantized subband and therefore behave essentially as a 2D EG. Such electron gas formed in a narrow channel of FET or HEMT occupying the lowest electron subband and has the following wave functions [Sarma and Lai, 1985],

$$\psi\ (x,\ y,\ z\ ) = \sqrt{\frac{b^{\ 3}}{2}} \times\ z\ \exp\ \left(-\ bz/2\right)\exp\ ^{\ i\left(k_{\ x}\ x\ +\ k_{\ y}\ y\ \right)} \quad \ldots(4.3)$$

where k_x and k_y be the electron wave vector along the x and y-directions respectively. b, the variation parameter [Ando, Fowler and Stern, 1982] is given as,

$$b = \left\{\frac{12e^2m^*}{\varepsilon_o\varepsilon_s\hbar^2}\left[\frac{11}{32}N_0\right]\right\}^{1/3} \quad \ldots(4.4)$$

The trial Eigen function and the energy eigen values for the ground state as given by Fang and Howard [Fang and Howard, 1966] is,

$$\xi_o(z) = \left(\frac{1}{2}b^3\right)^{1/2} z\exp(-\frac{bz}{2}) \quad \ldots(4.5)$$

The equation (4.5) is obtained by minimizing the total energy of the system with respect to b, i.e., $dE_o/dt = 0$. The energy for the lowest state is given by,

$$E_o = \frac{\hbar^2b^2}{8m*} + \left(\frac{3e^2}{4\pi\varepsilon_o\varepsilon_s b}\right)\left[N_{dep} + \frac{11}{16}N_{inv} - \frac{2}{B}\left(N_A - N_B\right)\right] \quad \ldots(4.6)$$

The potential vanishes at the interface. N_A is the acceptor concentration. The charge density associated with the variational wave-function penetrates over an average distance of $z_o = 3/b$.

The density of state (DOS) is an important parameter while calculating various transport parameters of low dimensional systems. The DOS in n-dimensional wave vector space is $(2\pi)^{-n}$ [Ando, Folwer and Stern, 1982], the two-dimension DOS per unit area per unit energy for compound semiconductor is,

$$D(E) = \frac{1}{(2\pi)^2} 2\pi k \frac{dk}{dE} \qquad \ldots(4.7)$$

For the electron energy is given as, $E = E_i + \hbar^2 k^2 / 2m^*$ the DOS is modified as,

$$D(E) = \frac{m^*}{(2\pi)^2} 2\pi \frac{2m^*}{\hbar^2} \sqrt{E - E_i} \frac{1}{\hbar^2 k}$$

$$\therefore D(E) = \frac{m^*}{(2\pi)} \frac{1}{\hbar^2} \sum H(E - E_i) \qquad \ldots(4.8)$$

where H is the step function defined as $H(z) = 1 \quad z \rangle 0$, and $H(z) = 0 \quad z \langle 0$

The probability of occupancy of the subband is,

$$n(z) = \sum_i N_i |\xi_i|^2$$

Where, $N_i = \int D(E) f(E) dE$

$$N_i = \frac{m^* k_B T}{2\pi\hbar^2} \ln\left[1 + \exp\left(\frac{E_F - E_i}{k_B T}\right)\right] \qquad \ldots(4.9)$$

Where $f(E)$ is the Fermi- Dirac (F-D) carrier distribution.

In our model, we assumed that the carriers are scatted by various phonon and nonphonon scattering mechanisms. The most important nonphonon scattering mechanisms at low temperatures are ionized impurity (in), alloy disorder (all) and surface roughness (sr) scattering mechanisms are included in our calculation, simultaneously the phonon scattering mechanisms such as piezoelectric via deformation potential (pz) and acoustic phonon (ac) scattering mechanisms are also taken into account.

For the phonon scattering mechanisms the matrix element for the transition from k to k' due to electron-phonon interactions [Nag, 1980] is given as,

$$M(k,k') = \int \psi^*(x,y,z)\left(ae^{\overline{iQR}} - a^+ e^{\overline{-iQR}}\right)\times\psi(x,y,z)dxdydz \qquad ...(4.10)$$

Where a and a^+ are the annihilation and creation operators. $\overline{Q}$ and $\overline{R}$ the wave vector and displacement vector in three dimensions. The integration is over space for both phonons and electrons. The matrix element takes the form,

$$M(k,k') = \left(N_Q + \frac{1}{2} \pm \frac{1}{2}\right)^{1/2}\left(C/Q\right)\partial(k-k'\pm q_x)\partial(k-k'\pm q_y)\times\left(\frac{b^3}{z}\right)\times\int z^2 e^{-bz\pm iq_z z}dz$$

...(4.11)

Where C, the constant has different expressions for different scattering processes. q_{xyz} is the components of phonon wave vector along the x, y and z direction respectively. N_Q is the phonon number, obeys Bose-Einstein statistics. The momentum conservation approximation (MCA) proposed by Ridley [Ridley, 1982] has been used to perform the integration over the y axis.

For the nonphonon scattering mechanisms such as coulomb scatterings, impurity and surface roughness scattering, the expression for the matrix element is given as,

$$M(k,k') = \int \psi(x,y,z)V(Q)\psi^*(x,y,z)dxdydz \qquad ...(4.12)$$

Where $V(Q)$ is the coulomb potential. The coulomb potential $V(Q)$ for the different scattering mechanisms [Fishman, 1986] are substituted in the expression for the relaxation time defined as,

Relaxation time for nonphonon scattering or elastic collision is given by [Nag, 1980]:

$$\tau^{-1} = \sum_{K'} P(k,k')\left[1 - \frac{\cos\theta'}{\cos\theta}\right] \qquad ...(4.13)$$

for nonrandomizing elastic collision or

$$\tau^{-1} = \sum_{K'} P(k,k')\left[\frac{1-f_o(E')}{1-f_o(E)}\right] \qquad ...(4.14)$$

for randomizing inelastic collision.

Where $P(k,k')$ is the transition probability of electron is,

$$P(k,k') = \left(\frac{2\pi}{\hbar}\right)\left|M(k,k')\right|^2 \partial\left(E_k - E_{k'}\right) \qquad \ldots(4.15)$$

For elastic scattering $E_k = E_{k'}$ also $f_o(E) = f_o(E')$
from k to k' and θ is the scattering angle between them.

Our mobility calculation is based on the Boltzmann transport equation and the relaxation time is calculated by using Fermi's golden rule. At low temperatures, the dominant scattering processes are the piezoelectric via deformation potential (pz) and acoustic phonon (ac) scattering as phonon scattering mechanisms; and ionized impurity (in) scattering due to both remote and background impurities, alloy disorder (all) and surface roughness (sr) scatterings as nonphonon scattering mechanisms. Hence, the total low temperature scattering mechanisms is obtained by using Matthiessen's rule, which is symbolically expressed as $\tau(E)$ and is a function of energy E. The corresponding values of the relaxation scattering mechanism are given in **Appendix 4A** for Q2D system.

Average relaxation time for 2D EG, $\langle\tau\rangle$ [Nag, 1980] is given as,

$$\langle\tau\rangle = \frac{\int E\ \tau(E)\ \frac{\partial f_o}{\partial E}\, dE}{\int E\ \frac{\partial f_o}{E\,\partial E}\, dE} \qquad \ldots(4.16)$$

The mobility for Q2D system can be obtained using the above averaging relation.

4.2 (b) For 1D EG

In the case of FET, an approximately triangular potential well which is formed along the z-axis and a square quantum well of infinite height is present along the y-direction. Hence, the wave function relation for such electron gas occupying the lowest electron subband has the following wave functions [Sarma and Lai, 1985],

$$\psi(x, y, z) = \sqrt{\frac{b^3}{La}} \sin\left(\frac{\pi y}{a}\right) z \quad \exp\left(-bz/2\right) \exp^{ik_z x} \quad \ldots(4.17)$$

where L and a are the length and width of the channel respectively, used in Stern-Howard wave function [Stern and Howard, 1967]. k_x is the electron wave vector along the x-direction and b, the variation parameter [Ando, Fowler and Stern,1982] is already defined as above.

The DOS per unit length per unit energy for compound semiconductor is,

$$D(E) = \frac{1}{(2\pi)} \frac{dk}{dE}$$

We get, for 1D EG carrier calculation,

$$N_i = \frac{m^*}{\sqrt{2k_B T}\pi\hbar} \int \frac{\left(E/k_B T\right)^{-1/2}}{\left(1 + e\left(\frac{E_i - E_F}{k_B T}\right)\right)} \partial\left(\frac{E}{k_B T}\right) \quad \ldots(4.18)$$

Where E_F is the Fermi energy.

The matrix element of equation (4.11) also gets modified for 1D EG [Kundu et al., 1990] as,

$$M(k,k') = \left(N_Q + \frac{1}{2} \pm \frac{1}{2}\right)^{1/2} \left(C/Q\right) \partial\left(k - k' \pm q_x\right) \left(2/a\right)$$
$$\times \int \sin^2\left(\pi y/a\right) e^{\pm i q_y y} dy \left(\frac{b^3}{z}\right) \times \int z e^{-bz \pm i q_z z} dz$$

$\ldots(4.19)$

Relaxation time for nonphonon scattering or elastic collision is given by equation (4.13) and is calculated with scattering angle of π for 1D EG. So, that the term in equation (4.13) is replaced by 2.

At low temperatures, the dominant scattering processes are the piezoelectric via deformation potential (pz) and acoustic phonon (ac) scattering as phonon scattering mechanisms; and ionized impurity (in) scattering due to both remote and background impurities and surface roughness (sr) scatterings as nonphonon scattering mechanisms. The expressions for individual relaxation scattering mechanisms are given in **Appendix 4B** for Q1D system. In the

case of 1D EG also, the total of all such scattering mechanisms is obtained by Matthiessen's rule.

Average relaxation time for 1D EG [Nag, 1980] is given by,

$$\langle \tau \rangle = \frac{\int E^{1/2} \tau (E) \frac{\partial f_o}{\partial E} dE}{\int E^{1/2} \frac{\partial f_o}{\partial E} dE} \qquad \text{....(4.20)}$$

$f_0(E)$ in the equations (4.16) and (4.20) is the F-D distribution function of the electrons. $\langle \tau \rangle$ in equations (4.16) and (4.20) is calculated by taking density of states for 2D EG and 1D EG respectively. We generalize the model first put forward by Sakaki [Sakaki, 1980], that the carries occupy only their lowest size quantized subband and that the carries therefore behave essentially as a 2D EG and 1D EG

4. 2 (c) dc/ac Mobility for 2D EG and 1D EG systems:

The dc mobility relation based on the Boltzmann's transport relation for both **2D EG** and **1D EG** systems are given [Nag, 1980] as,

$$\mu = \frac{e}{m^*} \langle \tau \rangle \qquad \text{...(4.21)}$$

The averaging over the distribution function, <> is taken for 2D EG and 1D EG by equations (4.16) and (4.20) respectively.

In the presence of a weak ac field with frequency ω, the scattering time or relaxation time becomes complex, i.e ω^{-1} changes to $(\tau + i\omega)^{-1}$ leading to the real and the imaginary parts of the mobility μ_r and μ_{im} respectively. These are given as [Nag, 1980]:

$$\mu_r = \left(\frac{e}{m^*} \right) \left\langle \frac{\tau}{(1 + \omega^2 \tau^2)} \right\rangle \qquad \text{...(4.22)}$$

$$\mu_{im} = \left(\frac{e}{m^*} \right) \omega \left\langle \frac{\tau^2}{(1 + \omega^2 \tau^2)} \right\rangle \qquad \text{...(4.23)}$$

ω is the angular frequency, τ is the contribution from lower temperature scattering mechanisms as described above, is taken for Q2D and Q1D

separately with their appropriate scattering mechanisms and related constant.

4.3 Results and Discussions

Comparative studies of reduced dimensionality on low field electron transport at the heterojunctions of GaAs/$Al_xGa_{(1-x)}As$ and $Ga_{(1-x)}In_xAs$/InP systems at low temperatures has been carried out. The material parameters are taken from Walukiewicz et al., Kundu et al. and Ando et al. [Walukiewicz and Ruda, 1984; Kundu, Sarkar and Basu, 1988; Ando, Fowler and Stern, 1982] and are also given in the table Parameter of GaAs-InGaAs. The carrier concentration for 2D EG and 1D EG are taken to be $10^{14}m^{-2}$ and $10^{7}m^{-1}$ respectively. The concentration of background and remote ionized impurities are taken as $10^{20}m^{-3}$ and $10^{22}m^{-3}$ respectively for both systems. The value of x for GaAs and InGaAs are taken to be 0.33 and 0.47 respectively. The various scattering mechanisms for Q2D and Q1D are taken from Walukiewicz et al., Ando et. al. and Ando [Walukiewicz et al., 1984; Ando, Fowler and Stern, 1982; Ando, 1977] and Kundu et. al. [Kundu, Sarkar and Basu, 1990; Kundu, Sarkar and Basu, 1988] respectively. The expressions for these scattering mechanisms are also given in **Appendix 4A & 4B**. The corresponding Fermi energy level relation for 2D EG and 1D EG are also given in the **Appendix 4C**.

The theoretical variation of 2D EG dc mobility versus temperature for GaAs for various scattering mechanisms, such as acoustic phonon via deformation potential (ac), piezoelectric (pz), ionized impurity (in), and surface roughness (sr) scattering mechanisms independently is given in Fig. 4.1. The Fig 4.1 shows that the surface roughness (sr) scattering mechanism dominates the other scattering mechanisms at low temperatures. At higher temperatures other scattering mechanisms is also more active.

Similarly, the 1D EG dc mobility versus temperature for GaAs for various scattering mechanisms, such as acoustic phonon via deformation potential (ac), piezoelectric (pz), ionized impurity (in) and surface roughness (sr) scattering mechanisms separately is presented in Fig. 4.2. Fig 4.2 shows that the phonon scattering mechanisms dominates the other scattering mechanisms in all temperature ranges.

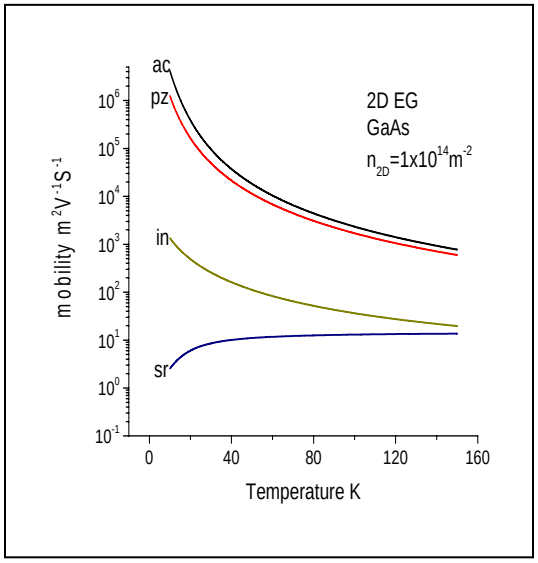

Fig. 4.1 Variation of 2D EG dc mobility versus temperature for GaAs for various scattering mechanisms such as acoustic phonon via deformation potential (ac), piezoelectric (pz), ionized impurity (in), alloy disorder (all) and surface roughness (sr) scattering mechanisms.

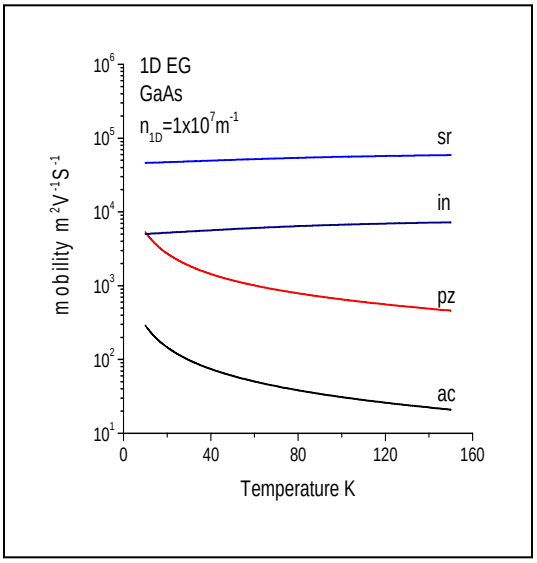

Fig. 4.2 Variation of 1D EG dc mobility versus temperature for GaAs for various scattering mechanisms such as acoustic phonon via deformation potential (ac), piezoelectric (pz), ionized impurity (in) and surface roughness (sr) scattering mechanisms.

The resultant mobility due to individual scattering mechanisms operative in 2D EG and 1D EG respectively are calculated and are given in Fig. 4.3 and Fig. 4.4 respectively.

The variation of dc mobility versus temperature for GaAs and InGaAs is given in Fig. 4.3 with the various scattering mechanisms such as acoustic phonon via deformation potential (ac), piezoelectric (pz), ionized impurity (in) and surface roughness (sr) scattering mechanisms. InGaAs is an alloy semiconductor hence, alloy disorder (all) scattering mechanism is also included for InGaAs. It is seen in Fig. 4.3 that the mobility at first increases with temperature, reaches a maximum and then decreases. It is due to the surface roughness scattering mechanism dominating the other scattering mechanisms in the 2D EG as already mentioned above also, but at higher temperatures the contributions of phonon scattering mechanisms such as, acoustic phonon (ac) and piezoelectric (pz) are also effective. Hence, the over all effect causes the mobility to decrease further at higher temperatures.

Similar to Fig. 4.3, Fig. 4.4 also shows the variation of dc mobility versus temperature for 1D EG GaAs and InGaAs with the various scattering

mechanisms, such as acoustic phonon via deformation potential (ac), piezoelectric (pz), ionized impurity (in) and surface roughness (sr) scattering mechanisms. Here, the mobility decreases as the temperature increases. It is due to the phonon scatterings dominating the other scattering mechanisms. At higher temperatures, the contribution of phonon scattering mechanism is more prominent as compared to other scattering mechanisms due to which the mobility decreases further.

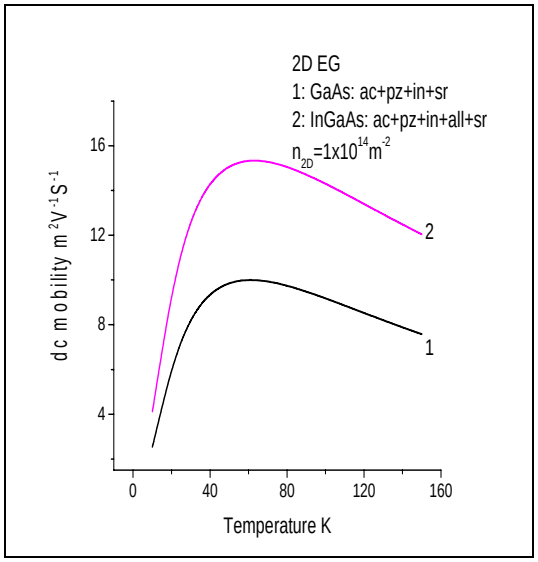

Fig. 4.3 Variation of 2D EG dc mobility versus temperature for GaAs (1) and InGaAs (2) with various scattering mechanisms such as acoustic phonon via deformation potential (ac), piezoelectric (pz), ionized impurity (in) and surface roughness (sr) scattering mechanisms.

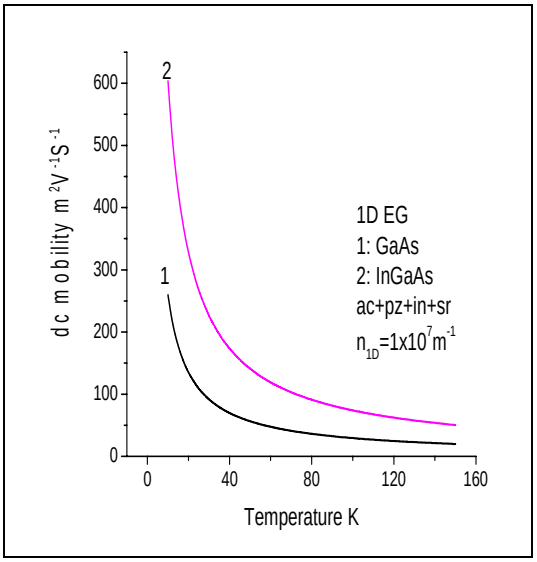

Fig. 4.4 Variation of 1D EG dc mobility versus temperature for GaAs (1) and InGaAs (2) with various scattering mechanisms such as acoustic phonon via deformation potential (ac), piezoelectric (pz), ionized impurity (in) and surface roughness (sr) scattering mechanisms.

The variation in the nature of curves for 2D EG/1D EG dc mobility is shown in Figs. 4.3 and 4.4 respectively, that can be explained due to the effect of dominating nature of the respective scattering mechanisms in both cases. As already mentioned that the ionized impurity scattering is minimized in heterojunction for both 2D EG and 1D EG systems. However, due to the presence of interface, the surface roughness scattering becomes more important than the other scattering mechanisms in 2D EG. In contrast, in 1D EG, the contribution of phonon scattering mechanisms dominates over all other scattering mechanisms. However, in both 2D EG and 1D EG more

scattering mechanisms become more active as the temperature increases, it causes the resultant mobility to decrease with temperature.

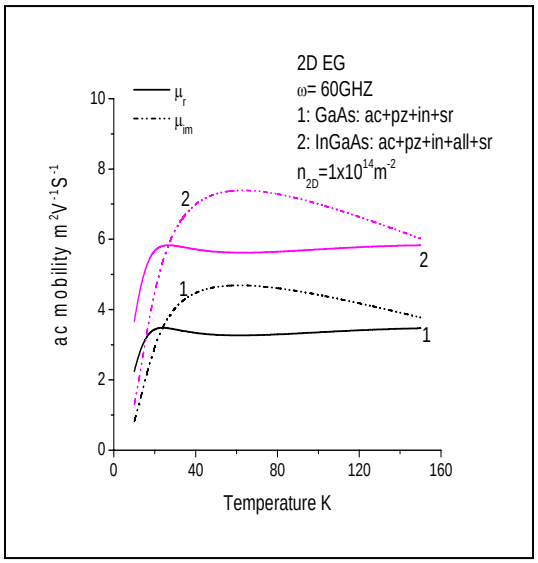

Fig. 4.5 Variation of 2D EG ac mobility versus temperature at constant frequency 60GHz for GaAs (1) and InGaAs (2) with various scattering mechanisms such as acoustic phonon via deformation potential (ac), piezoelectric (pz), ionized impurity (in), alloy disorder (all) and surface roughness (sr) scattering mechanisms.

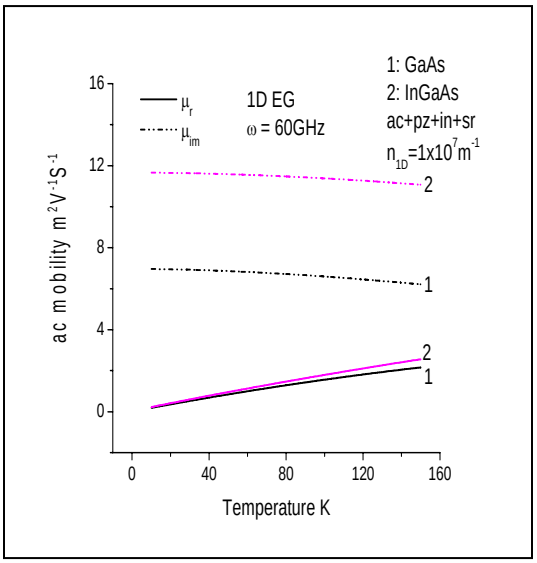

Fig. 4.6 Variation of 1D EG ac mobility versus temperature at constant frequency 60GHz for GaAs (1) and InGaAs (2) with various scattering mechanisms such as acoustic phonon via deformation potential (ac), piezoelectric (pz), ionized impurity (in) and surface roughness (sr) scattering mechanisms.

Most of the present electronic devices are subjected to ac power. The studies of ac transport properties in such devices are also interesting. The author also presented the variation of 2D EG ac mobility versus temperature at a constant frequency 60GHz for GaAs and InGaAs, in Fig. 4.5 with the various scattering mechanisms such as acoustic phonon via deformation potential (ac), piezoelectric (pz), ionized impurity (in), alloy disorder (all) (only for InGaAs triangular well) and surface roughness (sr) scattering mechanisms.

The imaginary part of 2D EG ac mobility given in Fig. 4.5 is similar to that of the 2D EG dc mobility as given in Fig.4.3, but the magnitude of the imaginary part of ac mobility is about half as that of the dc mobility. It is expected due to the presence of frequency (ω) in the ac mobility relations, which are given by equation (4.22) and (4.23). When ω is taken as zero, the real part of the

ac mobility determines the dc mobility term. It is true in low frequency region. In contrast, in high frequency region, $\left(1/\tau\omega^2\right)$ term determines the real part of the ac mobility. Hence the nature of the imaginary part of ac mobility is found to be similar to that of the dc mobility curve. Also due to the value of ω being large, the magnitude of the imaginary part of ac mobility is higher than that of real part of the ac mobility and can be seen in Fig. 4.5.

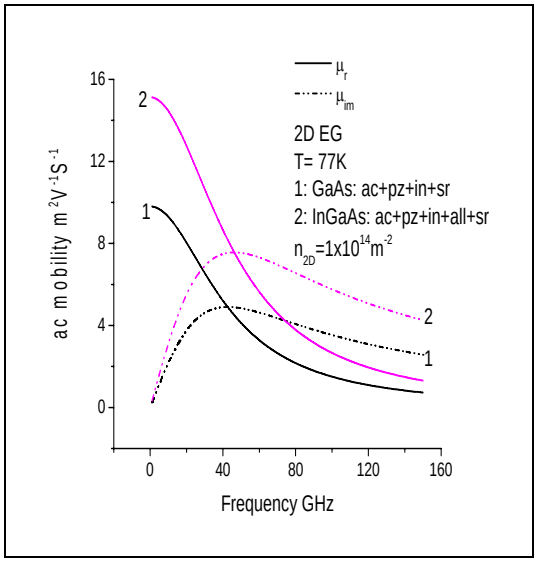

Fig. 4.7 Variation of 2D EG ac mobility versus frequency at constant temperature 77K for GaAs (1) and InGaAs (2) with various scattering mechanisms such as acoustic phonon via deformation potential (ac), piezoelectric (pz), ionized impurity (in), alloy disorder (all) and surface roughness (sr) scattering mechanisms.

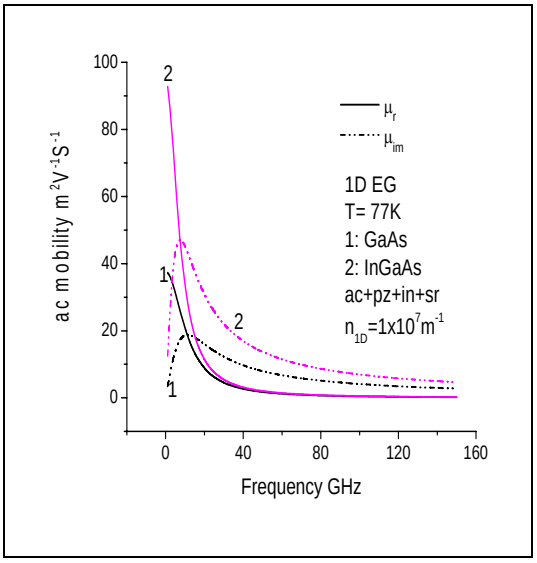

Fig. 4.8 Variation of 1D EG ac mobility versus frequency at constant temperature 77K for GaAs (1) and InGaAs (2) with various scattering mechanisms such as acoustic phonon via deformation potential (ac), piezoelectric (pz), ionized impurity (in) and surface roughness (sr) scattering mechanisms.

The same logic causes the variation in the magnitude of 1D EG ac imaginary part of the mobility to be much higher than that of ac real part which is given in Fig. 4.6. The Fig. 4.6 shows the variation of 1D EG ac mobility versus temperature at a constant frequency 60GHz for GaAs and InGaAs with the various scattering mechanisms, such as acoustic phonon via deformation potential (ac), piezoelectric (pz), ionized impurity (in) and surface roughness (sr) scattering mechanisms.

The frequency dependent ac real and imaginary parts of ac mobility study is also carried out and shown in Fig. 4.7. Fig. 4.7 shows the variation of 2D EG ac mobility versus frequency at a constant temperature 77K for GaAs and InGaAs with the various scattering mechanisms such as acoustic phonon via deformation potential (ac), piezoelectric (pz), ionized impurity (in), alloy disorder (all) (only for InGaAs) and surface roughness (sr) scattering mechanisms.

The Fig. 4.8 shows the similar variation of 1D EG ac mobility versus frequency at a constant temperature 77K for GaAs and InGaAs with the various scattering mechanisms such as acoustic phonon via deformation potential (ac), piezoelectric (pz), ionized impurity (in) and surface roughness (sr) scattering mechanisms.

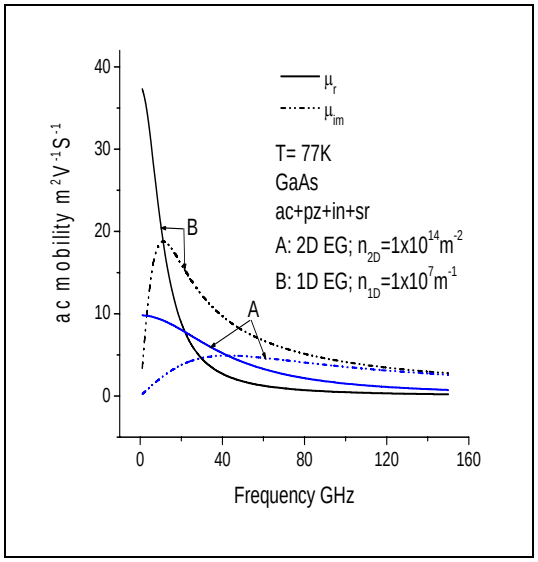

Fig. 4.9 Variation of 2D EG (A)/ 1D EG (B) ac mobility versus frequency at constant temperature 77K for GaAs with various scattering mechanisms such as acoustic phonon via deformation potential (ac), piezoelectric (pz), ionized impurity (in) and surface roughness (sr) scattering mechanisms.

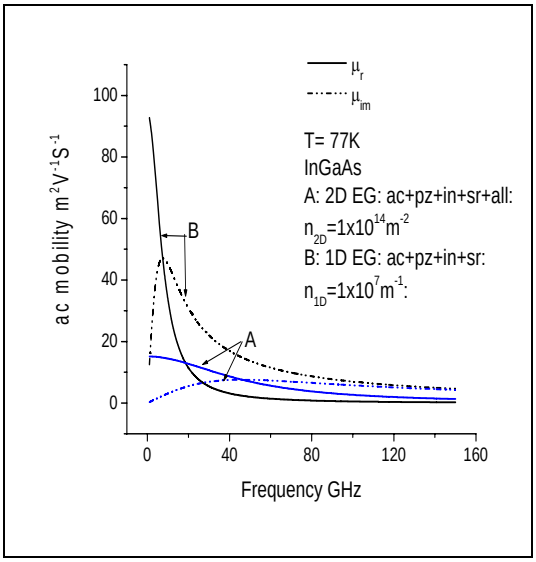

Fig. 4.10 Variation of 2D EG (A)/ 1D EG (B) ac mobility versus frequency at constant temperature 77K for InGaAs with various scattering mechanisms such as acoustic phonon via deformation potential (ac), piezoelectric (pz), ionized impurity (in) and surface roughness (sr) scattering mechanisms. Alloy disorder scattering (all) mechanism is also included in case of 2D EG.

Comparative studies of Figs. 4.7 and 4.8, show that the real parts of the ac mobility decreases sharply with frequency, while the imaginary part first increases and then decreases in both cases. The real and imaginary parts of the ac mobility at low frequencies are determined by $\langle \tau \rangle$ and $\langle \omega\tau^2 \rangle$, while for higher frequency region these vary as $\langle 1/\omega^2 \tau \rangle$ and $\langle 1/\omega \rangle$ respectively. It is also observed from Fig. 4.8 that the effect of dimensionality disappears in the real part of ac mobility for Q1D at high frequencies, while the imaginary parts of mobility show the effect of dimensionality throughout the frequency range studied here. The effect of dimensionality appears more distinct in 2D EG ac mobility as can be see in Fig. 4.7.

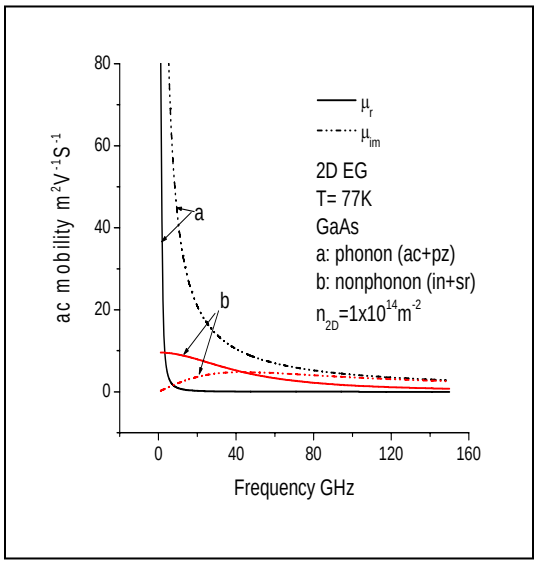

Fig. 4.11 Variation of 2D EG ac mobility versus frequency at constant temperature 77K for GaAs with phonon (a) scattering mechanisms such as acoustic phonon via deformation potential (ac) and piezoelectric (pz) scattering mechanisms; and nonphonon (b) scattering mechanisms such as ionized impurity (in), alloy disorder (all) and surface roughness (sr) scattering mechanisms.

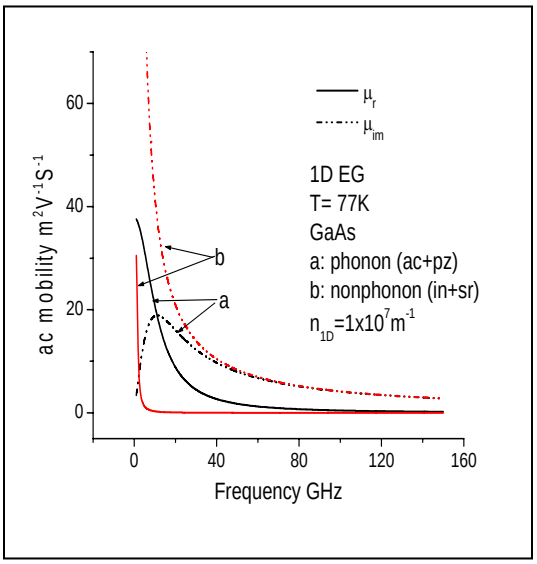

Fig. 4.12 Variation of 1D EG ac mobility versus frequency at constant temperature 77K for GaAs with phonon (a) scattering mechanisms such as acoustic phonon via deformation potential (ac) and piezoelectric (pz) scattering mechanisms; and nonphonon (b) scattering mechanisms such as ionized impurity (in) and surface roughness (sr) scattering mechanisms.

Over all, the Figs. 4.3 to 4.8 show the similarity in one aspect that the magnitude of dc as well as ac mobility for InGaAs is found to be higher as compared to that of GaAs and is expected due to the effect of effective mass of InGaAs being lower than that of GaAs.

Variation of 2D EG and 1D EG ac mobility versus frequency at a constant temperature 77K for GaAs with various scattering mechanisms such as acoustic phonon via deformation potential (ac), piezoelectric (pz), ionized impurity (in) and surface roughness (sr) scattering mechanisms is shown in Fig. 4.9.

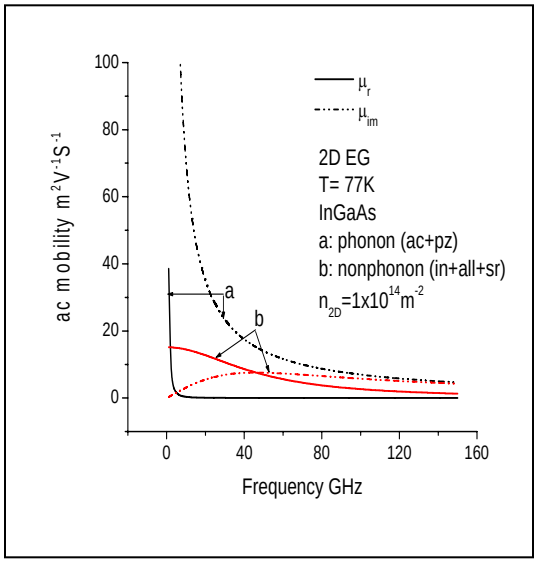

Fig. 4.13 Variation of 2D EG ac mobility versus frequency at constant temperature 77K for InGaAs with phonon (a) scattering mechanisms such as acoustic phonon via deformation potential (ac) and piezoelectric (pz) scattering mechanisms; and nonphonon (b) scattering mechanisms such as ionized impurity (in), alloy disorder (all) and surface roughness (sr) scattering mechanisms.

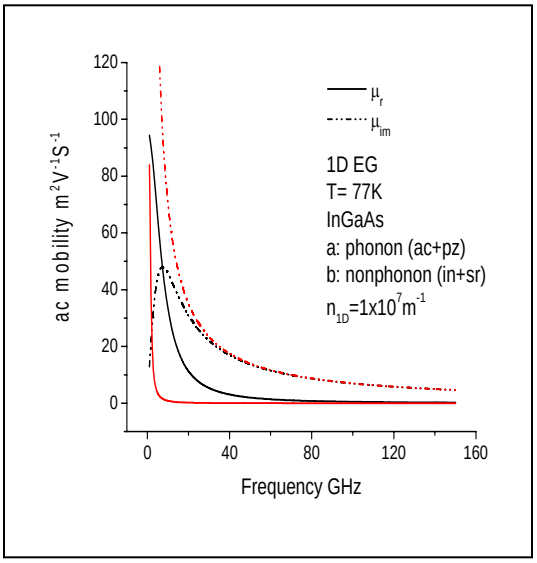

Fig. 4.14 Variation of 1D EG ac mobility versus frequency at constant temperature 77K for InGaAs with phonon (a) scattering mechanisms such as acoustic phonon via deformation potential (ac) and piezoelectric (pz) scattering mechanisms; and nonphonon (b) scattering mechanisms such as ionized impurity (in) and surface roughness (sr) scattering mechanisms.

Similar variation of 2D EG and 1D EG ac mobility versus frequency at a constant temperature 77K for InGaAs with the various scattering mechanisms, such as acoustic phonon via deformation potential (ac),

piezoelectric (pz), ionized impurity (in) and surface roughness (sr) scattering mechanisms is given in Fig. 4.10. Alloy disorder scattering (all) mechanism is also included in the case of 2D EG for InGaAs.

Both the Figs. 4.9 and 4.10 show the magnitude of real and imaginary parts of ac mobilities for Q1D is higher than the corresponding parts of the ac mobility in Q2D. It also verifies that the reduction of dimensionality reduces the scattering mechanisms, hence leads to the higher values of mobility in the case of 1D EG.

The 2D EG ac mobility variation with frequency is shown in Fig. 4.11 at a constant temperature of 77K for GaAs with phonon scattering mechanisms such as acoustic phonon via deformation potential (ac) and piezoelectric (pz); and nonphonon scattering mechanisms such as ionized impurity (in) and surface roughness (sr) scattering mechanisms separately.

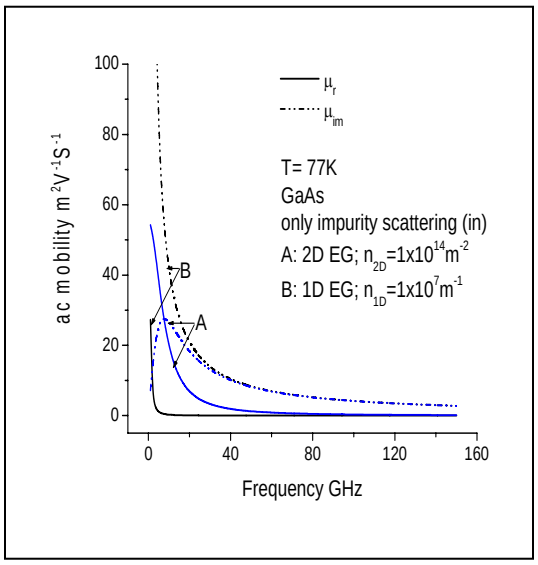

Fig. 4.15 Variation of 2D EG (A)/ 1D EG (B) ac mobility versus frequency at constant temperature 77K for GaAs for only impurity (in) scattering mechanism, including back ground and remote impurity.

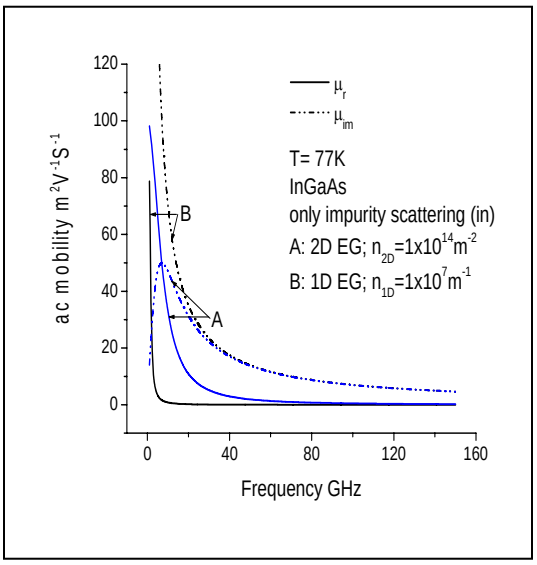

Fig. 4.16 Variation of 2D EG (A)/ 1D EG (B) ac mobility versus frequency at constant temperature 77K for InGaAs for only impurity (in) scattering mechanism, including back ground and remote impurity.

Similarly, Fig. 4.12 shows the variation of 1D EG ac mobility versus frequency at a constant temperature 77K for GaAs with both phonon and nonphonon scattering mechanisms which are taken for curve of Fig. 4.11.

For InGaAs, the 2D EG ac mobility variation with frequency is shown in Fig. 4.13 at a constant temperature of 77K with phonon scattering mechanisms such as acoustic phonon via deformation potential (ac) and piezoelectric (pz); and nonphonon scattering mechanisms, such as ionized impurity (in), alloy disorder scattering (all) and surface roughness (sr) scattering mechanisms separately.

Similar to Fig. 4.13, Fig. 4.14 shows variation of 1D EG ac mobility versus frequency at a constant temperature 77K for InGaAs with phonon scattering mechanisms such as acoustic phonon via deformation potential (ac) and piezoelectric (pz); and nonphonon scattering mechanisms such as ionized impurity (in) and surface roughness (sr) scattering mechanisms separately.

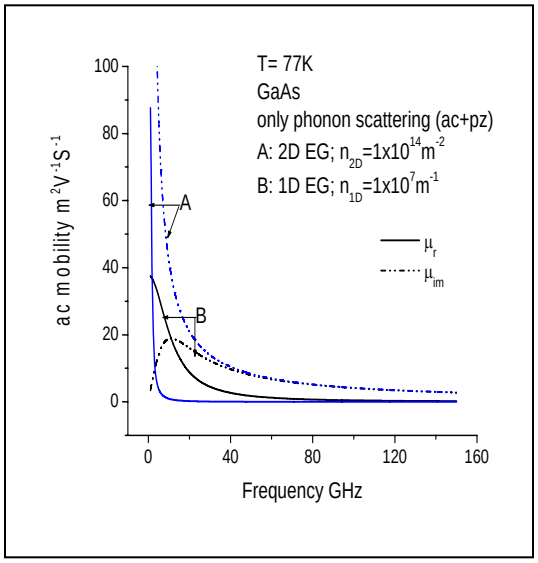

Fig. 4.17 Variation of 2D EG(A)/ 1D EG (B) ac mobility versus frequency at constant temperature 77K for GaAs with only phonon scattering mechanisms as acoustic phonon via deformation potential (ac) and piezoelectric (pz) scattering mechanisms.

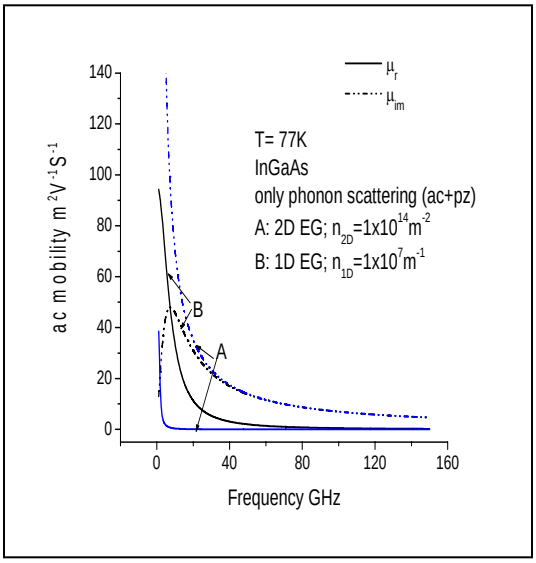

Fig. 4.18 Variation of 2D EG(A)/ 1D EG (B) ac mobility versus frequency at constant temperature 77K for InGaAs with only phonon scattering mechanisms as acoustic phonon via deformation potential (ac) and piezoelectric (pz) scattering mechanisms.

The variations of 2D EG and 1D EG ac mobility versus frequency at a constant temperature 77K for GaAs and InGaAs with ionized impurity (in)

scattering mechanism only, including both back ground and remote impurities are shown in Figs. 4.15 and 4.16 respectively

Whereas, Fig. 4.17 and 4.18 show variations of 2D EG and 1D EG ac mobility versus frequency at a constant temperature 77K with only phonon scattering mechanism as acoustic phonon via deformation potential (ac) and piezoelectric (pz) scattering mechanisms for GaAs and InGaAs respectively.

4.4 Conclusions

In our work we have selected the heterojunction of GaAs/AlGaAs and InGaAs/InP, due to their present available applications.

The variation of mobility due to the various scattering mechanisms applicable for both 2D EG and 1D EG systems with temperature are also independently investigated.

Comparative studies of dc and ac mobility variations with temperatures have been carried out for both 2D EG and 1D EG systems formed at the heterojuctions of GaAs and InGaAs. It is observed in both the heterojucations that 1D EG ac/dc mobility is much higher than that of 2D EG ac/dc mobility.

The variation of real and imaginary parts of ac 2D EG and 1D EG mobility with frequency is also compared for both the heterojunctions. It is found that the value of mobility for InGaAs heterojunction is more than that of GaAs heterojunction.

The effect of phonon and nonphonon scattering mechanisms on the ac 2D and 1D mobility of the heterojucntion systems are also observed and compared.

References

Abramowitz M. and Stegun I.A., eds. 1964 Handbook of Mathematical Functions (National Bureau of Standards Applied Mathematics Series, No. 55) (1964).
Ando T., J. Phys. Soc. Japan 43, 1616 (1977).
Ando T., Fowler A.B. and Stern F., Rev. Mod. Phys. 54, 437 (1982).
Arora V.K. and Prasad M., Phys. Stat. Sol. (b) 117, 127 (1983).
Esaki L. and Tsu R., IBM Research Laboratories, International Report No RC 2418, 1969 (unpublished).
Fang F.F. and Howard W.E., Phys. Rev. Lett. 16, 797 (1966).
Fishman G., Phys. Rev B 34, 2394 (1986).
Ghosh P.K., Sarkar C.K. and Chattopadhyay D., Phys. Stat. Sol. (a) 156, 365 (1996).
Nag B. R., Electron transport in Compound Semiconductors, edited by H.J. Queisser (Springer, Berlin) (1980).
Kundu S., Sarkar C.K. and Basu P.K., J. Appl. Phys. 61, 5080 (1987).
Kundu S., Sarkar C.K. and Basu P.K., J. Appl. Phys. 68, 1070 (1990).
Kundu S., Sarkar C.K. and Basu P.K., Phys. Rev. B 38, 5730 (1988).
Ridley B., J. Phys. C 15, 5899 (1982).
Sakaki H., Jpn. J. Appl. Phys. 19, L735 (1980).
Sarma Das S. and Loi W.Y., Phys. Rev. B 32, 1401 (1985).
Stern R. and Howard W.E., Phys. Rev. 163, 816 (1967).
Stern F., Phys. Rev. 159, 632 (1967).
Stern, Phys. Rev. B 5, 4891 (1972).
Walukiewicz W., Ruda H.E., Logowski J. and Gatos H., Phys. Rev. B 30, 4571 (1984).

Parameters of GaAs- GaInAs: Table 4.1

Quantity	Magnitude GaAs	GaInAs	Units	References
Static dielectric constant ε_s	12.9	13.77	$C^2N^{-1}m^{-2}$	Walukiewicz et al., 1984
Effective mass m^*	$0.067(9.109\times10^{-31})$	$0.049.109\times10^{-31})$	Kg	Walukiewicz et al., 1984
alloy composition z	0.33	0.47		Kundu et al., 1987
Elastic constant C_l	139.7	130.9	GNm^{-2} GNm-2	Kundu et al., 1988
Dimensionless piezoelectric constant K	0.064	0.034		Walukiewicz et al., 1984

mean specific heat H	0.43	nm	Kundu, 1988
d	1.5	nm	Kundu, 1988
Wide of the channel a	10	nm	Kundu, 1988
Background impurities N_B	$1x10^{20}$	m^{-3}	Kundu, 1988
Remote impurities N_R	$1x10^{22}$	m^{-3}	Kundu, 1988
Carrier concentration N_o	$1x10^{16}$	m^{-2}	Kundu, 1988
1D carrier concentration n_{1D}	$1x10^{7}$	m^{-1}	
2D carrier concentration n_{2D}	$1x10^{-14}$	m^{-2}	
Deformation Potential E_1	7	eV	Walukiewicz et al., 1984
Volume of a unit cell V	$5.05x10^{-29}$	m^3	
Alloy scattering potential ΔE	0.7	eV	
N_s	$1.92x10^{16}$	m^{-2}	Ando et al., 1982
N_{depl}	$1x10^{16}$	m^{-2}	
rms height of the rough surface Δ	0.43	nm	Ando et al., 1982
Correlation length L	1.5	nm	Ando et al., 1982

References for Parameters:

Ando T., Fowler A. B. and Stern F., Rev. Mod. Phys. 54, 437 (1982).
Kundu S., Sarkar C.K. and Basu P.K., Phys. Rev. B 38, 5730 (1988).
Kundu S., Sarkar C.K. and Basu P.K., J. Appl. Phys. 61, 5080 (1987).
Walukiewicz H., Ruda. H.E., Logowski J. and Gatos H., Phys. Rev. B 30, 4571 (1984).

Appendix 4A

2D EG

τ_{ac}, τ_{pz},τ_{im}, τ_{all} and τ_{sr} are the relaxation time for acoustic phonon via potential deformation, piezoelectric, ionized impurity, alloy disorder and surface roughness scattering [Walukiewicz, Ruda, Jogowski and Gatos, 1984; Ando, Fowler and Stern, 1982; Ando, 1977] respectively for **2D EG**.

$$\tau^{-1}_{ac} = \frac{3E_1^2 m^* K_B T b}{(8\pi\hbar^3 C_L)} \int_0^{\pi} \sin^4\alpha \left(\sin\alpha + \frac{q_s}{2C_2\sqrt{x}}\right)^{-2} d\alpha \quad ...(4A.1)$$

$$\tau^{-1}_{pz} = \frac{K^2 e^2 m^* b k_B T}{16\pi\varepsilon_s \hbar^3} \int_0^{\pi} \left(8b^2 + 9bq + 6q^2\right)(b+q)^{-3}(q+q_s)^{-2} q\sin^2\alpha d\alpha)$$

....(4A.2)

$$\tau^{-1}_{im} = \tau^{-1}_{bi} + \tau^{-1}_{ri}$$

$$= \left(\frac{m^* e^4}{2\pi\hbar^3\varepsilon_s^2}\right)\int_0^{\pi} \left[N_B P_0^2\left(1 - e^{-2qL}\right) + N_R C_o\right]\frac{\sin^2\alpha}{2q(k+q_S p_{av})^2} d\alpha \ldots (4A.3)$$

$$\tau^{-1}_{all} = \left(\frac{m^* z(z-1)V(\Delta E)^2 3b}{16\pi\hbar^3}\right)\int_0^{\pi} \sin^4\alpha\left(\sin\alpha + \frac{q_s}{2C_2\sqrt{x}}\right)^{-2} d\alpha \ldots (4A.4)$$

$$\tau^{-1}_{sr}(K) = \frac{\Delta^2 L^2 e^4 \left(N_{depl} + \frac{1}{2}N_s\right)^2 m^*}{2\varepsilon_s^2\hbar^3}$$

$$\int_0^{2\pi} d\theta(1-\cos\theta)\exp^{\left(-k^2L^2\sin^2(\theta/2)\right)}\left(\frac{\Gamma(2k\sin(\theta/2))}{\varepsilon(2k\sin(\theta/2))}\right)^2 \ldots (4A.5)$$

According to **Matthiessen's** rule the total relaxation time for **2D EG** is,

$$\tau^{-1} = \tau^{-1}_{ac} + \tau^{-1}_{pz} + \tau^{-1}_{im} + \tau^{-1}_{all} + \tau^{-1}_{sr} \ldots (4A.6)$$

Appendix 4B

1D EG

τ_{ac}, τ_{pz},τ_{im} and τ_{sr} are the relaxation time for acoustic phonon via potential deformation, piezoelectric, ionized impurity and surface roughness scattering [Kundu, Sarkar and Basu, 1990] respectively for **1D EG.**

$$\tau^{-1}_{ac}(k) = \frac{9 E_1^2 k_B T m^* b}{(8 a \hbar^3 C_L k)} \quad ...(4B.1)$$

$$\tau^{-1}_{pz}(k) = \frac{K^2 e^2 K_B T m^* b}{32 \pi \hbar^3 \varepsilon_s a k}\{2 f'(K) + f'(K_O)\} \quad ... \ (4B.2)$$

$$\tau^{-1}_{im}(k) = \tau^{-1}_{bi}(ka) + \tau^{-1}_{ri}(ka)$$

$$= \left(\frac{\pi m^* N_B}{2\hbar^3 k^3}\right)\left(\frac{e^2}{2\pi\varepsilon_s}\right)^2 \left[1 + (ka)^2 \{K_O^2(ka) - K_1^2(ka)\}\right]$$

$$+ \left(\frac{\pi m^* N_R a^2}{2\hbar^3 k}\right)\left(\frac{e^2}{2\pi\varepsilon_s}\right)^2 \left[K_1^2(ka) - K_O^2(ka)\right] \quad ... \ (4B.3)$$

$$\tau^{-1}_{sr}(k) = \left(\frac{35}{32\pi}\right)\left(\frac{e^2 n_{1D} H d}{\varepsilon_s}\right)^2 \left(\frac{m^*}{\hbar^3 a^3}\right)\left\{\frac{\exp(-4k^2 d^2)}{k}\right\} \quad ... \ (4B.4)$$

Where K_0 and K_1 are the modified Bessel Function of the second kind of order 0 and 1 respectively.

According to **Matthiessen's rule** the total relaxation time for **1D EG** is,

$$\tau^{-1} = \tau^{-1}_{ac} + \tau^{-1}_{pz} + \tau^{-1}_{im} + \tau^{-1}_{sr} \quad ...(4B.5)$$

Appendix 4C

2D Fermi energy level

$$\eta = \frac{E_F}{k_B T} = \ln\left[e^{\frac{\pi\hbar^2 n_{2D}}{m^* k_B T}} - 1\right] \quad ... \ (4C.1)$$

1D Fermi energy level

$$\eta = \frac{E_F}{k_B T} = \ln\left[\frac{\hbar^2 n_{1D}^2}{m^* k_B T}\left(\frac{\pi}{2}\right)^3\right] \quad ...(4C.2)$$

Where,

$$\eta = \frac{E_F}{k_B T}$$

$$q_S = \frac{e^2 N_0}{2\varepsilon_o \varepsilon_s k_B T\left[\left(1+e^{-\eta}\right)\ln\left(1+e^{\eta}\right)\right]}$$

$$C_2 = \left[\frac{2m^* k_B T}{\hbar^2}\right]^{1/2}$$

$$x = \frac{E}{k_B T}$$

$$k = c_2\sqrt{x}$$

$$q = 2k$$

$$p_o = \left(\frac{b}{b+k}\right)^3$$

$$D = k + q_s p_{av}$$

$$C_o = \frac{2b^6 + 24b^5 q + 48b^4 q^2 + 43b^3 q^3 + 18b^2 q^4 + 3bq^5}{2(b+q)^6}$$

$$k_0^2 = k^2 + \frac{\pi^2}{a^2}$$

$$f'(x) = \frac{\left(4b^2 + 9bx + 6x^2\right)}{\left[x(b+2x)\right]^2}$$

$$p_{av} = \frac{3b^3 + 9b^2 k + 3bk^2}{8(b+k)^3}$$

5.1 Introduction

$Hg_{0.8}Cd_{0.2}Te$ (MCT), a narrow-direct band gap and an alloy semiconductor is selected for our work due to its application in various electronics and optoelectronic devices for different applications, such as infrared detectors [Shakouri and Chris, 1999], thermoelectric devices, such as cooler, refrigerator etc. Due to the narrow band gap, the band structure of MCT is nonparabolic and the nonparabolicity has been calculated based on Kane's model [Phadke and Sharma, 1975]. Recent study of Chen and Sher [Chen and Sher, 1982], shows that the band structure of MCT is more hyperbolic in nature rather than nonparabolic, as described by Kane.

When a magnetic field is applied to a semiconductor, electrons in the system move into a circular path due to the Lorentz force in the direction transverse to the magnetic field. The direction of the motion of the electrons is always perpendicular to the path of the electrons as well as to the direction of the magnetic field. Such electrons are quantized into various equally spaced co-centric circular orbits called Landau levels. The motion of the electrons in the longitudinal direction i.e. along the direction of the magnetic field is still free to move. In the presence of a temperature gradient along the direction of the magnetic, the system becomes more interesting because under the condition the system behaves as quasi-one dimensional (Q1D) system. At a reasonable high magnetic field, electrons would occupy the lowest Landau levels and the condition is called the extreme quantum limit (EQL). To simplify our calculations we have considered the case EQL in our work.

The importance of Q1D system in the electronic devices is due to its high mobility, which is possible due to confinement of dimensions of motion of the system. The importance of selecting MCT in our work is due to the low effective mass, which further enhances the mobility of the system. High mobility is inherently important to facilitate electron transport in the thermoelectric materials, because the high mobility reduces the Joule heating [Shakouri, 1999].

The thermal transport property known as the figure of merit of thermoelectric is defined as $Z = S^2\sigma/\kappa$ [Harmon and Honig, 1962; Egli, 1961; Rowe and Bhandari, 1983]. Where σ, S and κ are the electrical conductivity, Seebeck coefficient and the thermal conductivity respectively. Z has the dimension of inverse temperature. If we are trying to pump heat from cooler region to hotter one, we need high pumping efficiency (high S), low production of heat

through Joule heating (high σ) and low backward conduction of heat (low κ) [Sofo, Mahan and Baars, 1994]. The efficiency of thermoelectric refrigerators and generators increases with large values of ZT.

Ghose et al. [Ghose et al., 2000] has studied the variation of the conductivity with temperature and magnetic field considering all parabolic, nonparabolic and hyperbolic band structure of MCT in EQL.

Hence, we have done detailed study to calculate different important transport parameters of MCT such as, mobility, conductivity, Seebeck coefficient, thermal conductivity due to electrons and lattice separately, and finally the figure of merit of the material at low and high temperatures. Considering the importance of the band structures as parabolic, nonparabolic and hyperbolic, the effects of the band nonparabolicity in the above transport parameters are also observed.

The above thermal transport parameters are calculated with the Boltzmann's transport equations considering various phonon and nonphonon scattering mechanisms such as ionized impurity (in) and alloy disorder (all), acoustic phonon via deformation potential (ac), piezoelectric (pz) scattering mechanisms. Narrow band gap semiconductors are made of elements with a large electronegativity difference. Therefore polar optical mode scattering is one of the most important scattering mechanisms [Sofo and Mahan, 1994] to be considered in our calculation. At high temperature polar optical phonon (pop) scattering mechanism is also considered in our calculations. The effects of high and low temperature scattering mechanisms on the transport parameters are also observed separately.

In the higher carrier concentration, the effect of electron-electron interaction is prominent which leads us to use Fermi-Direct statistics instead of the Maxwell- Boltzmann statistics. The effect of degeneracy on the system is also calculated and compared in our transport results.

5.2 Theoretical Formulation

5.2 (a) Band structures of MCT

We consider a nonparabolic spherically symmetric conduction band semiconductor subjected to a large longitudinal quantizing magnetic field B along z-axis which causes the electrons to occupy the lowest Landau level

i.e. Extreme Quantum Limit (EQL). A temperature gradient ΔT is also applied along the z-axis. The Boltzmann transport equation can be used in the longitudinal configuration even in the case of magnetic quantization, since the magnetic field does not produce any effect on the longitudinal motion of charge carriers.

The energy dispersion relation for the electrons subjected to a quantizing magnetic field along the z- direction for nonparabolic band based on Kane's model can be written [Phadke and Sharma, 1975] as,

$$E^{np} = \frac{\hbar^2 k_z^2}{2m^* a_o} + \left(n + \frac{1}{2}\right) E_g \left(a_o - 1\right) \qquad ...(5.1)$$

Where the 1st term in the equation (5.1), $\left(\hbar^2 k_z^2 / 2m^* a_o\right)$ gives the longitudinal component of energy $\left(E_{oz}\right)$ along z-axis. In the expression k_z is the z-component of the wave vector. m^* and $\hbar$ in the equation (5.1) are the effective mass and Plank's constant divided by 2π respectively.

The second term of the equation (5.1) gives transverse component of quantized energy along xy-plane due to the presence of magnetic field. E_g is the band gap energy. n is Landau subband index and a_o being the nonparabolicity factor is given as,

$$a_o = \left[1 + 2\hbar\omega_c \left(1 - |g| \frac{m^*}{2m_o}\right) \Big/ E_g\right]^{1/2} \qquad ...(5.2)$$

In the equation (5.2), $|g|$ and $\omega_c = \left(Be/m^*\right)$ are the Lande's g-factor and the cyclotron frequency respectively. Where, e, m_o and B are the charge of an electron, free electron mass and magnetic flux density respectively.

The wide band gap parabolic semiconductor material means E_g to be large i.e. $E_g \to \infty$. At the condition $a_o \to 1$. Hence, nonparabolicity factor $\left(a_o\right)$ reduces to unity. The energy dispersion relation given by equation (5.1) for parabolic band structure reduces and is given as,

$$E^p = \frac{\hbar^2 k_z^2}{2m*} + \left(n + \frac{1}{2}\right)\hbar\omega_c \left(1 - |g| \frac{m^*}{m_o}\right) \qquad ...(5.3)$$

The hyperbolic band structure has been suggested by Krishnamurthy and Sher [Krishnamurthy and Sher, 1995] for narrow gap semiconductor such as MCT on the basis of experimental interpretation of transport parameters of MCT and is given as,

$$E^h = \left(\gamma k^2 + c^2\right)^{\frac{1}{2}} - c \qquad ...(5.4)$$

$$\text{where } k^2 = \left(n + \frac{1}{2}\right)\frac{2eB}{\hbar} + k_z^2 \qquad ...(5.5)$$

The terms γ and c in equation (5.4) are adjusted parameters to fit the experimentally observed band structure in the energy range of interest [Krishnamurthy and Sher, 1994]. The hyperbolic band structure of equation (5.4) is simplified to make a comparative study with parabolic and nonparabolic band structures. The simplified from of the hyperbolic band structure in similar form of equations (5.1) and (5.3) is obtained. The detail calculation is given in **Appendix 5A**.

$$E^h = \frac{\hbar^2 k_z^2}{2m^* a_0^h} + \sqrt{\left(\frac{\gamma\hbar e}{\hbar} + c^2\right)} - c \qquad ...(5.6)$$

The nonprabolicity factor for hyperbolic band structure $\left(a_o^h\right)$ is ,

$$a_o^h = \frac{\hbar^2}{m^*\gamma}\sqrt{\left(\frac{\gamma\hbar e}{\hbar} + c^2\right)} \qquad ...(5.7)$$

5.2 (b) Electrical Transport Parameters

5.2 (b) i. Mobility

An important transport parameter of semiconductor devices is mobility. In the presence of a high magnetic field, all the electrons in the conduction band occupy the lowest Landau energy level and the situation is called the extreme quantum limit [EQL]. The mobility of electrons in the EQL can be expressed as,

$$\mu = \frac{2e}{\sqrt{\pi}m^* a_o}\langle\tau\rangle \qquad ...(5.8)$$

The symbol $\langle\ \rangle$ in equations (5.8) indicates the average over energy incorporating the carrier distribution function f_0. In the presence of magnetic field, f_0 also gets modified and becomes magnetic field dependent due to Fermi energy (E_F) being magnetic field dependent. f_0 is also called the equilibrium distribution function and the value of which depends on carrier concentrations and temperature.

For **nondegenerate case** (lightly doped semiconductor), the Fermi energy E_F lies just below the band edge, the equilibrium distribution function $f_o(E_{oz})$ in such case is given by Maxwell Boltzman distribution as follow,

$$f_o(E_{oz}) = \exp\left(\frac{E_{F1}(B) - E_{oz}}{k_B T}\right) \qquad ...(5.9)$$

The mobility relation of equation (5.8) in the case of EQL [Chattopadhya and Nag, 1976] becomes,

$$\mu = \frac{2e}{\sqrt{\pi} m^* a_o} \int_0^\infty x^{1/2} \tau(x) \exp^{(-x)}\, dx \qquad ...(5.10)$$

Where $x = E_{oz}/k_B T$ with k_B, the Boltzmann's constant and T being the electron temperature in Kelvin.

For **degenerate case** (heavily doped semiconductor) under $E_F \rangle\rangle k_B T$, the equilibrium distribution function $f_o(E_{oz})$ is obtained by using Fermi-Dirac distribution and is given below,

$$f_o(E_{oz}) = \left[1 + \exp\left(\frac{E_{oz} - E_{F2}(B)}{k_B T}\right)\right]^{-1} \qquad ...(5.11)$$

Where the magnetic field dependent Fermi energy ($E_F(B)$) [Nag, 1980, Arora and Jaafarin, 1976], in equations (5.9) and (5.11) for nondegenerate and degenerate semiconductors respectively is given in **Appendix 5B**. The presence of a magnetic field generally lowers the Fermi level compared to the bulk and the material becomes less degenerate. In EQL the Fermi level lies below the lower edge of the second subband, so that only one subband is

occupied by the electrons. This condition occurs when the magnetic field is very large so that $\hbar\omega_c$ is larger than $E_F(B)$.

Due to higher concentration of doping, the effect of electron-electron interaction can not be ignored. Under such condition semiconductor becomes degenerate and the degenerate mobility relation is given as [Banerji, 1995],

$$\mu = \frac{2e}{m^* a_0} \frac{\int_0^\infty x^{1/2} \tau(x) f_o (1 - f_o) \partial x}{\int x^{-1/2} f_o \partial x} \qquad \ldots(5.12)$$

Knowing the mobility, from equations (5.10) and (5.12) for nondegenerate and degenerate cases, one can obtain the electrical conductivity (σ) using the relation $\sigma = ne\mu$, where n is the corresponding carrier concentrations applicable for nondegenerate and degenerate cases respectively.

$\tau(x)$ in equations (5.10) and (5.12) is the total momentum relaxation time for nonpnonon scattering mechanisms such as ionized impurity (in) and alloy disorder (all) scattering, found to be dominant in alloy semiconductor, such as MCT at low temperatures and phonon scattering mechanisms, such as acoustic phonon via deformation potential (ac), piezoelectric (pz) scattering mechanisms are dominant at low temperature and polar optical phonon (pop) scattering mechanism, dominant at high temperatures. The expressions for individual scattering mechanisms are given in the **Appendix 5C**. The total momentum relaxation time in both cases is obtained by combining them and using Matthiessen's rule.

5.2 (b) ii. Seebeck Coefficient

Seebeck coefficient is another interesting and important thermal transport parameter, due to the fact that it gives an idea of scattering processes operative and the nature of the band structure. In the presence of a temperature gradient parallel to the applied high magnetic field along z-direction, one can use the Boltzmann transport equation to compute the longitudinal Seebeck coefficient similar, to the mobility calculation. The relation for Seebeck coefficient is given [Nag, 1980] as,

$$S = \frac{\xi}{\nabla_z T} = -\frac{k_B}{e}\left[-\frac{E_F(B)}{k_B T} + \frac{\langle \mathrm{E}\tau \rangle}{\langle \tau \rangle k_B T}\right] \qquad ...(5.13)$$

The 1st term in the equation (5.13) gives the magnetic field dependent Fermi level term and the 2nd term is the scattering term in the form of ratio.

The equation (5.13) is applicable for both degenerate and nondegenerate cases. The Fermi energy term and the average scattering term with proper carrier distributions have to be taken according to the condition of degeneracy i.e. for nondegenerate and degenerate cases, $E_F(B)$ and $\langle \tau \rangle$ in the equation (5.13) are taken separately. $\langle E\tau \rangle$ is calculated in the same way as $\langle \tau \rangle$ is calculated.

5.2 (b) iii. Thermal Conductivity

For a semiconductor, there are two separate contributions to the thermal conduction. The conduction due to the vibration of the atoms about their position of the thermal equilibrium (lattice vibrations for crystals) and that due to the mobile charge carries electrons or holes. The thermal conductivity due to the former is denoted by κ_l and that due to the latter is denoted by κ_e for n-type semiconductors.

The **electronic thermal conductivity,** κ_e [Smith, 1989] can be expressed as,

$$\kappa_e = \sigma L \mathrm{T} \qquad ...(5.14)$$

Where the Lorentz ratio, L is given as,

$$L = \mathcal{L}\left(\frac{\mathrm{k_B^2}}{e^2}\right) \qquad ...(5.15)$$

$$\text{where} \quad \mathcal{L} = \frac{\langle \tau \rangle \langle \mathrm{E}^2\tau \rangle - \langle \mathrm{E}\tau \rangle^2}{k_\mathrm{B}^2 \mathrm{T}^2 \langle \tau \rangle^2} \qquad ...(5.16)$$

The expression $\langle E^2\tau \rangle$ is also calculated in the similar way mentioned earlier.

The **Lattice thermal conductivity,** κ_l calculation is based on Callaway's phenomenological theory [Callaway, 1959]. In Callaway's formula the lattice thermal conductivity is given as,

$$\kappa_l = \left(\frac{k_B}{\hbar}\right)^3 \frac{k_B}{2\pi^2 \nu} T^3 \int_0^{T_D/T} \frac{x'^4 \tau_l e^{x'}}{\left(e^{x'}-1\right)^2} \partial x' \qquad ...(5.17)$$

Where T_D is the Debye temperature. $x' = \hbar\omega / k_B T$, where ω is the phonon frequency. The phonon relaxation time (τ_l) is determined by the phonon boundary scattering [Puri and Geballe, 1966] i.e. $\tau_l = L'/\nu$, L' is the shortest dimensional of the sample. The phonon once strikes the boundary of the sample loses all it coherence. Hence τ_l is defined by the shortest length of the sample (L') along with velocity of sound (ν), ν is taken separately for acoustic sound velocity (u_{ac}) and the piezoelectric sound velocity (u_{pz}).

5.2 (b) iv. Figure of merit

MCT has also the potential to use as a material for thermoelectric cooling devices [Goldsmid, 1986].

Due to the low effective mass MCT has very high conductivity and it is necessary to optimize the performance of thermoelectric devices such as cooler, refrigerator and generators. The study of the figure of merit (Z) for narrow gap semiconductor in the presence of longitudinal quantizing magnetic field in EQL is an important aspect of our study for its utility of narrow gap semiconductor as thermoelectric cooler. The figure of merit Z is expressed as [Harmon and Honig, 1962; Egli, 1961; Rowe and Bhandari, 1983],

$$Z = S^2 \left(\frac{\sigma}{\kappa}\right) \qquad ...(5.18)$$

where $\kappa = \kappa_e + \kappa_l$

5.3 Results and Discussions

The material parameters for MCT are given in Parameter table of MCT. For hyperbolic band structure the constants are taken as, $\gamma = 48.3 \times 10^{-20} e^2$ and $c = 0.058e$ [Krishnamurthy and Sher, 1994]. The calculations have been done

with the carrier concentrations of $1\times10^{20}\,m^{-3}$ and $1\times10^{22}\,m^{-3}$ for nondegenerate and degenerate MCT respectively, with different nonphonon scattering mechanisms, such as ionized impurity (in) and alloy disorder (all) scattering mechanisms, and phonon scattering mechanisms, such as acoustic phonon (ac) via deformation potential, piezoelectric (pz) and polar optical phonon (pop) scattering mechanisms. Polar optical phonon (pop) scattering mechanism is active in the higher temperature region beyond 77K. The expressions for the various scatterings mechanisms are given in the **Appendix 5C.** The total scattering mechanism is obtained by the Matthiessen's rule is also given in the **Appendix 5C**.

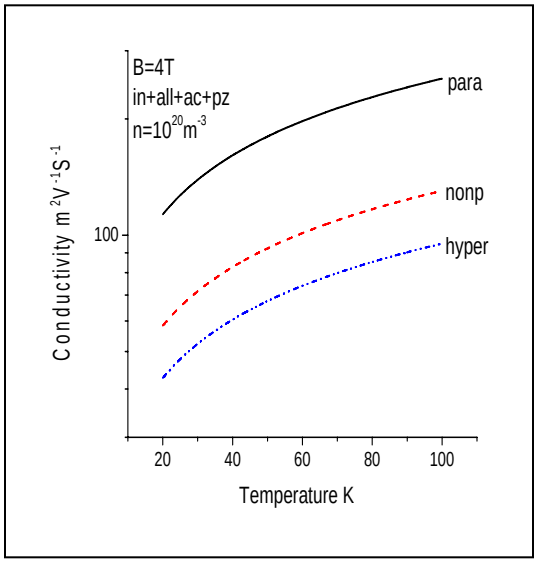

Fig. 5.1 Variation of Conductivity with temperature at constant magnetic field 4T for nondegenerate n-$Hg_{0.8}Cd_{0.2}Te$ with various scattering mechanisms such as ionized impurity (in), alloy disorder (all), acoustic phonon via deformation potential (ac) and piezoelectric (pz) scattering mechanisms.

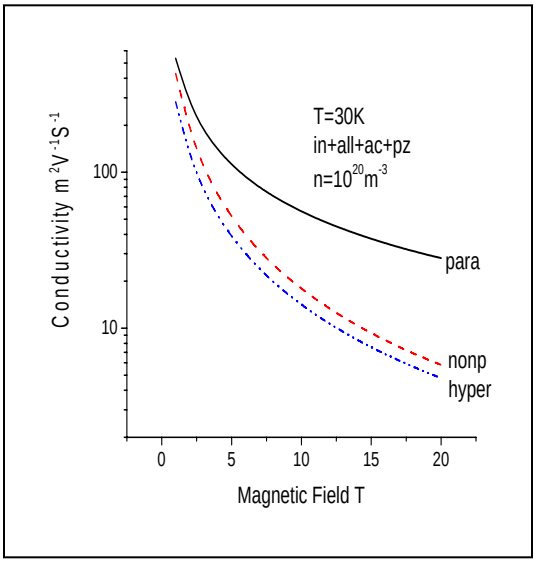

Fig.5.2 Variation of Conductivity with magnetic field at constant temperature 30K for nondegenerate n-$Hg_{0.8}Cd_{0.2}Te$ with various scattering mechanisms such as ionized impurity (in), alloy disorder (all), acoustic phonon via deformation potential (ac) and piezoelectric (pz) scattering mechanisms.

The variation of conductivity with temperatures at a constant magnetic field of 4T for nondegenerate MCT considering parabolic, nonparabolic and hyperbolic band structures with various low temperature scattering mechanisms such as ionized impurity (in), alloy disorder (all), acoustic phonon via deformation potential (ac) and piezoelectric (pz) scattering mechanisms is calculated and shown in Fig. 5.1.

Hence, with the same low temperature scattering mechanisms as described above for Fig 5.1, the variation of conductivity for nondegenerate MCT, considering all parabolic, nonparabolic and hyperbolic band structures with magnetic field at a constant temperature of 30K is observed and is given in Fig. 5.2.

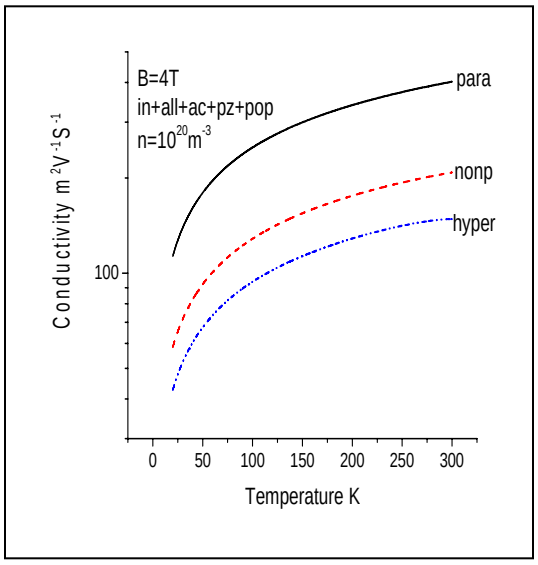

Fig. 5.3 Variation of Conductivity with temperature at constant magnetic field 4T for nondegenerate n-$Hg_{0.8}Cd_{0.2}Te$ with various scattering mechanisms such as ionized impurity (in), alloy disorder (all), acoustic phonon via deformation potential (ac), piezoelectric (pz) and polar optical phonon (pop) scattering mechanisms.

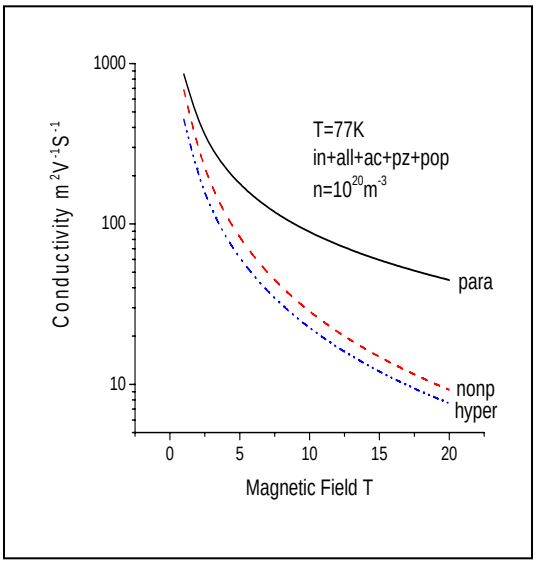

Fig. 5.4 Variation of Conductivity with magnetic field at constant temperature 77K for nondegenerate n-$Hg_{0.8}Cd_{0.2}Te$ with various scattering mechanisms such as ionized impurity (in), alloy disorder (all), acoustic phonon via deformation potential (ac), piezoelectric (pz) and polar optical phonon (pop) scattering mechanisms.

The study of the transport parameters in higher temperatures is interesting because in higher temperatures the system is affected by some more microscopic phenomena, such as the scattering due to polar optical phonon (pop). Hence we have studied the variation of conductivity, in Fig. 5.3 with temperature at a constant magnetic field of 4T for nondegenerate MCT with the lower temperature scattering mechanism as mentioned above like ionized impurity (in), alloy disorder (all), acoustic phonon via deformation potential (ac) and piezoelectric (pz) along with the higher temperature scattering mechanism, the polar optical phonon (pop) scattering.

Similarly, in the Fig 5.4 the variation of conductivity with magnetic field for nondegenerate MCT at a constant temperature of 77K for all the scattering mechanism taken for Fig 5.3 is shown.

In the higher carrier concentration, the distribution of carriers is determined by Fermi-Dirac statistics instead of Maxwell-Boltzmann.

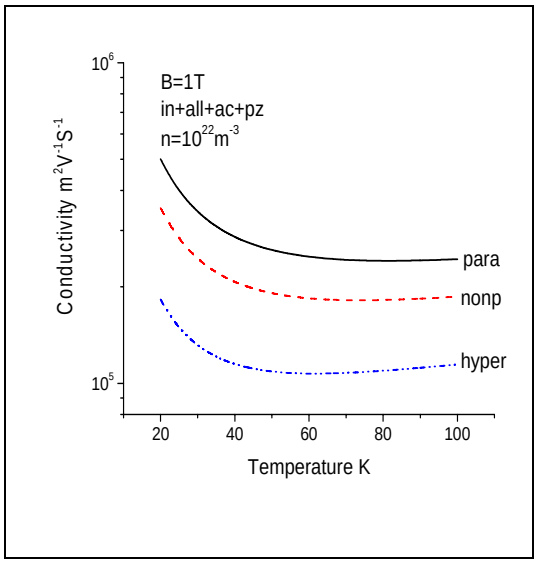

Fig. 5.5 Variation of Conductivity with temperature at constant magnetic field 1T for degenerate n-$Hg_{0.8}Cd_{0.2}Te$ with various scattering mechanisms such as ionized impurity (in), alloy disorder (all), acoustic phonon via deformation potential (ac) and piezoelectric (pz) scattering mechanisms.

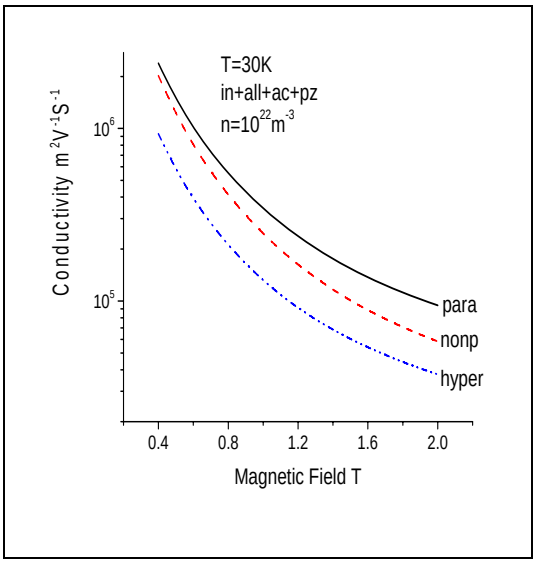

Fig. 5.6 Variation of Conductivity with magnetic field at constant temperature 30K for degenerate n-$Hg_{0.8}Cd_{0.2}Te$ with various scattering mechanisms such as ionized impurity (in), alloy disorder (all), acoustic phonon via deformation potential (ac) and piezoelectric (pz) scattering mechanisms.

With the carrier concentration of $10^{22}\,m^{-3}$, the variation of conductivity with temperature at a constant magnetic field of 1T for degenerate MCT considering parabolic, nonparabolic and hyperbolic band structures, with low temperature scattering mechanisms, such as ionized impurity (in), alloy disorder (all), acoustic phonon via deformation potential (ac) and piezoelectric (pz) scattering mechanisms is calculated and the results are presented in Fig. 5.5.

Fig. 5.6 shows the variation of conductivity for degenerate MCT with magnetic field at a constant temperature of 30K with the same low temperature scattering mechanisms as those taken for Fig. 5.5.

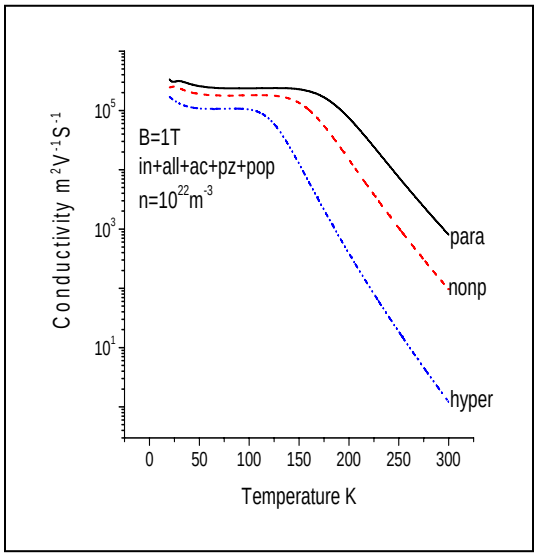

Fig. 5.7 Variation of Conductivity with temperature at constant magnetic field 1T for degenerate n-$Hg_{0.8}Cd_{0.2}Te$ with various scattering mechanisms such as ionized impurity (in), alloy disorder (all), acoustic phonon via deformation potential (ac), piezoelectric (pz) polar optical phonon (pop) scattering mechanisms.

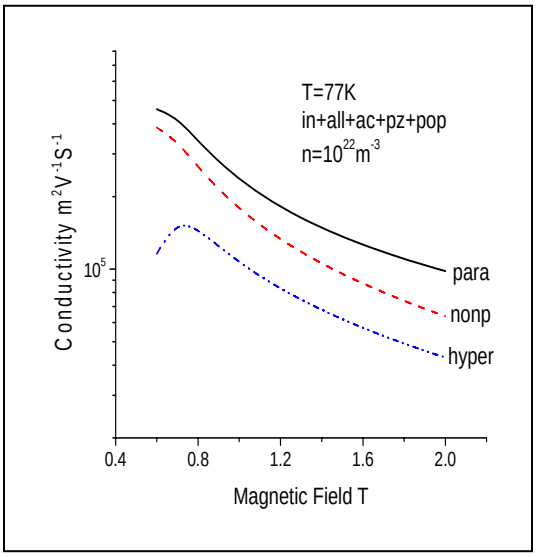

Fig. 5.8 Variation of Conductivity with magnetic field at constant temperature 77K for degenerate n-$Hg_{0.8}Cd_{0.2}Te$ with various scattering mechanisms such as ionized impurity (in), alloy disorder (all), acoustic phonon via deformation potential (ac), piezoelectric (pz) and polar optical phonon (pop) scattering mechanisms.

Including, the polar optical phonon (pop) scattering mechanism, dominant at higher temperature along with the low temperature scattering mechanisms, the variation of conductivity with temperature at a constant magnetic field of 1T for degenerate MCT for parabolic, nonparabolic and hyperbolic band structures is shown in Fig. 5.7. Whereas, the variation of conductivity with magnetic field at a constant temperature of 77K for degenerate MCT for all the three different types of band structures with the scattering mechanism taken for Fig 5.7 is given in Fig. 5.8.

In Fig. 5.5, we see that conductivity decreases with increasing in temperatures. It is expected due to decreasing of the mean free path with increasing temperature, since in such case, more phonons are excited and more scattering events are taking place.

In case of alloy semiconductor like MCT, the mobility is totally governed by the scattering of the carries due to alloy disorder potential. The effect of other scattering mechanism such as acoustic phonon via deformation potential (ac) and piezoelectric (pz) scattering mechanisms become dominant at high temperature, still they do not have any significant effect on the mobility. However, more and more scattering mechanisms become active at higher temperatures and mobility is found to decrease with increasing temperature.

At very high temperatures the effect of polar optical phonon (pop) is found to be more significant because of which the conductivity decreases more steeply as we can see in Fig. 5.7.

The presence of the peak in the temperatures range 70K to 140K, found in Fig. 5.7 as observed, and is explained by Krishnamurth and Sher [Krishnamurthy and Sher, 1994] also. However, the author's [Krishnamurthy and Sher, 1994] results are based on the bulk, degenerate MCT mobility in the absence of magnetic field.

The results of Figs. 5.2, 5.4, 5.6 and 5.8 show that the conductivity decreases with the increase in magnetic field. The magnetic field dependence of the longitudinal resistively (inverse of mobility) is obtained as $B^{n'}$. Similar dependence of mobility for InSb has been observed by Alive et al. and Huff et al. [Alive et al., 1975; Huff et al., 1968].

The magnetic field increases the band nonparabolicity. The nonparabolicity increases the effective mass which also increases the scattering rate [Basu, Sarkar and Chattopadhyay, 1988] and which decreases the mobility [Arora and Jaafarian, 1976; Wu and Spector, 1971].

Figs. 5.1-5.8 show the values of the conductivity is maximum for parabolic and are followed by nonprababolic and hyperbolic band structures respectively. Benerji [Banerji, 1995] has also observed the similar nature of the curves in his theoretical calculations. Benerji compared his result with the experiment results of Nimtz and Gebhardt, [Nimtz and Gebhardt, 1987] at 4.2K and has found to agree the results for nondegnerate MCT.

The nonparabolicity factor for parabolic band structure is one, whereas it is observed to be 1.56208 and 1.92635 for nonparabolic and hyperbolic band

structures respectively at the temperature of 30K and the magnetic field 4.0T. This shows that the nonparabolicity is in the order of $1 \le a_o \le a_o^h$.

The values of the conductivities are observed to be higher for degenerate MCT as compared to that of nondegnerate.

The Fermi energy relations are given in **Appendix 5B**. The magnetic field dependent Fermi Energy Level (η) variation with temperature at a constant magnetic field of 4T is shown in Fig. 5.9, whereas Fig 5.10 shows similar variation of Fermi Energy Level (η) with magnetic field at a constant temperature of 77T for nondegenerate MCT.

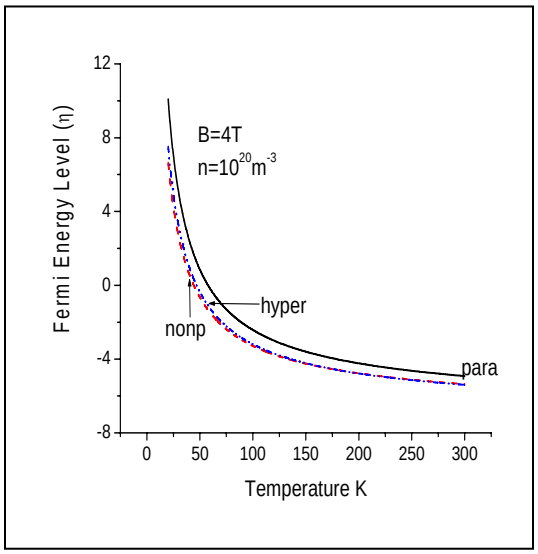

Fig. 5.9 Variation of Fermi Energy Level (η) with temperature at constant magnetic field 4T for nondegenerate n-$Hg_{0.8}Cd_{0.2}Te$.

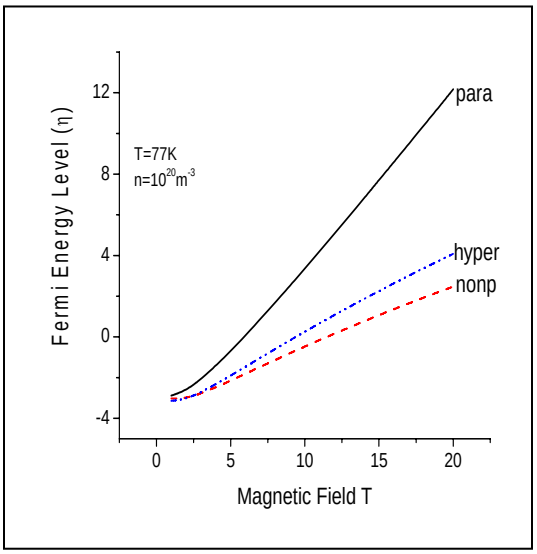

Fig. 5.10 Variation of Fermi Energy Level (η) with magnetic field at constant temperature 77K for nondegenerate n-$Hg_{0.8}Cd_{0.2}Te$.

Fig. 5.11 shows the variation of Fermi Energy Level (η) with temperature at a constant magnetic field of 1T for degenerate MCT. Similarly, Fig. 5.12 shows the variation of Fermi Energy Level (η) with magnetic field at constant temperature of 77K for degenerate MCT.

Fig. 5.12 shows that the Fermi energy decreases with magnetic field and is expected due to the material becoming less degenerate with increases in temperature.

Seebeck coefficient is a difference between the magnetic field dependent Fermi energy and the average scattering mechanisms in the form of ratio and are given in Figs. 5.13- 5.16 for nondegenerate MCT.

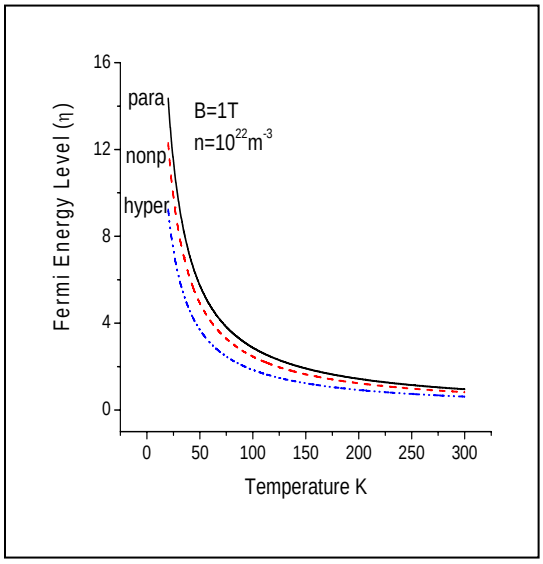

Fig. 5.11 Variation of Fermi Energy Level (η) with temperature at constant magnetic field 1K for degenerate n-$Hg_{0.8}Cd_{0.2}Te$.

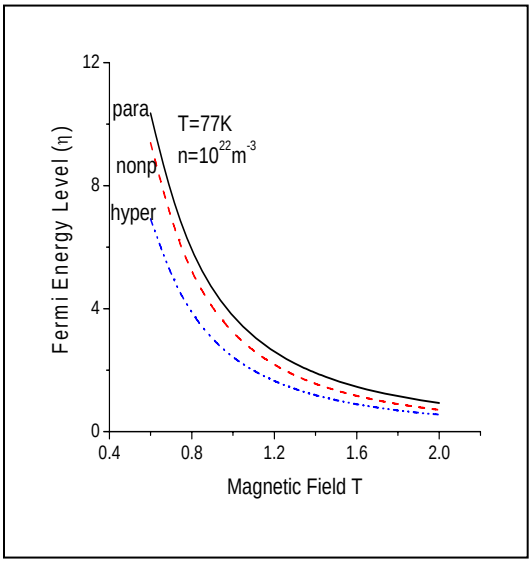

Fig. 5.12 Variation of Fermi Energy Level (η) with magnetic field at constant temperature 77K for degenerate n-$Hg_{0.8}Cd_{0.2}Te$.

The variation of Seebeck coefficient with temperature at a constant magnetic field 4.0T for nondegenerate MCT, is given in Fig. 5.13 with all low temperature scattering mechanisms, such as ionized impurity (in), alloy disorder (all), acoustic phonon via deformation potential (ac) and piezoelectric (pz) scattering mechanisms.

With the low temperature scattering mechanisms used in Fig. 5.13, the Fig. 5.14 also shows the variation of Seebeck coefficient with magnetic field at a constant temperature of 30K for nondegenerate MCT.

Fig. 5.15 shows that the variation of Seebeck coefficient with temperature at a constant magnetic field 4.0T for nondegenerate MCT with low temperature scattering mechanisms as used in Fig. 5.13 and Fig. 5.14 with an additional high temperature scattering mechanism i.e. polar optical phonon (pop) scattering mechanism.

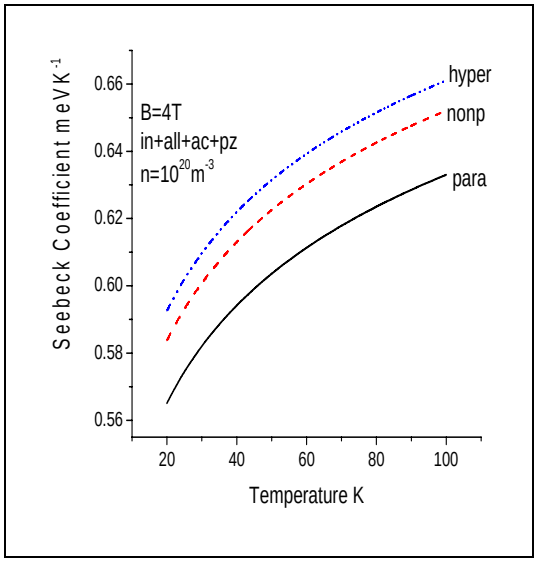

Fig. 5.13 Variation of Seebeck coefficient with temperature at constant magnetic field 4T for nondegenerate n-$Hg_{0.8}Cd_{0.2}Te$ with various scattering mechanisms such as ionized impurity (in), alloy disorder (all), acoustic phonon via deformation potential (ac) and piezoelectric (pz) scattering mechanisms.

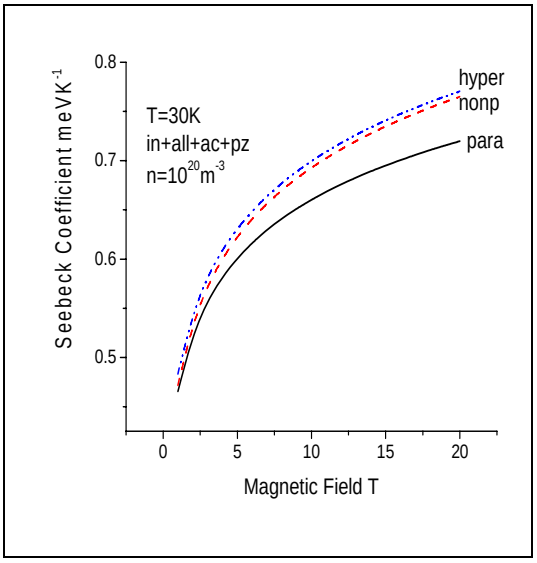

Fig. 5.14 Variation of Seebeck coefficient with magnetic field at constant temperature 30K for nondegenerate n-$Hg_{0.8}Cd_{0.2}Te$ with various scattering mechanisms such as ionized impurity (in), alloy disorder (all), acoustic phonon via deformation potential (ac) and piezoelectric (pz) scattering mechanisms.

Similar to Fig. 5.15, Fig. 5.16 is plotted to show the variation of Seebeck coefficient with magnetic field at a constant temperature 77K for nondegenerate MCT with the scattering mechanisms used in Fig. 5.15.

The variation of Seebeck coefficient with temperature at a constant magnetic field 1.0T for degenerate MCT with ionized impurity (in), alloy disorder (all), acoustic phonon via deformation potential (ac) and piezoelectric (pz) scattering mechanisms is presented in Fig. 5.17.

Similar variation of Seebeck coefficient with magnetic field at a constant temperature 30K for degenerate MCT is shown in Fig. 5.18 with all the scattering mechanisms taken as that for Fig. 5.17.

Fig 5.19 shows the variation of Seebeck coefficient with temperature at a constant magnetic field 1.0T for degenerate MCT with the ionized impurity (in), alloy disorder (all), acoustic phonon via potential deformation (ac),

Piezoelectric (pz) and polar optical phonon (pop) scattering mechanisms. Whereas, the variation of Seebeck coefficient with magnetic field at a constant temperate 77K for degenerate MCT with all the scattering mechanisms as that used in Fig. 5.19, is shown in Fig. 5.20

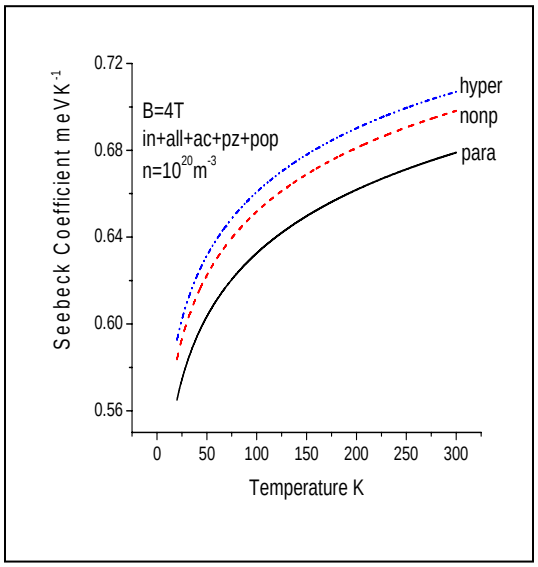

Fig. 5.15 Variation of Seebeck coefficient with temperature at constant magnetic field 4T for nondegenerate n-$Hg_{0.8}Cd_{0.2}Te$ with various scattering mechanisms such as ionized impurity (in), alloy disorder (all), acoustic phonon via deformation potential (ac), piezoelectric (pz) and polar optical phonon (pop) scattering mechanisms.

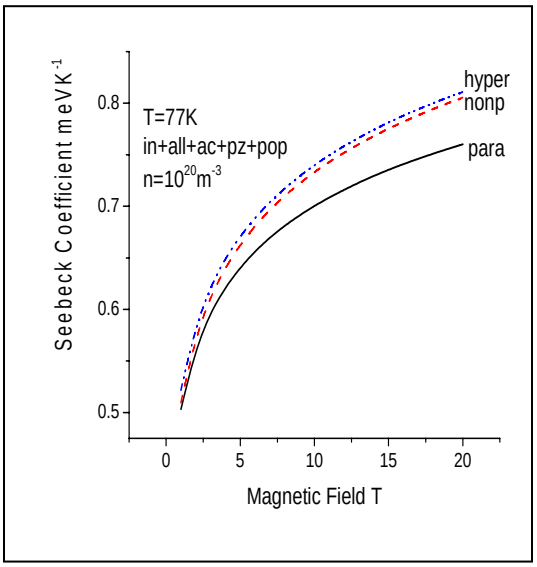

Fig. 5.16 Variation of Seebeck coefficient with magnetic field at constant temperature 77K for nondegenerate n-$Hg_{0.8}Cd_{0.2}Te$ with various scattering mechanisms such as ionized impurity (in), alloy disorder (all), acoustic phonon via deformation potential (ac), piezoelectric (pz) and polar optical phonon (pop) scattering mechanisms.

From the above results we can conclude that the Seebeck coefficient increases with the magnetic field due to the fact that the Seebeck coefficient is a difference between the Fermi energy term and the scattering term in the form of ratio. The Fermi energy term increases with the magnetic field for nondegenerte MCT as shown in Fig. 5.10. Whereas, the scattering term in the form of ratio is not altered much due to the magnetic field variation. Thus, one term increases with magnetic field and the other remains constant with the magnetic field which causes the Seebeck coefficient to increase.

Fermi energy term decreases sharply with temperature in the presence of quantizing magnetic field, while the second term in the form of ratio remains

unchanged with temperature variation. It causes Seebeck coefficient to increase with temperature for nondegenerate MCT [Santra, 1994].

For degenerate system, the magneto thermopower or Seebeck coefficient is weakly dependent on scattering mechanisms and is inversely proportional to the Fermi energy [Nag, 1980] and causes the coefficient to increase with the magnetic field.

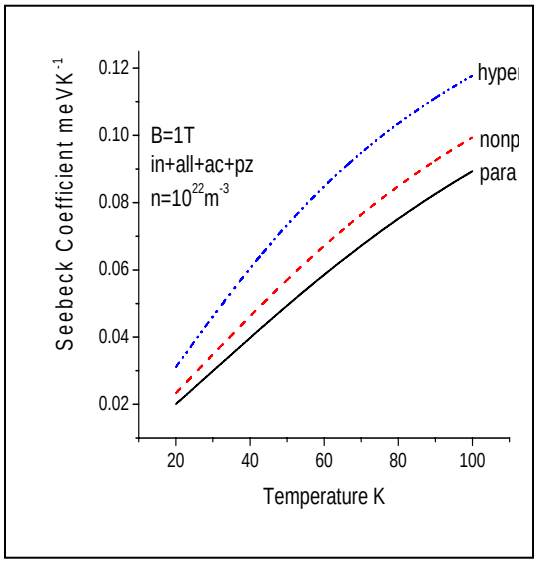

Fig. 5.17 Variation of Seebeck coefficient with temperature at constant magnetic field 1T for degenerate n-$Hg_{0.8}Cd_{0.2}Te$ with various scattering mechanisms such as ionized impurity (in), alloy disorder (all), acoustic phonon via deformation potential (ac) and piezoelectric (pz) scattering mechanisms.

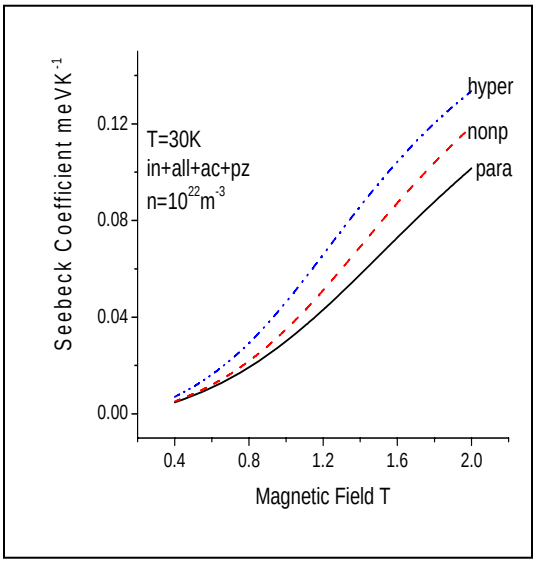

Fig. 5.18 Variation of Seebeck coefficient with magnetic field at constant temperature 30K for degenerate n-$Hg_{0.8}Cd_{0.2}Te$ with various scattering mechanisms such as ionized impurity (in), alloy disorder (all), acoustic phonon via deformation potential (ac) and piezoelectric (pz) scattering mechanisms.

For denegnerate semiconductor Seebeck coefficient is inversely proportional to the Fermi energy [Kubukaddi and Mulimani, 1985] and the Fermi energy decreases with increases of temperature which causes the Seebeck coefficient to increase with temperature.

Figs. 5.13-5.20 show that the Seebeck coefficient is maximum for hyperbolic band structure and is followed by nonparabolic and parabolic band structures respectively, verify the effect of nonparabolicty factor given by equations

(5.2) and (5.7) for nonparabolic and the hyperbolic band structures respectively is significant.

The wavy nature in the curve of Fig. 5.19 may be due to the interplay of high and low temperatures phonon scattering mechanisms.

The variation of electronic thermal conductivity with temperature at a constant magnetic field of 4.0T for nondegenerate MCT with ionized impurity (in), alloy disorder (all), acoustic phonon via deformation potential (ac), piezoelectric (pz) and polar optical phonon (pop) scattering mechanisms has also been calculated and is shown in Fig. 5.21. Whereas Fig. 5.22 shows the variation of electronic thermal conductivity with magnetic field at a constant temperature 77K for nondegenerate MCT with all scattering mechanisms taken as that for Fig. 5.21.

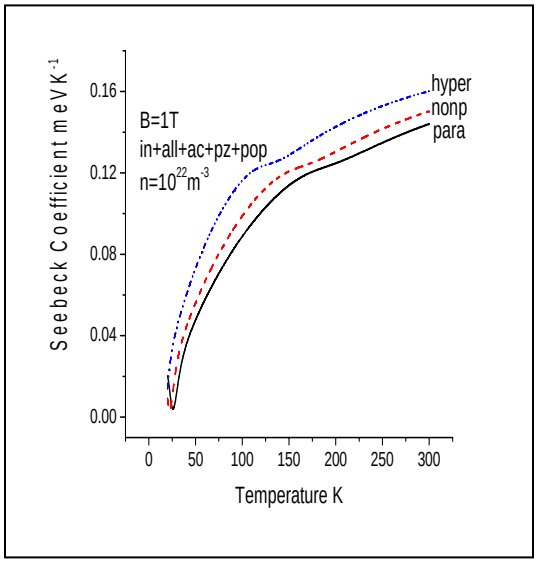

Fig. 5.19 Variation of Seebeck coefficient with temperature at constant magnetic field 1T for degenerate n-$Hg_{0.8}Cd_{0.2}Te$ with various scattering mechanisms such as ionized impurity (in), alloy disorder (all), acoustic phonon via deformation potential (ac), piezoelectric (pz) and polar optical phonon (pop) scattering mechanisms.

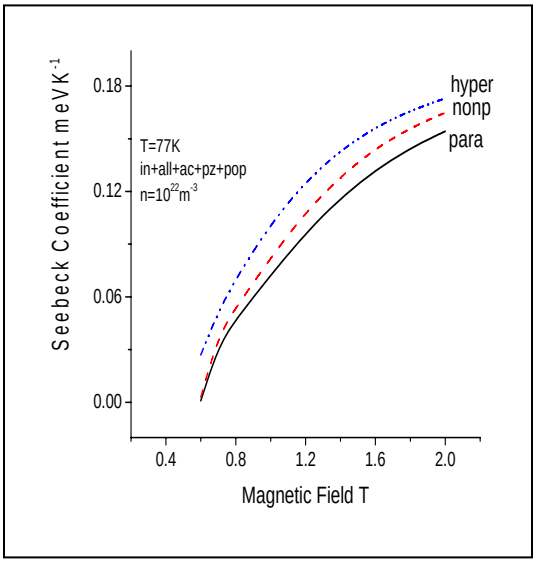

Fig. 5.20 Variation of Seebeck coefficient with magnetic field at constant temperature 77K for degenerate n-$Hg_{0.8}Cd_{0.2}Te$ with various scattering mechanisms such as ionized impurity (in), alloy disorder (all), acoustic phonon via deformation potential (ac) , piezoelectric (pz) and polar optical phonon (pop) scattering mechanisms.

Fig. 5.23 shows the variation of electronic thermal conductivity with temperature at a constant magnetic field 1.0T for degenerate MCT with all the scattering mechanisms as that taken for curves of Fig. 5.21 and 5.22.

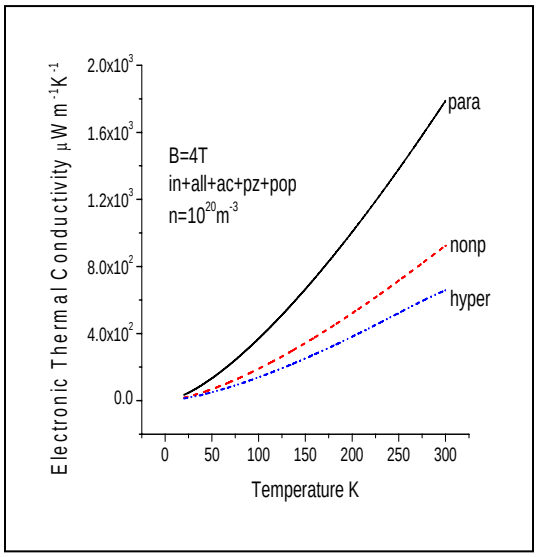

Fig. 5.21 Variation of Electronic Thermal Conductivity with temperature at constant magnetic field 4T for nondegenerate n-$Hg_{0.8}Cd_{0.2}Te$ with various scattering mechanisms such as ionized impurity (in), alloy disorder (all), acoustic phonon via deformation potential (ac), piezoelectric (pz) and polar optical phonon (pop) scattering mechanisms.

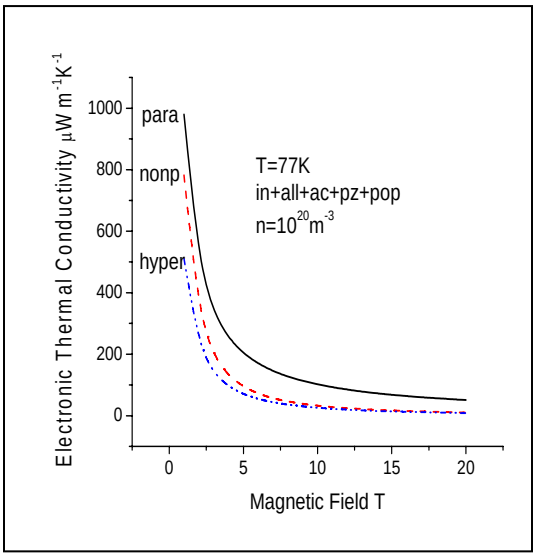

Fig. 5.22 Variation of Electronic Thermal Conductivity with magnetic field at constant temperature 77K for nondegenerate n-$Hg_{0.8}Cd_{0.2}Te$ with various scattering mechanisms such as ionized impurity (in), alloy disorder (all), acoustic phonon via deformation potential (ac), piezoelectric (pz) and polar optical phonon (pop) scattering mechanisms.

Similarly, Fig. 5.24 is plotted to show the variation of electronic thermal conductivity with magnetic field at a constant temperature 77K for degenerate MCT with all low and high temperatures scattering mechanisms used in Fig. 5.23.

The thermal conductivity due to electrons is given in Figs. 5.22 and 5.24, is mainly determined by electrical conductivity curve. Hence, the nature of the thermal conductivity curve in the figures is found to be similar to that of the electrical conductivity curves. A slight variation in curves of Figs. 5.21 and 5.23 as compared to that of Figs. 5.3 and 5.7 respectively is given and is due

to dependence of electronic thermal conductivity on T along with σ. The magnitude of Lorentz ratio (L) being very small and is almost constant.

In order to calculate the thermal conductivity due to lattice, the boundary phonon scatterings due to phonon relaxations are considered. The phonon life time relation is $\tau_l = L'/\nu$. Where L' is the shortest dimension of the sample which is taken as 0.052 cm [Santra, 1994]. The velocity of sound (ν) for acoustic and piezoelectric velocities of sound is given in the Parameter table. Debye temperature (T_θ) for MCT is taken as 300K [Stadler and Nimtz, 1986]. The magnetic field does not have any effect on lattice atoms, hence the lattice thermal conductivity is independent of magnetic field. The effect of band structure is not applicable for lattice atoms, it is only for electrons in the conduction and valence bands.

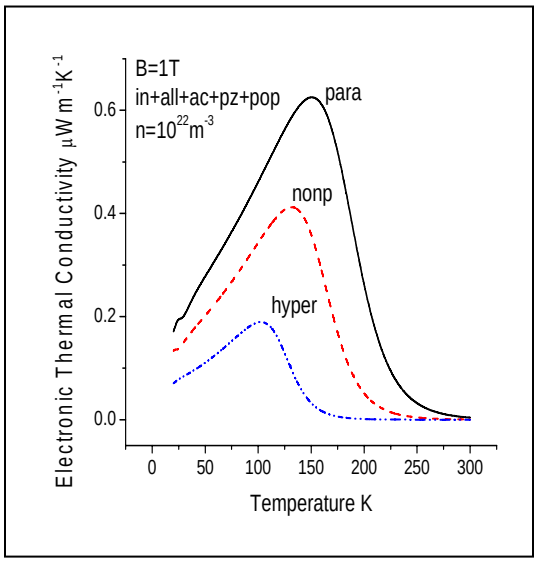

Fig. 5.23 Variation of Electronic Thermal Conductivity with temperature at constant magnetic field 1T for degenerate n-$Hg_{0.8}Cd_{0.2}Te$ with various scattering mechanisms such as ionized impurity (in), alloy disorder (all), acoustic phonon via deformation potential (ac), piezoelectric (pz) and polar optical phonon (pop) scattering mechanisms.

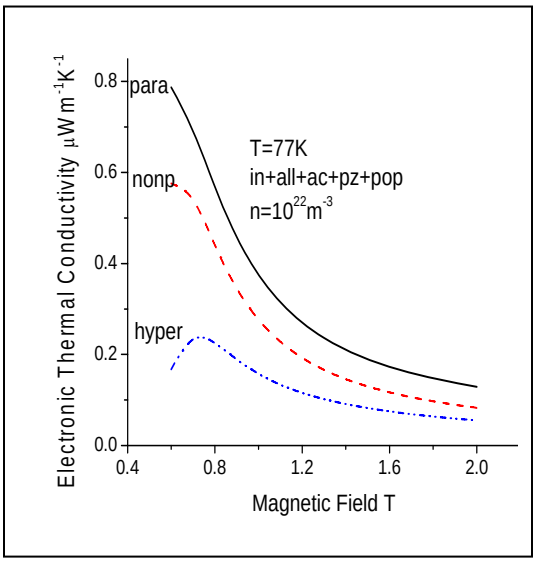

Fig. 5.24 Variation of Electronic Thermal Conductivity with magnetic field at constant temperature 77K for degenerate n-$Hg_{0.8}Cd_{0.2}Te$ with various scattering mechanisms such as ionized impurity (in), alloy disorder (all), acoustic phonon via deformation potential (ac) , piezoelectric (pz) and polar optical phonon (pop) scattering mechanisms.

The variation of the total thermal conductivity due to electron and lattice thermal conductivity with temperature at a constant magnetic field of 1T for degenerate MCT is represented in Fig. 5.25. For electronic thermal conductivity, the scattering mechanisms due to ionized impurity (in), alloy disorder (all), acoustic phonon via deformation potential (ac), piezoelectric (pz) and polar optical phonon (pop) are used. For the lattice part of the thermal conductivity, the boundary phonon scattering is taken. Fig. 5.25 shows the thermal conductivity due to lattice decrease with the increasing temperature, because the thermal resistively increases with temperature. As temperature increases, lattice atoms vibration increases. It causes more deformation in the lattice potential and produces more phonons.

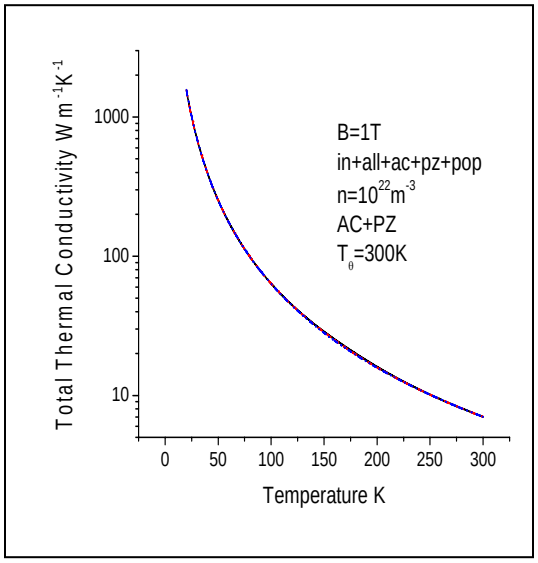

Fig. 5.25 Variation of Total Thermal Conductivity with temperature at constant magnetic field 1T for degenerate n-$Hg_{0.8}Cd_{0.2}Te$ with various scattering mechanisms such as ionized impurity (in), alloy disorder (all), acoustic phonon via deformation potential (ac) , piezoelectric (pz) and polar optical phonon (pop) scattering mechanisms. Boundary scatterings due to acoustic phonon (AC) and piezoelectric (PZ) are included for lattice thermal conductivity.

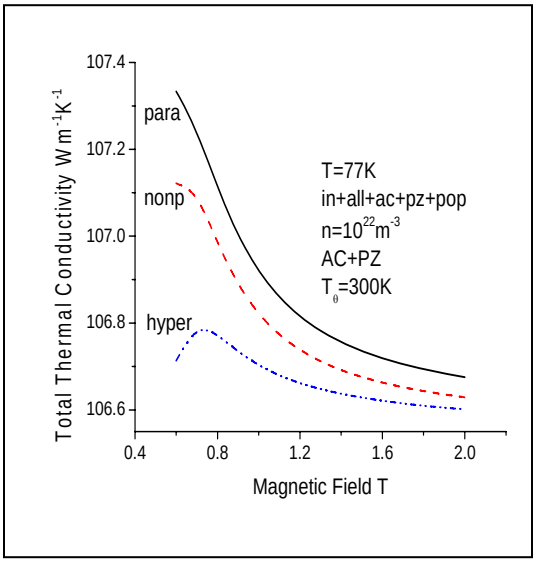

Fig. 5.26 Variation of Total Thermal Conductivity with magnetic field at constant temperature 77K for degenerate n-$Hg_{0.8}Cd_{0.2}Te$ with various scattering mechanisms such as ionized impurity (in), alloy disorder (all), acoustic phonon via deformation potential (ac) , piezoelectric (pz) and polar optical phonon (pop) scattering mechanisms. Boundary scatterings due to acoustic phonon (AC) and piezoelectric (PZ) are included for lattice thermal conductivity.

The curves in Fig 5.25 are found to be same for parabolic, nonparabolic and hyperbolic band structures; because the lattice thermal conductivity mainly dominates the electronic thermal conductivity, hence the effect of nonparabolicity does not matter.

Fig. 5.26 represents the variation of the total lattice thermal conductivity due to electron and lattice thermal conductivity with magnetic field at constant temperature 1T for degenerate MCT with the same scattering mechanisms considered in the case of curve shown in Fig. 5.25. The Fig. 5.26 shows that the nature of the curve is similar to that of the lattice thermal conductivity due to electrons presented in Fig. 5.8. But the magnitude of the parameters shown in the curve of Figs. 5.26 and 5.8 are different only by a constant value of 106.546 $Wm^{-1}K^{-1}$. It also verifies the effect of magnetic field, but does not affect for lattice atoms.

Thermal conductivity of MCT without magnetic field is calculated by Sofo and Mahan and is found to be about $2.80Wm^{-1}K^{-1}$ and $1.38Wm^{-1}K^{-1}$ at temperatures 100K and 300K respectively [Sofo, Mahan and Baars, 1994], which are very nearly closed to our calculated values for degenerate MCT, presented here in Fig. 5.25.

The figure of merit (Z_e) of MCT with thermal conductivity due to electrons only is represented by Figs. 5.27, 5.28, 5.29 and 5.30.

Fig. 5.27 shows the variation of Z_eT with temperature at a constant magnetic field 4.0T for nondegenerate MCT considering ionized impurity (in), alloy disorder (all), acoustic phonon via deformation potential (ac), piezoelectric (pz) and polar optical phonon (pop) scattering mechanisms. Whereas, Fig. 5.28 is the plot of the variation of Z_eT with magnetic field at a constant temperature 77K for nondegenerate MCT with all the scattering mechanisms used for the curve of Fig. 5. 27.

Similar variation of Z_eT is shown in Fig. 5.29 with temperature at a constant magnetic field 1.0T for degenerate MCT with all scattering mechanisms used in Figs. 5.27 and 5.28. Fig. 5.30 shows the variation of Z_eT with magnetic field at the constant temperature 77K for degenerate MCT with scattering mechanisms as described above for Fig. 5.29.

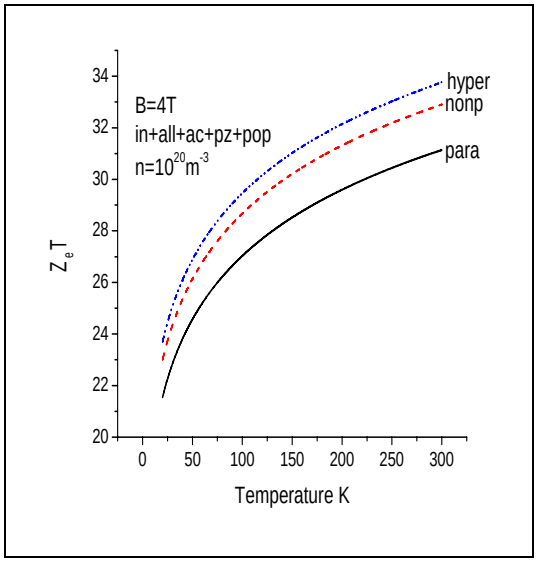

Fig. 5.27 Variation of Z_eT with temperature at constant magnetic field 4T for nondegenerate n-$Hg_{0.8}Cd_{0.2}Te$ with various scattering mechanisms such as ionized impurity (in), alloy disorder (all), acoustic phonon via deformation potential (ac), piezoelectric (pz) and polar optical phonon (pop) scattering mechanisms.

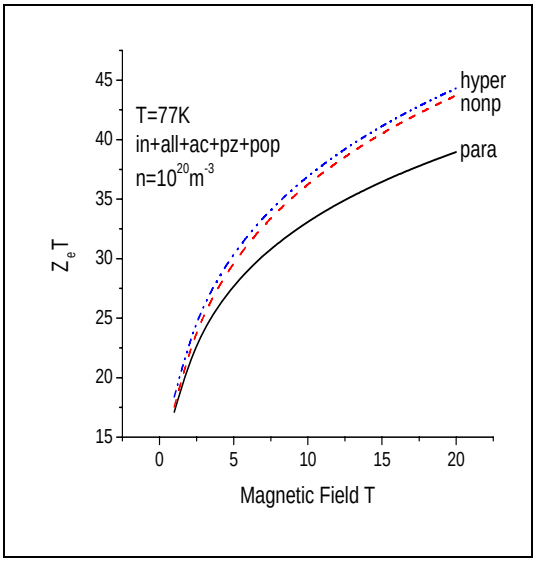

Fig. 5.28 Variation of Z_eT with magnetic field at constant temperature 77K for nondegenerate n-$Hg_{0.8}Cd_{0.2}Te$ with various scattering mechanisms such as ionized impurity (in), alloy disorder (all), acoustic phonon via deformation potential (ac) , piezoelectric (pz) and polar optical phonon (pop) scattering mechanisms.

Figs. 5.27, 5.28, 5.29, 5.30 show that the values of Z_eT increase with the increasing magnetic field and also with temperature. Z_eT is also found to be maximum for hyperbolic band structure and are followed by nonparabolic and parabolic band structures. Z_eT being a solo dependent on the square of the Seebeck coefficient in the present case, as the conductivity term cancels out due to its presence in numerator and denominator, when the electronic contribution to the thermal conductivity alone is taken. Seebeck coefficient increases with magnetic field as well as with temperature as found in Figs. 5.15, 5.16, 5.19 and 5.20. Hence, the nature of the curve for Z_eT in Figs. 5.27, 5.28, 5.29 and 5.30 is similar to Seebeck curve.

Fig. 5.31 shows the variation of ZT with temperature at a constant magnetic field 4.0T for nondegenerate MCT with lower temperature scattering mechanism such as ionized impurity (in), alloy disorder (all), acoustic phonon via deformation potential (ac) and piezoelectric (pz) scattering mechanisms. Total thermal conductivity is taken as a sum of the thermal conductivity due

to electron and the lattice. For the lattice part of the thermal conductivity the boundary scatterings due to acoustic phonon (AC) and piezoelectric (PZ) phonons are taken. Similar variation of ZT with magnetic field at a constant temperature 30K for nondegenerate MCT with all scattering mechanisms as used for Fig 5.31 is presented in Fig. 5.32.

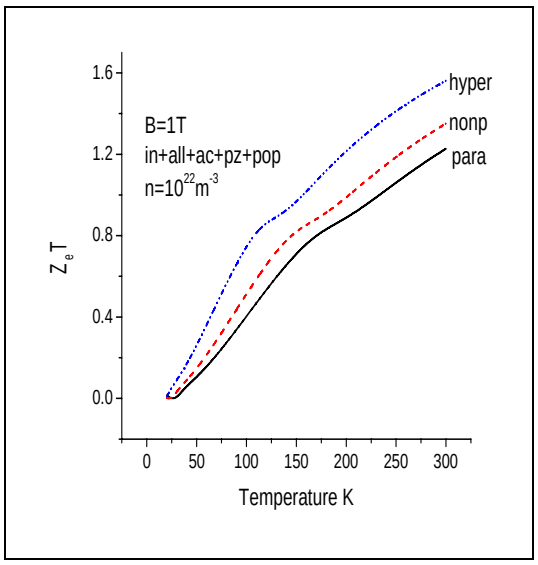

Fig. 5.29 Variation of Z_eT with temperature at constant magnetic field 1T for degenerate n-$Hg_{0.8}Cd_{0.2}Te$ with various scattering mechanisms such as ionized impurity (in), alloy disorder (all), acoustic phonon via deformation potential (ac), piezoelectric (pz) and polar optical phonon (pop) scattering mechanisms.

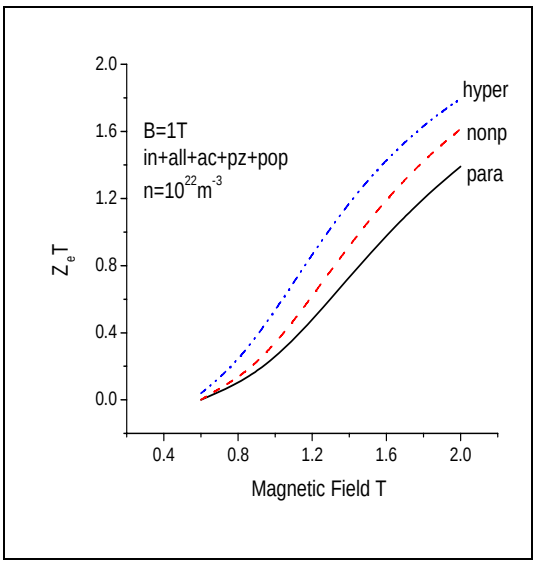

Fig. 5.30 Variation of Z_eT with magnetic field at constant temperature 77K for degenerate n-$Hg_{0.8}Cd_{0.2}Te$ with various scattering mechanisms such as ionized impurity (in), alloy disorder (all), acoustic phonon via deformation potential (ac) , piezoelectric (pz) and polar optical phonon (pop) scattering mechanisms.

Including, the polar optical phonon (pop) scattering mechanism along with all low temperature scattering mechanisms as considered for the above Figs. 5.31 and Fig.5.32, the variation of ZT is observed and is shown in Fig. 5.33. The Figs 5.33 represents the variation of ZT with temperature at a constant magnetic field 4.0T for nondegenerate MCT.

Using the various scattering mechanisms taken for plotting curve of Fig. 5.33, the variation of ZT with magnetic field at a constant temperature 77K for nondegenerate MCT is presented in Fig. 5.34.

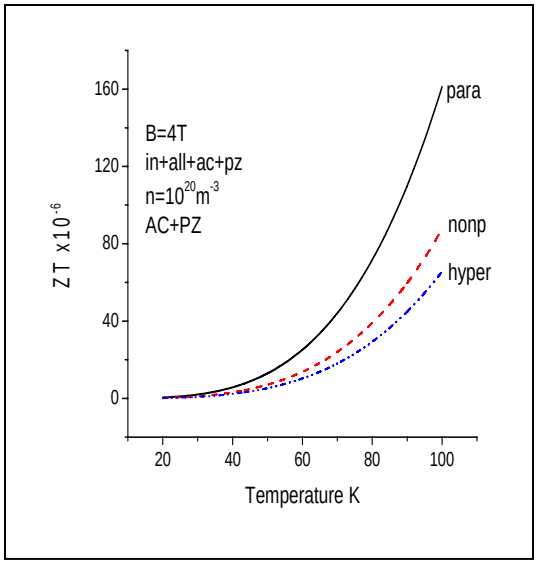

Fig. 5.31 Variation of ZT with temperature at constant magnetic field 4T for nondegenerate n-$Hg_{0.8}Cd_{0.2}Te$ with various scattering mechanisms such as ionized impurity (in), alloy disorder (all), acoustic phonon via deformation potential (ac) and piezoelectric (pz) scattering mechanisms. Boundary scatterings due to acoustic phonon (AC) and piezoelectric (PZ) are included for lattice thermal conductivity.

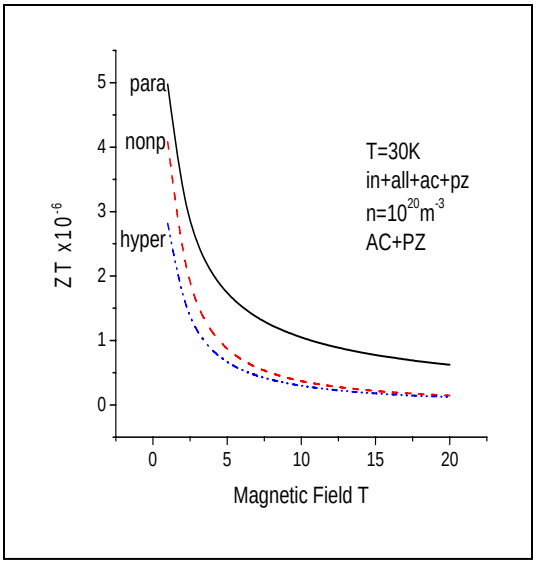

Fig. 5.32 Variation of ZT with magnetic field at constant temperature 30K for nondegenerate n-$Hg_{0.8}Cd_{0.2}Te$ with various scattering mechanisms such as ionized impurity (in), alloy disorder (all), acoustic phonon via deformation potential (ac) and piezoelectric (pz) scattering mechanisms. Boundary scatterings due to acoustic phonon (AC) and piezoelectric (PZ) are included for lattice thermal conductivity.

Figs. 5.31 and 5.33 show that the ZT increases with rise in temperature, while Figs. 5.32 and 5.34 show that the ZT decreases with rise in magnetic field, such ZT being the functions of conductivity (σ), Seebeck coefficient (S), temperature (T) and the thermal conductivity (κ). As MCT is a narrow band gap material with very low effective mass hence it has very high conductivity. ZT is dependent on σ, which decreases with temperature. The total thermal conductivity (κ) in the denominator also decreases with temperature. The magnitude of the Seebeck coefficient is in the order of meV. Hence, the overall effect causes the observed variation. Due to the conductivity being maximum for parabolic band, ZT is also maximum for the parabolic band structure and are followed by nonparabolic and hyperbolic band structures. The result of Figs. 5.32 and 5.34 can also be explained in the same way.

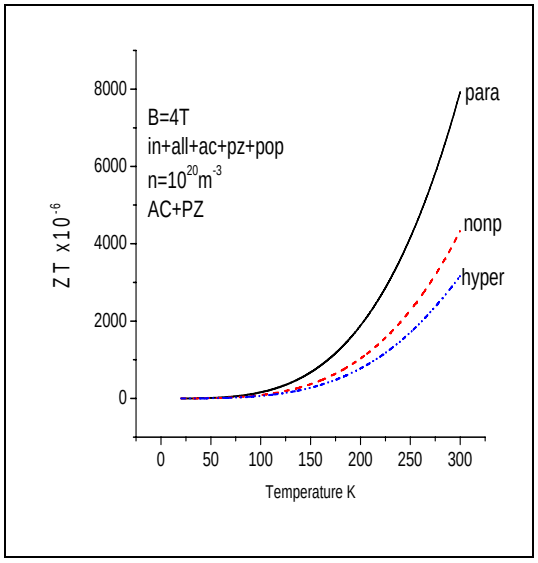

Fig. 5.33 Variation of ZT with temperature at constant magnetic field 4T for nondegenerate n-$Hg_{0.8}Cd_{0.2}Te$ with various scattering mechanisms such as ionized impurity (in), alloy disorder (all), acoustic phonon via deformation potential (ac), piezoelectric (pz) and polar optical phonon (pop) scattering mechanisms. Boundary scatterings due to acoustic phonon (AC) and piezoelectric (PZ) are included for lattice thermal conductivity.

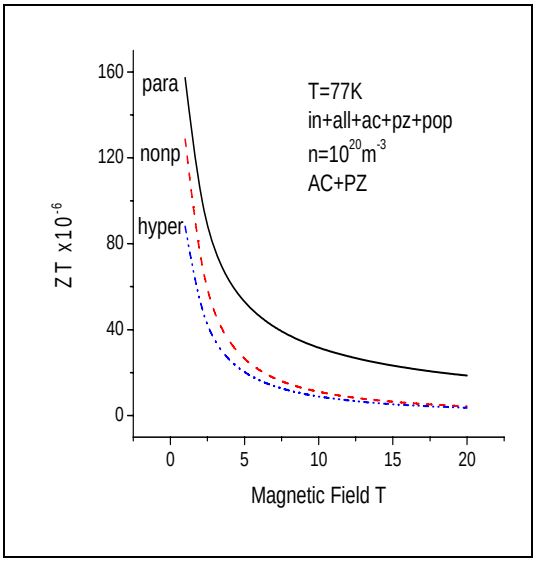

Fig. 5.34 Variation of ZT with magnetic field at constant temperature 77K for nondegenerate n-$Hg_{0.8}Cd_{0.2}Te$ with various scattering mechanisms such as ionized impurity (in), alloy disorder (all), acoustic phonon via deformation potential (ac) , piezoelectric (pz) and polar optical phonon (pop) scattering mechanisms. Boundary scatterings due to acoustic phonon (AC) and piezoelectric (PZ) are included for lattice thermal conductivity.

Fig. 5.35 shows the variation of ZT with temperature at a constant magnetic field 1.0T for degenerate MCT with ionized impurity (in), alloy disorder (all), acoustic phonon via deformation potential (ac) and piezoelectric (pz) scattering mechanisms. The lattice thermal conductivity is taken with boundary phonon scatterings due to acoustic phonon (AC) and piezoelectric phonon (PZ) scatterings.

The curve of Fig. 5.36 shows the variation of ZT with magnetic field at a constant temperature 30K for degenerate MCT with all the same scattering mechanisms considered for the curves of Fig. 5.35.

The variation of ZT with temperature is shown in Fig. 5.37 at a constant magnetic field 1.0T for degenerate MCT for low temperature scattering

mechanisms, assumed to plot Figs. 5.35 and 5.36 along with polar optical phonon (pop) scattering mechanism. Similar variation of ZT with magnetic field at a constant temperature 77K for degenerate MCT is shown in Fig 5.38 with scattering mechanisms are taken to plot Fig. 5.37.

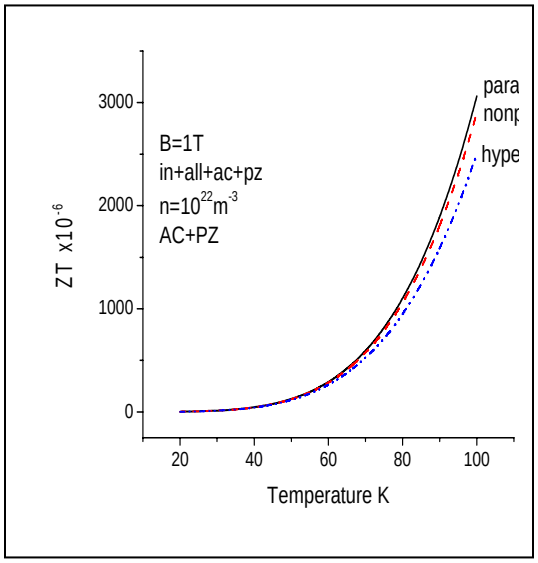

Fig. 5.35 Variation of ZT with temperature at constant magnetic field 1T for degenerate n-$Hg_{0.8}Cd_{0.2}Te$ with various scattering mechanisms such as ionized impurity (in), alloy disorder (all), acoustic phonon via deformation potential (ac) and piezoelectric (pz) scattering mechanisms. Boundary scatterings due to acoustic phonon (AC) and piezoelectric (PZ) are included for lattice thermal conductivity.

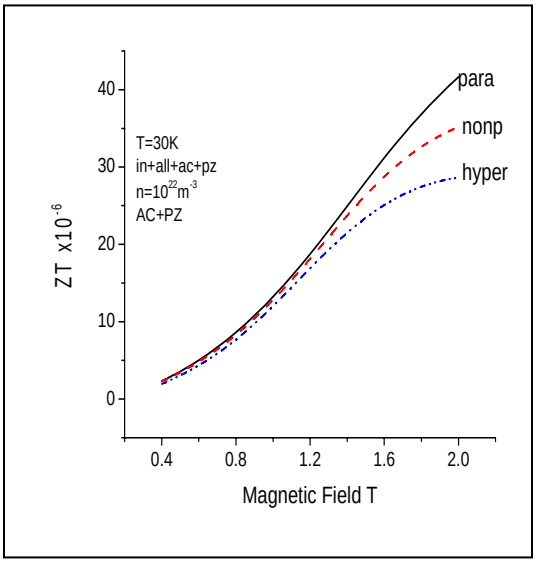

Fig. 5.36 Variation of ZT with magnetic field at constant temperature 30K for degenerate n-$Hg_{0.8}Cd_{0.2}Te$ with various scattering mechanisms such as ionized impurity (in), alloy disorder (all), acoustic phonon via deformation potential (ac) and piezoelectric (pz) scattering mechanisms. Boundary scatterings due to acoustic phonon (AC) and piezoelectric (PZ) are included for lattice thermal conductivity.

Figs. 5.36 and 5.38 show that the value of ZT increases with the increase in magnetic field. The values of ZT is found to be maximum for parabolic band structure and is followed by nonparabolic and hyperbolic band structure respectively. Here also, we can explain the result due to the magnitude of the conductivity (σ), shown in Figs. 5.6 and 5.8 respectively, being very high as compared to that of Seebeck coefficient (S), shown in Figs. 5.18 and 5.20. The thermal conductivity term in the denominator is independent of the magnetic field.

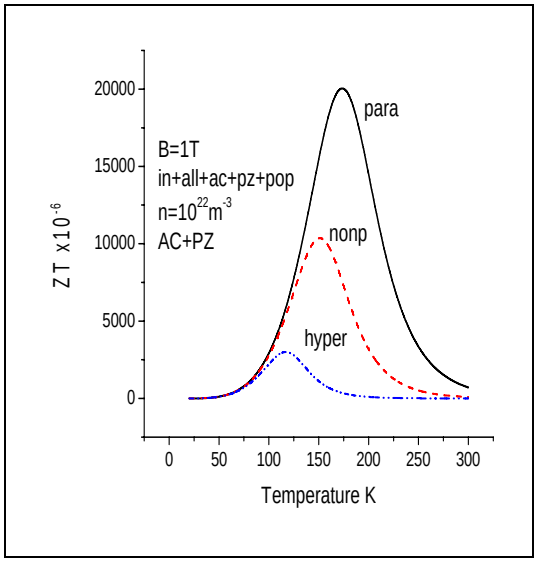

Fig. 5.37 Variation of ZT with temperature at constant magnetic field 1T for degenerate n-$Hg_{0.8}Cd_{0.2}Te$ with various scattering mechanisms such as ionized impurity (in), alloy disorder (all), acoustic phonon via deformation potential (ac), piezoelectric (pz) and polar optical phonon (pop) scattering mechanisms. Boundary scatterings due to acoustic phonon (AC) and piezoelectric (PZ) are included for lattice thermal conductivity.

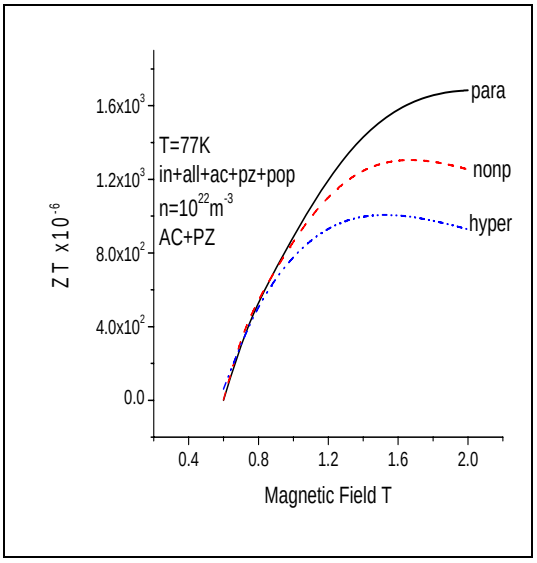

Fig. 5.38 Variation of ZT with magnetic field at constant temperature 77K for degenerate n-$Hg_{0.8}Cd_{0.2}Te$ with various scattering mechanisms such as ionized impurity (in), alloy disorder (all), acoustic phonon via deformation potential (ac) , piezoelectric (pz) and polar optical phonon (pop) scattering mechanisms. Boundary scatterings due to acoustic phonon (AC) and piezoelectric (PZ) are included for lattice thermal conductivity.

Fig. 5.37 shows a peculiar character that the ZT is found to be maximum at temperature of about 100K and decreases with temperature as expected, because the conductivity curve in Fig. 5.7 shows quite the similar character as that of the curve in Fig. 5.37.

At present, bulk bismuth telluride alloys have the highest value of Z. It is calculated that ZT=1 at room temperature [Sofo Mahan and Baars 1994]. Our studies showed the values of ZT is maximum of 0.02, .01, and .003 for degenerate MCT at temperatures 172K, 150K and 116K considering parabolic, nonparabolic and hyperbolic band structures with carrier concentration of $10^{22}m^{-3}$.

5.4 Conclusions

MCT has very high mobility due to a low effective mass. High mobility strongly supports its application in thermoelectric devices, such as refrigerator, cooler and generators. Hence, the author has selected the material.

Due to the narrow band gap, the band structure of MCT is taken as nonparabolic based on Kane's model, but later it is found to be hyperbolic band due to extreme inparabolicity of the band structure. The nonparabolicity factors for both band structures have been calculated. A relative comparison of the above band structures under magnetic quantization has been made by considering the effect on transport parameters of MCT.

In the presence of longitudinal quantizing magnetic field, the system behaves totally differently from that of the bulk system due to the quantization of the energy levels. The system under such circumstance behaves as quasi-one dimensional (Q1D). The study of various transport parameters such as mobility, Seebeck coefficient, thermal conductivity due to electrons and the figure of merit for magnetically quantized Q1D system of MCT is an important part of our work.

The thermal conductivity due to electrons, for all the band structures of MCT has also been calculated. Since the magnetic field has no effect on lattice atoms, thermal conductivity due to lattice is calculated using boundary phonon scattering mechanisms, introduced by [Puri and Geballe, 1966] taking the acoustic and piezoelectric phonon scatterings.

The variations of the above transport parameters with temperature and magnetic field have been observed with the hyperbolic band structure. The values and the nature of the transport parameter variations are found to be close to the available theoretical and experimental data.

We have also observed the effect of degeneracy on the system, which arises due to the higher carrier concentrations, electron distribution in such condition is taken to be Fermi-Dirac distribution.

The effect of low temperature scattering mechanisms such as ionized impurity (in), alloy disorder (all), acoustic phonon via deformation potential (ac) and piezoelectric (pz) scattering mechanisms and the higher

temperature scattering mechanism such as polar optical phonon (pop) scattering of MCT on the above transport parameters have been investigated.

References

Aliev M.I., Askerov B.M., Agaeva R.G., Daibov A.Z. and Ismailov I.A., Sov. Phys. Semicond. 9, 377 (1975).

Arora V.K. and Jaafarian M., Phys. Rev B 13, 4457 (1976).

Arora V.K. and Spector H.N., Phys. Stat. Sol. (b) 94, 323 (1979).

Baars J., Brink D., Edwall D.D. and Bubulac L.O., J. Electron. Mater 22, 923 (1993).

Banerje, Ph. D. Thesis, Electronic transport in semiconductors under energy band quantization, Jadavpur Univerity (1995).

Basu P.K., Sarkar C.K. and Chattopadhyay D., J Appl. Phys. 64, 4041 (1988).

Blakemore I.S., Semiconductor Statistics, Dover Publication, Pergamon Press, New York, (1987).

Callaway J., Phys. Rev. 113, 1046 (1959).

Chen A.B. and Sher A., J. Vac. Sci. Technol. 21, 138 (1982).

Chattopadhya D. and Nag B.R., J. Phys. C 9, 3095 (1975).

Dornhaus R. and Nimtz G., Springer Tracts in Mod. Phys. 98, 119 (1983).

Egli P.Ed., Thermoelectricity (Wiley, New York) (1961).

Ghose M., Chakraborty C., Benerji P. and Sarkar C.K., Indian J. Phys. 74A (4), 399 (2000).

Goldsmid H.J., Electronic Refrigeration, [London: Pion Limited] (1986).

Harmon T.C. and Honig J.M., J. Appl. Phys. 33, 3178 (1962).

Huff H.R., Kawaji S. and Gatos H.C., Phys. Stat. Sol. (b) 30, 613 (1968).

Krishnamurthy S. and Sher A., J. Appl. Phys. 7904 (1994).

Krishnamurthy S. and Sher A., J. Elec. Mater. 24 641 1121 (1995).

Kubakaddi S.S., Mulimani B. G. , J. Appl. Phys. 58, 3643 (1985).

Nag B.R., Electron Transport in Compound Semiconductors Vol. II, edited by H.J. Queisser (Springer Berlin) (1980).

Nimtz G. and Gebhardt J., Proc. of the 18th International Conference on the Physhics of Semiconductors, Stockhom, 1986, ed. by O. Engstrom (World Scientific, Singapore), 1197 (1987).

Phadke U.P. and Sharma S., J. Phys. Chem. Sol. 36, 1 (1975).

Puri S.M. and Geballe T.H., in Semiconductors and Semimetals, ed. by R.K. Willardson and A.C. Beer (Academic, New York), Vol.1, 203-264 (1966).

Rowe D.M. and Bhandari C.M., Modern Thermoelectrics (Reston, Reston VA), (1983).

Santra K., Ph. D. Thesis, Some studied on electron transport parameters of narrow gap semiconductors under magnetic quantization, Jadavpur University (1994).

Santra K., Shrestha S. Sarkar C.K. and Bhattarai P.K., Proc. of XIth

International Workshop on the Physics of Semiconductor Devices IWPSD 2001, held at IIT, Delhi, from Dec.11 to 15, pg.1367 (2001).
Shakouri Ali and Chris LaBounty, Pro, of Int. Conf, on Thermoelec, Baltimore, Sept. (1999).
Smith R.A., Semiconductors, Academic Publishers, IInd edition (1989).
Sofo J.O., J. Appl. Phys. 77, 1561, (1995).
Sofo J.O. and Mahan G.D., Phys. Rev. B 49, 4565 (1994).
Sofo J.O., Mahan G.D and Baars J., J. Appl. Phys. 76, 2249 (1994).
Stadler J.P. and Nimtz G., Phys. Rev. Lett. 56, 382 (1986).
Wu C.C. and Spector H.N., Phys. Rev. B 3, 3979 (1971).

Parameters of n-$Hg_{0.8}Cd_{0.2}Te$: Table 5.1

Quantity	Magnitude	Units	References
Mole fraction x	0.8		Dornhaus and Nimtz, 1983
Debye temperature T_D	300	K	Stadler and Nimtz, 1986
Free space permittivity ε_0	8.85418×10^{12}	F/m	Nag, 1980
ε_∞	$12.76\varepsilon_0$	F/m	Dornhaus and Nimtz, 1983
Dielectric constant ε	$18\varepsilon_0$	F/m	Dornhaus and Nimtz, 1983
Lande's factor $\lvert g\rvert$	90 (4T)		Dornhaus and Nimtz, 1983
Effective mass $m^*(4K)$	$0.0065\left(9.109\times10^{-31}\right)$	Kg	Dornhaus and Nimtz, 1983
Deformation potential constant E_1	9	eV	Dornhaus and Nimtz, 1983
Piezoelectric modulus e_{14}	0.0355	Cm^{-2}	Santra, 1994
No of atoms per unit volume N_A	$3.68x10^{27}$	m^{-3}	Santra, 1994
Alloy scattering potential E_o	1.9	eV	Dornhaus and Nimtz, 1983
Mass density ρ	7654.0	Kgm^{-3}	Dornhaus and Nimtz, 1983
Ionized impurity concentration n_i	10^{20} for nondeg 10^{22} for deg	m^{-3} m^{-3}	Santra, 1994
Acoustic sound velocity u_{ac}	3017	ms^{-1}	Dornhaus and Nimtz, 1983
Piezoelectric sound velocity u_{pz}	1948	ms^{-1}	Dornhaus and Nimtz, 1983
γ	$48.3x10^{-18}$	$(eVm)^2$	Krishanmurthy and Sher, 1994
c	.056	eV	Krishanmurthy and Sher, 1994
Bandgap energy E_g	70	meV	Dornhaus and Nimtz, 1983

References for Parameters

Dornhaus R. and Nimtz G., Springer Tracts in Mod. Phys. 98, 119 (1983).

Krishnamurthy S. and Sher A., J. Appl. Phys. 75, 7904 (1994).

Santra K., Ph. D. Thesis, Some studied on electron transport parameters of narrow gap semiconductors under magnetic quantization, Jadavpur University (1994).

Stadler J.P. and Nimtz G., Phys. Rev. Lett. 56, 382 (1986).

Nag B.R., Electron Transport in Compound Semiconductors Vol. II, ed. by H.J. Queisser (Springer Berlin) (1980).

Appendix 5A

The hyperbolic relation (equation 5.4) is,

$$E^h = \left(\gamma k^2 + c^2\right)^{1/2} - c$$

where, $k^2 = \left(n + \frac{1}{2}\right)\frac{2Be}{\hbar} + k_z^2$

Hence, $E^h = \left(\gamma\left\{\left(n + \frac{1}{2}\right)\frac{2Be}{\hbar} + k_z^2\right\} + c^2\right)^{1/2} - c$

$$E^h = \left[k_z^2\gamma + \left(n + \frac{1}{2}\right)\frac{2Be\gamma}{\hbar} + c^2\right]^{1/2} - c$$

$$= \sqrt{\left(n + \frac{1}{2}\right)\frac{2Be\gamma}{\hbar} + c^2} \quad \times\left[1 + \frac{k_z^2\gamma}{\left\{\left(n + \frac{1}{2}\right)\frac{2Be\gamma}{\hbar} + c^2\right\}}\right]^{1/2} - c$$

$$= \sqrt{\left(n + \frac{1}{2}\right)\frac{2Be\gamma}{\hbar} + c^2} \quad \times\left[1 + \frac{k_z^2\hbar^2}{2m^*\left\{\left(n + \frac{1}{2}\right)\frac{2Be\gamma}{\hbar} + c^2\right\}\frac{\hbar^2}{2m^*\gamma}}\right]^{1/2} - c$$

Let, $x = \left(n + \frac{1}{2}\right)\frac{2Be\gamma}{\hbar} + c^2$ and $y = \left\{\left(n + \frac{1}{2}\right)\frac{2Be\gamma}{\hbar} + c^2\right\}\frac{\hbar^2}{2m^*\gamma}$

$$E^h = \sqrt{x}\left[1+\frac{1}{2}\times\frac{k_z^2\hbar^2}{2m^* y}+.....\right]-c$$

$$=\left[\frac{k_z^2\hbar^2}{2m^*\left(2y/\sqrt{x}\right)}+.\sqrt{x}\right]-c$$

$$=\frac{k_z^2\hbar^2}{2m^* a_o^h}+\sqrt{\left(n+\frac{1}{2}\right)\frac{2Be\gamma}{\hbar}+c^2}-c$$

Hence, the nonparabolicity factor for hyperbolic band structure be,

$$a_o^h = 2\sqrt{\left\{\left(n+\frac{1}{2}\right)\frac{2Be\gamma}{\hbar}+c^2\right\}}\times\frac{\hbar^2}{2m^*\gamma}$$

Appendix 5B

Fermi Energy $E_{F1}(H)$ for nondegenerate Semiconductors [Nag 1980] in the extreme quantum limit,

For parabolic band structure,

$$\eta^P = \frac{E_{F1}(H)}{k_B T} =$$

$$= Ln\left[\frac{n_e k_B T}{2\hbar\omega}\left(\frac{2\pi\hbar^2}{m^* k_B T}\right)^{3/2}\exp\left(\frac{\hbar\omega}{2k_B T}\left(1-\frac{m^*}{2m}\right)\right)\right]...(5B.1)$$

For nonparabolic band structure,

$$\eta^{np} = Ln\left[\frac{n_e k_B T}{2\hbar\omega}\left(\frac{2\pi\hbar^2}{m^* k_B T}\right)^{3/2}\frac{\exp\left(\frac{E_g}{2k_B T}(a_0-1)\right)}{a_0^{1/2}}\right]...(5B.2)$$

For hyperbolic band structure,

$$\eta^h = Ln\left[\frac{n_e k_B T}{2\hbar\omega}\left(\frac{2\pi\hbar^2}{m^* k_B T}\right)^{3/2}\frac{\exp\left(\sqrt{\frac{Be\gamma}{\hbar}+c^2}-c\right)}{\sqrt{a_o^h}}\right]...(5B.3)$$

Fermi Energy $F_{F2}(B)$ for degenerate Semiconductors [Arora and Jaafrian 1976] in the extreme quantum limit,

For parabolic band structures,

$$\eta^{p} = \frac{E_{F2}(H)}{k_B T} = \frac{\pi n_e^2}{4N_c^2\theta^2} + \left(1 - |g|\frac{m^*}{2m_0}\right)\frac{\hbar\omega}{2}$$

...(5B.4)

For nonparabolic band structures,

$$\eta^{np} = \frac{E_F}{k_B T} = \frac{\pi n_e^2}{4N_c^2\theta^2 a_0} + \frac{E_g(a_0 - 1)}{2k_B T}$$

...(5B.5)

For hyperbolic band structures,

$$\eta^{h} = \frac{E_F}{k_B T} = \frac{\pi n_e^2}{4N_c^2\theta^2 a_o^h} + \sqrt{\frac{Be\gamma}{\hbar} + c^2} - c$$

...(5B.6)

where $\theta = \dfrac{\hbar\omega}{k_B T}$

Appendix 5C

τ_{ac}, τ_{pz},τ_{imp}, τ_{alloy} and τ_{pop} are the relaxation time for acoustic, piezoelectric, ionized impurity, alloy disorder and polar optical phonon scattering [Phadke and Sharma 1975; Arora V.K. and Spector 1979; Arora V.K. and Jaafrian 1976] respectively.

$$\tau_{ac}^{-1} = \frac{C_{ac}(m^* a_o)^{1/2}}{2\sqrt{\pi}\hbar^2 l^3} F_{ac}\left[\frac{N_q}{\sqrt{E + \hbar\omega_{ac}}} + \frac{N_q + 1}{\sqrt{E - \hbar\omega_{ac}}}\right] ..(5C.1)$$

$$\tau_{pz}^{-1} = \frac{C_{pz}(m^* a_o)^{1/2}}{2\sqrt{\pi}\hbar^2 l} F_{pz}\left[\frac{N_q}{\sqrt{E + \hbar\omega_{pz}}} + \frac{N_q + 1}{\sqrt{E - \hbar\omega_{pz}}}\right] ..(5C.2)$$

$$\tau_{imp}^{-1} = \frac{n_i e^4}{4\pi(2m^* a_o)^{1/2}\varepsilon^2\varepsilon_o^2 E^{1/2}(\varepsilon_d + 4E)} ..(5C.3)$$

$$\tau_{alloy}^{-1} = \frac{C_{alloy}}{2\pi\hbar^2 l^2}\left(\frac{1+\beta}{1+\beta+\alpha_s}\right)^{1/2}(2m^* a_o)^{1/2}\frac{1}{\sqrt{E}} ...(5C.4)$$

$$\tau_{pop}^{-1} = \frac{1}{2}\left[\left(1+\frac{\alpha}{2}\right)e^{x\theta}.E_1(x\theta) - \frac{\alpha}{2x\theta}\right] \times \frac{1}{h}\left(\frac{m^* a_o}{2\hbar^2}\right)^{1/2}$$
$$\times C_{pop}\left[\frac{N_q}{\sqrt{E+\hbar\omega_q}} + \frac{N_q+1}{\sqrt{E-\hbar\omega_q}}\right] \ldots (5C.5)$$

Where,

$$C_{ac} = \frac{E_1^2}{2u_{ac}\rho}$$

$$C_{pz} = \frac{\hbar^2 e^2 e_{14}^2}{2u_p(\varepsilon_s\varepsilon_o)^2\rho}$$

$$C_{imp} = \frac{n_i e^4}{(\varepsilon_s\varepsilon_o)^2}$$

$$C_{alloy} = \frac{3\pi^2 x'(1-x')E_o^2}{16N_A}$$

Matthiessen's rule.

$$\tau_{toral}^{-1} = \tau_{ac}^{-1} + \tau_{pz}^{-1} + \tau_{imp}^{-1} + \tau_{alloy}^{-1} + \tau_{pop}^{-1}$$

Magnetic field dependent Seebeck Coefficient

$$S(H) = \frac{\xi}{\nabla_z T} = -\frac{k_B}{e}\left[-\frac{E_F(H)}{k_B T} + \frac{\int \frac{E_{oz}}{k_B T}\tau_o(E_{oz})\frac{\partial g_o(E_{oz})}{\partial E_{oz}}k_z^2 dk_z}{\int \tau_o(E_{oz})\frac{\partial g_o(E_{oz})}{\partial E_{oz}}k_z^2 dk_z}\right]$$

6.1 Introduction

Low Dimensional Devices (LDD) and their interesting physical properties based on quasi-two dimensional (Q2D) semiconductor systems have been investigated for long time. Further reduction in the dimension of the system is in progress because of their advantage to study physical properties of the material and also to invent new low dimensional devices with very high efficiency, such as quantum effect devices, single electron devices, quantum interference devices for the recent VLSI technology etc.

A strong magnetic field applied to a bulk semiconductor leads to the formation of a set of equally spaced energy levels on a plane perpendicular to the applied magnetic field. The equally spaced or quantized circular energy levels are called Landau levels [Landau, 1930], having quantized energy eigen values. Under such a condition the motion of the carriers is restricted on the surface transverse to the direction of the magnetic field. However, the carriers are still free to move along the direction of the field. Such the system behaves as a quasi-one dimensional (Q1D) system.

A very high magnetic field causes the carriers to confine to the innermost cylinder, which is called the Extreme Quantum Limit (EQL). In such case electrons are available only in the lowest Landau level. We have already discussed it in detail in **Chapter V**.

In the present case, we have taken an ultra thin film of semiconductor having thickness of the order of deBroglie wavelength and applied a strong magnetic field along the direction of the thickness of the film. It creates a set of Landau levels as mentioned before on the surface of the film, at the mean time the motion along the film is also restricted due to the Quantum Sized Effect (QSE) [Majumdarm, Maity and Chakravarti, 1987]. Such a system provides a unique quantum-zero dimensional (Q0D) system where motion of electrons in all three directions is quantized.

Similar sub-dimensional systems can be formed by the conventional geometrical confined system also. Modern growth techniques such as molecular beam epitaxy (MBE) or metal organic chemical vapor deposition (MOCVD) [Ploog, 1980] made possible to fabricate devices of desired size and shape. Considering the devices of geometrical dimensions equal to that of magnetically confined structures, a comparative study has been done in such quantum well wire (QWW) and quantum dot (QD).

In the system such as QWW, higher carrier confinement causes enhanced mobility due to the confinement of the energy levels in various directions. The obvious potential of such type of systems is small and are useful for ultrafast devices in the field of ultra large scale integration (ULSI) and optical communications.

Due to the quantization of energy band structures the density of states (DOS) of the systems also is modified as we have seen in our review sections **Chapter II**. DOS for Q1D and Q0D possesses very sharp singular structures [Arch, 1985]. These structures appear through the step like nature in various optical and electronic transport parameters. However, in practice due to the presence of impurities or some imperfections the DOS instead of showing sharp nature is modified and there will be the broadening of the quantized energy levels. Hence, in order to observe the effect of such broadened energy levels due to electrons-impurities interaction the modified DOS has to be taken into consideration, while investigating the optical processes from real quantum-low dimensional (QLD) systems [Roth and Argyres, 1966].

The photoemission analysis, which is a useful tool to investigate the energy level structures for a semiconductor system, has been presented here. The photoemission (PE) current density due to magnetically quantized systems of Q1D and Q0D systems, formed by QSE is calculated. PE current density in the geometrically confined structure of physical dimension, same as that of the magnetically confined structure has also been studied. The calculations for Q1D system is done considering the radius of the QWW, due to geometrical confinement is equal to the radius of the lowest Landau subband under EQL. Similarly, the radius of QDs, formed by geometrical confinement also has been taken to be equal to the radius of Landau level with EQL consideration for Q0D calculations.

Furthermore, a comparison of the above systems has been made considering the lowest energy level for these systems to be same.

Due to the presence of impurities and imperfections in real system the motion of electrons giving rise to broadened energy levels, otherwise sharp and consequently modifies the DOS also. To study the photoemission process from such broadened energy levels the infinite well consideration is used in the present context to simplify the model. The basic understanding of the effect of broadening on the energy levels based on the infinite QWW model

will not much differ from those obtained from finite QWW model. Finally, a comparative study of the effect of energy level broadening on photoelectric emission due to the imperfection in such sub-two dimensional systems has been done.

6.2 Theoretical Model

When a shower of monochromatic photons of energy $h\upsilon$ is incident along the z-direction, the emission of photoelectrons is considered to take place along the same direction. Considering the incident photons are assumed to have energy sufficient to emit conduction electrons only. The current density (J) is used to estimate contribution from individual electric subbands [Majhumdar et al., 1987] is given by,

$$J = \sum \Delta J = \sum \frac{1}{2} aev\Delta n_0 \qquad ...(6.1)$$

where a is the photon absorption coefficient, e is the electronic charge and the factor $(1/2)$ takes into account the fact that statically only half the photo excited electrons capable of escaping are reflected back into the sample. ν and Δn_o are the velocity of the carries in the different subbands and the volume density respectively.

6.2 (a) i. Magnetically Confined System (MCS)

Q1D

When a bulk wide band gap semiconductor is subjected to a strong external magnetic field, the energy dispersion relation can be written as,

$$E = \left(n + \frac{1}{2} \right) \hbar\omega_o + E_x \qquad ...(6.2)$$

Where, n is the magnetic quantum number. $n = 0,1,2,3,4.....$ means that each value of the number gives the radius of the concentric circles. $\omega_o = Be/m^*$, is the cyclotron frequency. The magnetic flux density (B) is applied along x-axis. m^* and $\hbar$ are effective mass and Plank's constant divided by 2π respectively. The 1st term in the equation (6.2) represents the motion on the yz-plane. The motion is restricted due to the quantization of energy levels. The 2nd term, $E_x = \hbar^2 k_x^2 / 2m^*$ is energy of carriers in the

direction of z-axis, where carriers are still able to move freely. Hence the whole system behaves like Q1D system.

In the case of a very high magnetic field only the innermost Landau level is occupied by electrons. Hence, $n = 0$ is the only occupied level and the condition is called extreme quantum limit (EQL).

The radii of curvatures of the quantized levels on the xy-plane, the Landau levels are given as,

$$R = \sqrt{\hbar \Big/ 2\left(n + \frac{1}{2}\right)Be} \qquad ...(6.3)$$

In magnetically confined QWW the volume density of carriers in the quantized energy level (E_n) is,

$$D(E) = \frac{1}{(2\pi l)^2}\left(\frac{2m^*}{\hbar^2}\right)^{1/2} \sum_n \left[E - \left(n + \tfrac{1}{2}\right)\hbar\omega_o\right]^{1/2} \qquad ...(6.4)$$

$$\Delta n_o = 4\pi\hbar\omega_o \left(\frac{2m^*}{h^2}\right)^{3/2} \sqrt{E_F - E_n} \qquad ...(6.5)$$

assuming very low temperature, so the Fermi distribution function $f(E) = 1$ can be retained.

Substituting the values of Δn_o into the equation (6.1) we can obtain the photoelectric current density due to magnetically confined QWW. Since only the subband lying below the Fermi level will participate in emission, $n_{\max}$ will be limited as $E_{\max} \le E_F$ [Majumdar, Maity and Chakravarti, 1987]. Similarly v in the equation (6.1) is substituted by v_s, where $v_s = \sqrt{\left(2E_s / m^*\right)}$, is the corresponding velocity in the subband having E_s subband energy.

Q0D

Now, an ultrathin film of thickness *d* (~ nm) is assumed to be subjected to a strong magnetic field *B*, applied normal to the film surface, i.e., along *z*-direction. The continuous energy spectrum in *xy*-plane is then spited into discrete Landau levels. The z-direction also gets quantized due to the size

quantization. The energy dispersion relation for the carriers under the circumstance can be expressed as [Das et al., 2004],

$$E_{np} = \left(n + \frac{1}{2}\right)\hbar\omega_o + \frac{\hbar^2}{2m_n^*}\left(\frac{p\pi}{d}\right)^2 \quad ...(6.6)$$

The 1st term in the equation (6.6) gives the quantized levels due to the magnetic field and the 2nd term is also the quantized energy but it is due to QSE. Here, d and p ($p = 1,2,3,4....$) are the thickness of the film, which is of the order of the electron wavelength in the direction of x-axis and the size quantization number respectively. Hence the whole system behaves as Q0D.

For a particular value of *l*, the resulting DOS for an ideal system consists of a set of δ-functions separated by $\hbar\omega_0$, which is given by,

$$D(E, B) = \frac{eB}{h}\sum_{n=1}^{\infty}\delta(E - E_{nl}) \quad (6.7)$$

The degeneracy factor *eB/h* is the number of states per unit area within a single Landau level.

In the case of magnetically confined Q0D system, the volume density of carriers in the quantized energy level $(E_n)$is,

$$\Delta n_o = 4\pi\hbar\omega_0\left(\frac{2m_n^*}{h^2}\right)^{1/2}\left[\left\{E_F - \left(n + \frac{1}{2}\right)\hbar\omega_o\right\}^{1/2} + \sqrt{\frac{\hbar^2}{2m_n^*}}\left(\frac{p\pi}{d}\right)\right] \quad ..(6.8)$$

(J) for QD due to magnetically confined system becomes,

$$J = \sum\Delta J = \sum_p \sum_n \frac{1}{2} aev\Delta n_0 \quad ...(6.9)$$

6.2 (a) ii. Geometrically Confined System (GCS)

Q1D

The $E - k$ relation for geometrically confined system is given as,

$$E = E_{ml} + E_x \qquad ...(6.10)$$

The 1st term in the equation (6.10) gives the quantized energy relation [Arora and Prasad, 1983] and is given as,

$$E_{ml} = \frac{\hbar^2}{2m_n^*}\left(\frac{\alpha_{ml}}{R}\right)^2 \qquad ...(6.11)$$

where α_{ml} is the l^{th} zero of the m^{th} order Bessel function of first kind, and R is the radius of the circular corss-section of the QWW. The 2nd term in the equation (6.10) E_x gives the free energy part along the length (x-direction) of the wire.

In order to develop a model to estimate the PE current from realistic Q1D structure, a cylindrical wire of radius *R* (~ nm) having cross-section on *yz* plane with length measured along *x*-direction has been considered. The photons are assumed to be incident on the wire radialy along *z*-direction. The energy of electrons of such structures will be continuous along *x*-direction, and discrete in the transverse plane, i.e. *yz* due to spatial quantization in the plane. This would result in the formation of electric subbands characterized by different quantum numbers.

The general expression for the photoelectric current density in the case of cylindrical Q1D is given by,

$$J = \sum_{m=1}^{m_{\max}} \sum_{l_{\min}}^{l_{\max}} J_{ml}$$

$$= \sum_{m=1}^{m_{\max}} \sum_{l_{\min}}^{l_{\max}} \frac{1}{2} aev_{lm} \Delta n_0 \qquad ...(6.12)$$

Where the volume density of carriers (Δn_o) for quantized energy levels with quantum number m and l becomes,

$$\Delta n_0 = 2\frac{\sqrt{2m^* k_B T}}{h\pi R^2} F_{-\frac{1}{2}}(\eta_{ml}) \qquad ...(6.13)$$

In the equation (6.13), $F_j(\eta_{ml})$ is the Fermi-Dirac integration of the order 'j' as defined [Blackmore, 1962] with $\eta_{ml} = \frac{(E_F - E_{ml})}{k_B T}$.

The velocity of electrons of energy E_{ml}, in equation (6.12) is given as, $v_{ml} = \frac{\hbar}{m^*}\frac{\alpha_{ml}}{R}$ .The current density due to the geometrically confined Q1D system is,

The limiting values of the quantum numbers *l* and *m*, i.e. l_{max}, l_{min} and m_{max} in the equation (6.12) are determined from the following expressions,

$E_{m_{\max}} \le E_F - E_l$, for *l*=0;

$E_{l_{\max}} \le E_F - E_m$, for *m*=1 and

$E_{l_{\min}m} \ge W - h\nu$, for *m*=1.

Where, W being the electron affinity of the material.

Q0D

The quantization in one more direction causes the energy dispersion relation to be modified. Hence the $E-k$ relation for cylindrical **Q0D** of radius R and the thickness d is,

$$E_{ml} = \frac{\hbar^2}{2m_n^*}\left(\frac{\alpha_{ml}}{R}\right)^2 + \frac{\hbar^2}{2m_n^*}\left(\frac{p\pi}{d}\right)^2 \qquad ...(6.14)$$

The volume density of carriers for each sub band then becomes,

$$\Delta n_o = \frac{2}{\pi R^2 d}\frac{1}{1+e\left(\frac{E_{mlp}-E_F}{k_B T}\right)} \qquad ....(6.15)$$

$$J = \sum_p \sum_m \sum_l \frac{1}{2} aev_{ml}\Delta n_0 \qquad ...(6.16)$$

Assuming, a very low temperature so that the Fermi distribution function can be retained, the velocity of electrons in a particular energy level is calculated from the KE.

6.2 (b) Effect of Broadening

Till now, we have dealt with ideal systems. In reality, the system is full of imperfections such as impurities and phonons in the solid. The imperfections

affect the motion of the electrons in variety of ways, which we can classify as scattering, broadening and energy shifting. Scattering is obviously most important for the transport phenomena. A theoretical model to estimate the effect of imperfections on PE current density is the subject of our concern. The energy shifting and broadening of the unperturbed energy levels are usually small for most equilibrium properties. However, the broadening of the unperturbed energy levels is quite important for the amplitudes of the oscillations for the magnetic susceptibility for metals and semimetals. They are also proved to be of importance for the oscillations and the magnetic field dependence in the quantum limit of the optical transport properties.

It has been found that the infinite DOS at the discontinuity, that the magnetic field brings about, is rounded over due to the presence of impurities. The discontinuity has been removed by introducing energy level broadening (Δ) due to electron-impurity interactions. Accordingly, the ground oscillator level $E^{-½}$ in the unperturbed DOS is to be replaced by [Roth and Argyres, 1966],

$$\left[\left(\frac{E_x + \sqrt{E_x^2 + \Delta^2}}{2\left(E_x^2 + \Delta^2\right)}\right)\right]^{\frac{1}{2}} \qquad (6.17)$$

Assuming that the magnetic field is applied along *x*-direction. For $E_x >> \Delta$, the level density coincides with unperturbed one and has finite value $(2\Delta)^{-½}$ at $E_x = 0$, and goes to 0 as $E_x \rightarrow \infty$. Due to the broadening factor originated from the presence of impurities, the Fermi level decreases. The reduced Fermi level is expressed as:

$$E_f = E_F - \frac{\Delta^2}{4E_F} \qquad ...(6.18)$$

Here, E_f is the reduced Fermi energy level, Δ is the energy level broadening width, and E_F is the Fermi level for ideal crystal, which is taken 0.15 eV in the present work.

As the Fermi level decreases, it is expected that the PE current density will also decrease as it depends on $(E_F - E_{ml})^{½}$. If such a system be further subjected to a monochromatic photon beam incident along the direction of magnetic field, the PE current density expression takes the different form.

6.2 (b) i. Effect of Broadening on MCS

Considering Landau level broadening, the DOS of the Q2DEG in the presence of a quantizing magnetic field can be expressed as a sum of Gaussian peaks [Ando et al., 1982] as,

$$D(E) = \frac{2}{2\pi L^2}\sum_n \left(\frac{2}{\pi}\right)^{\frac{1}{2}} \frac{1}{\Delta}\exp\left[-2\left(\frac{E - E_n}{\Delta}\right)^2\right] \qquad (6.19)$$

where $L = \left(\hbar/eB\right)^{1/2}$ and Δ is the broadening parameter (level width taken to be 2Δ).

Assume the degenerate statistics at low temperatures, equation (6.7) can be converted to the following form,

$$\begin{aligned} J &= \frac{ae^2B}{m^* d^2\sqrt{2\pi}}\sum_l \sum_n l \int_0^{E_F - E_l} \frac{1}{\Delta}\exp\left[-2\left(\frac{E - E_n}{\Delta}\right)^2\right]dE \\ &= \frac{ae^2B}{m^* d^2\sqrt{\pi}}\sum_l \sum_n l \int_{-u_2}^{u_1} \exp\left(-u^2\right)dE \end{aligned} \qquad ..(6.20)$$

where $u = \sqrt{2}\left(\frac{E - E_n}{\Delta}\right)$, $u_1 = \sqrt{2}\left(\frac{E_F - E_1 - E_n}{\Delta}\right)$ and $u_2 = \frac{\sqrt{2}E_n}{\Delta}$,

The expression for the current density is finally obtained as,

$$J = \frac{ae^2B}{4m^* d^2}\sum_{l=1}^{\infty}\sum_{n=n_{nim}}^{\infty} l\left\{erf\left(u_1\right) + erf\left(u_2\right)\right\} \qquad ...(6.21)$$

where, n_{min} the limiting value of the quantum number *n* is determined from the condition for escape of a confined electron as a photoelectron coming out of the QW.

However, in the limit $\Delta \to 0$ the equation (6.) takes the form,

$$J = \frac{ae^2B}{2m^* d^2}\sum_l \sum_n l$$

The value of the applied magnetic field is so chosen that the radius of the lowest Landau orbit be equal to the radius of the cylindrical QWW considered.

6.2 (b) ii. Effect of Broadening on GCS

On inclusion of broadening in DOS, the conventional Fermi-Dirac integral $F_{-½}(\eta)$ is to be replaced by $F_{-½}(\eta, \gamma)$, which is given as [Jog and Wallace, 1975],

$$F_{-\frac{1}{2}}(\eta,\gamma)=\frac{1}{(j+1)}\int\frac{\sqrt{x+i\gamma}}{[1+\exp(x-\eta_{ml})]}dx \qquad (6.22)$$

where $x=\frac{E_x}{k_BT}$ and $\gamma=\frac{\Delta}{k_BT}$.

The value of $F_{-½}(\eta, \gamma)$ changes to the conventional Fermi-Dirac integral in the no broadening limit. One may write $F_{-½}(\eta, \gamma)$ in the asymptotic form for the extreme degeneracy.

6.3 Results and Discussions

The material parameters to calculate the magnetically and geometrically confinement studies for GaAs are taken from Adachi [Adachi, 1985]. The effect of nonparabolicity has not been considered due to the wide band gap of GaAs material.

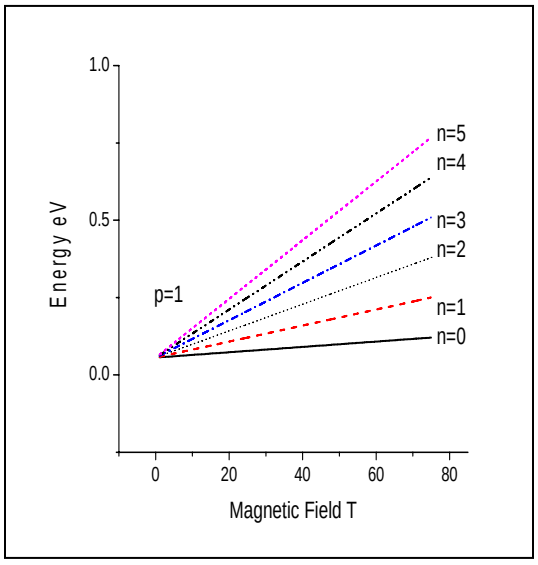

Fig. 6.1 Variation of energy versus magnetic field for different values of Landau levels (n).

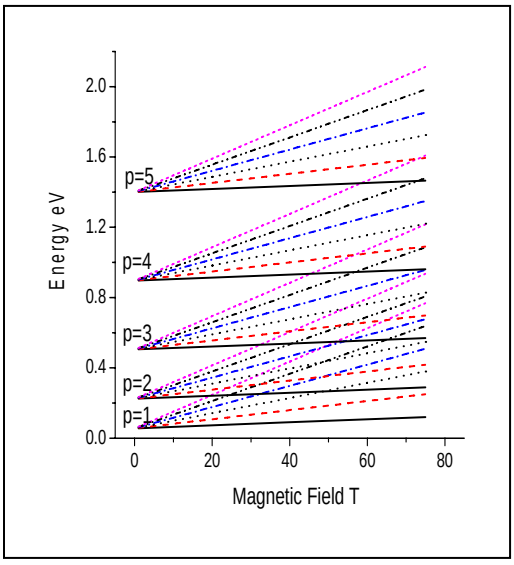

Fig. 6.2 Variation of energy versus magnetic field for different values of Landau levels (n) with different values of size quantization number (p).

We have taken $a = 1$, T=4.2K, and the Fermi energy, $E_F = 0.15eV$. The different values of the Bessel function used for different quantized values of the energy levels for geometrical confinement are given in table 6.1.

The variation of energy versus magnetic field for different values of Landau levels with the thin film thickness of the QD 10nm has been observed and presented in the Fig. 6.1. Similarly, the variation of energy versus magnetic field as that shown in the Fig. 6.1, with different values of size quantization number p ranging from 1 to 5, are also shown in Fig. 6.2.

The variation of the energy versus radius of the system formed by geometrical confinement structure is also studied and presented in Fig. 6.3 and 6.4. The curves in the Fig 6.3 are plotted for various Bessel function values, whereas the curves in Fig. 6.4 is plotted to show the variation of energy versus radius as that of the Fig. 6.3 for different values of size quantization number (p).

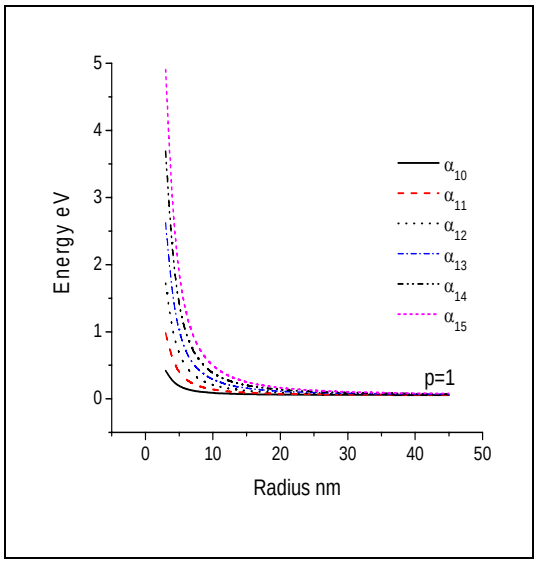

Fig. 6.3: Variation of energy versus radius in geometrically confined structure for various values of Bessel functions.

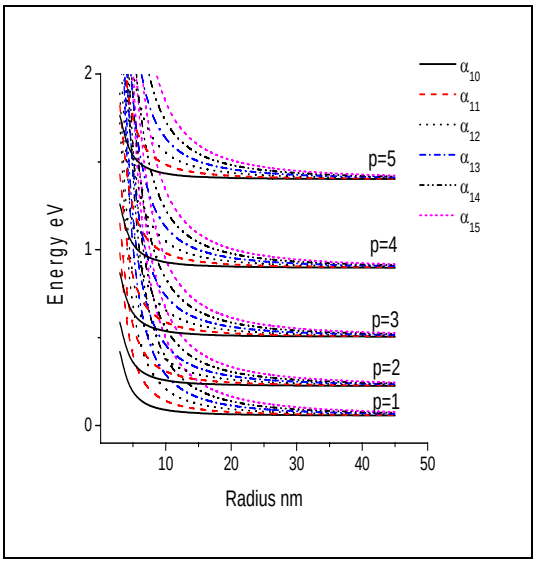

Fig. 6.4: Variation of energy versus radius in geometrically confined structure with various values of Bessel functions for different values of size quantization number (p).

The relation between the magnetic field, used for magnetically confined structure and the corresponding radius of curvature used for geometrically confined structure for the lowest Landau level are shown in Fig. 6.5.

Fig. 6.6 shows the variation of the energy versus the inverse of magnetic field for the magnetically confined structures.

Variation of energy versus inverse of square of magnetic field for the magnetically confined dot for different Landau levels (n) of confined dot with the different values of size quantization number (p) is shown in Fig. 6.7.

Fig. 6.8 shows the variation of energy versus radius for geometrically as well as the magnetically confined dot for different values of the thickness of the thin film. The Fig. 6.8 shows that the effect of dimensionality of the energy disappears as the radius increases for both magnetically and geometrical confinements.

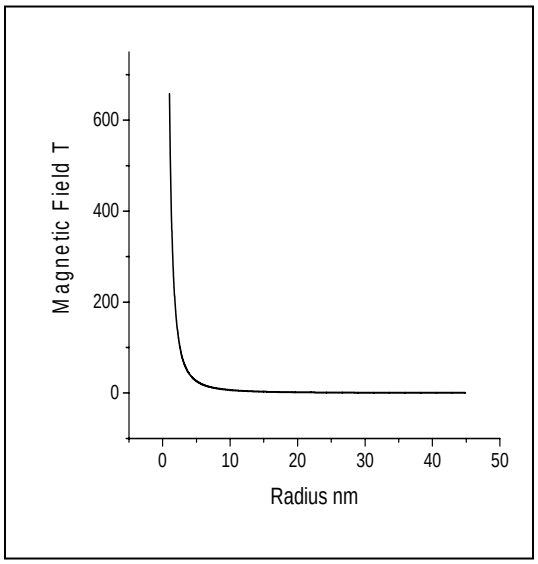

Fig. 6.5 Variation of the applied magnetic field versus radius for the lowest Landau level i.e. n=0.

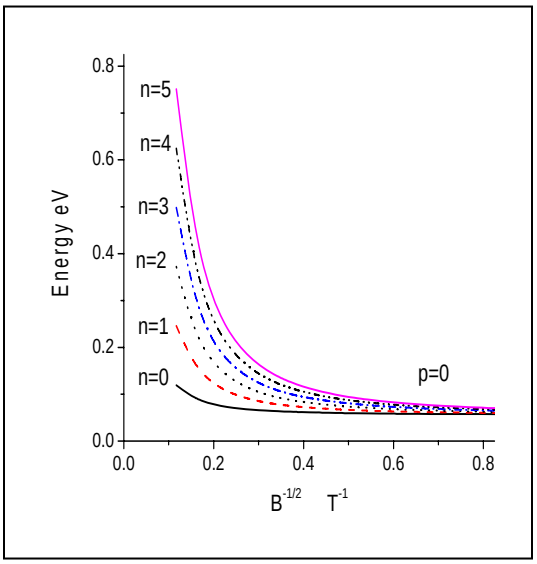

Fig. 6.6 Variation of energy versus inverse of square root of magnetic field in magnetically confined dot for different Landau levels.

The variation of PE current density versus photon energy for 20 nm thick thin film and 20 nm the radii of magnetically and geometrically confined cylindrical QD are shown in Fig. 6.9 and 6.10 respectively. The variations are found to be step like in the nature due to the contribution of various quantized energy levels. Electrons from more and more quantized levels take part in photo emission process as there is more photon energy incident.

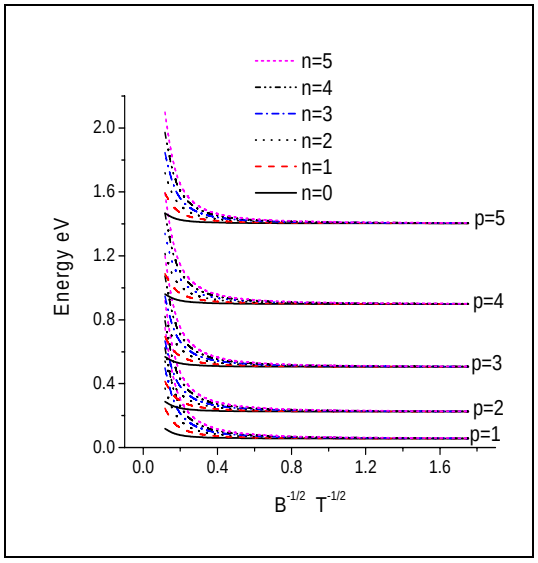

Fig. 6.7 Variation of energy versus inverse of square root of magnetic field in magnetically confined dot with different Landau levels (n) for different values of size quantization number (p).

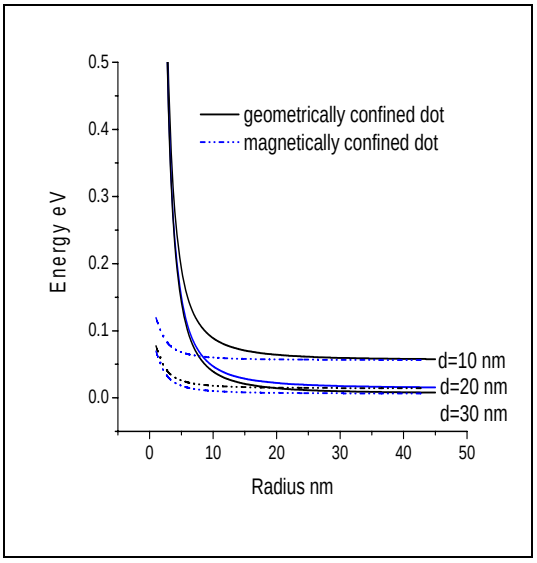

Fig. 6.8: Variation of energy versus radius for geometrically confined and magnetically confined dot for different thickness (d) of the thin films.

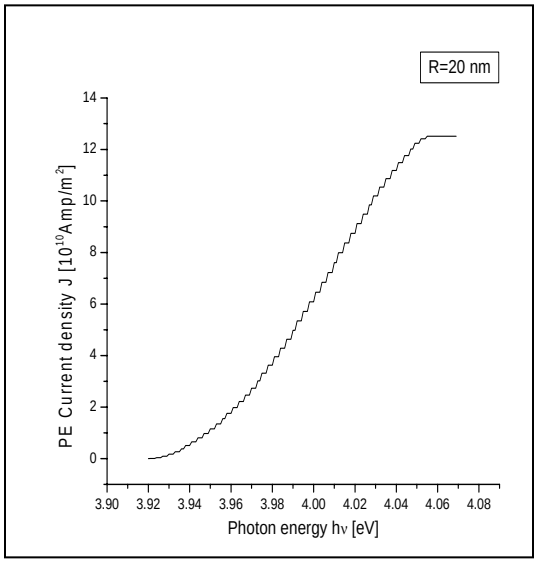

Fig. 6.9 Variation of PE current density versus photon energy for magnetically confined cylindrical QD with thickness 20nm and radius 20nm.

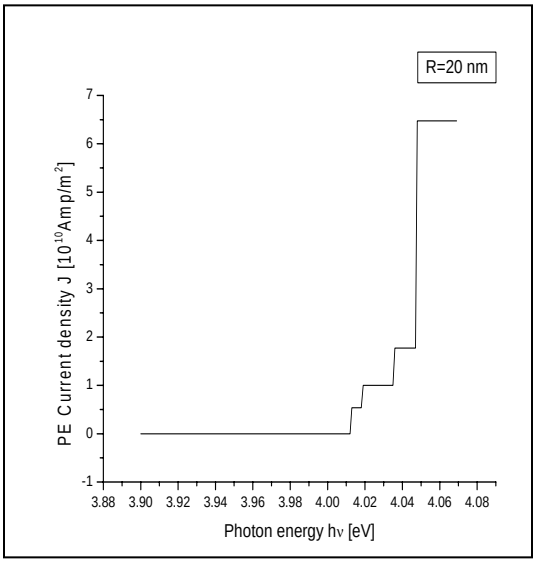

Fig. 6.10 Variation of PE current density versus photon energy for geometrically confined cylindrical QD with thickness 20nm and radius 20nm.

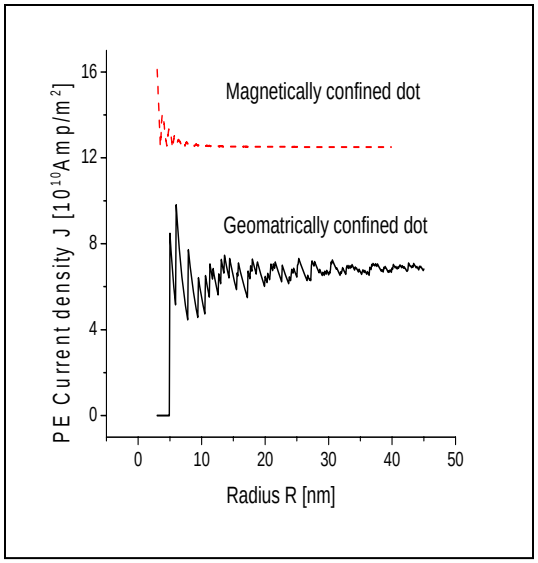

6.11 Variation of photoelectric current density with radius of magnetically and geometrically confined cylindrical QD, with thickness 20 nm and photon energy is taken as 4.07 eV

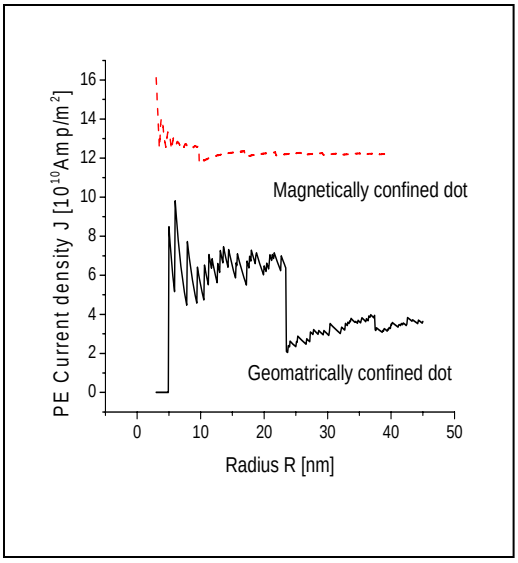

6.12 Variation of photoelectric current density with radius of magnetically and geometrically confined cylindrical QD, with thickness 10 nm and photon energy is taken as 4.07 eV.

Very small steps are found in the case of magnetically confined system, whereas, large steps are found in the case of geometrically confined QD due to the step sizes being directly related to separation between successive energy levels.

For a particular incident of photon energy 4.07eV, the variations of the PE current density with radius for the thickness 20 nm of QD of both geometrically as well as magnetically confined systems is shown in Fig. 6.11. Similar variation as that shown in Fig. 6.11, for the thickness 10nm is shown in Fig. 6.12.

In both figures, we can see that for magnetically confined QD, PE current density gets almost saturated as radius is increased beyond 10nm. But for geometrically confined QD it is oscillatory in nature, this oscillation decays as the radius of the curvature increases.

The PE current density with the modified DOS in the presence of broadening has been calculated as a function of the incident photon energy in the transverse dimension of QWW of n-GaAs for the different values of the broadening parameter (Δ). The idea is to investigate the effect of energy

level broadening on the PE current density. It is found that the broadening of the Landau levels results the reduction in the PE emission.

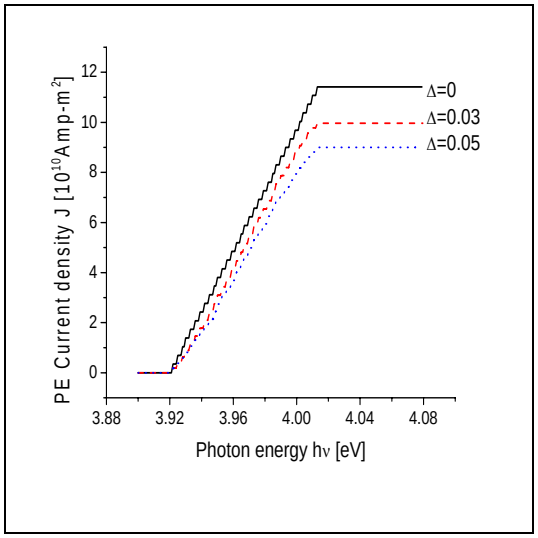

6.13 Variation of PE current density with incident photon energy of magnetically confined QD, with and without broadening (Δ=0, 0.03 eV, 0.05 eV) for the thick 20 nm.

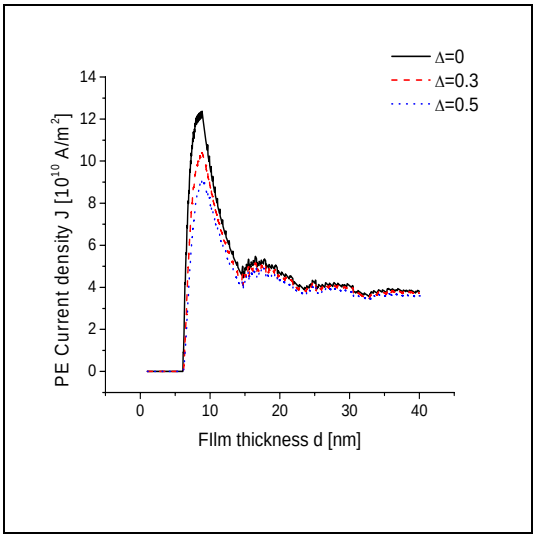

6.14 Variation of PE current density with the thickness of magnetically confined QD, with and without broadening (Δ=0, 0.03 eV, 0.05 eV) and photon energy being 4.07 eV.

The variation of the PE current density with incident photon energy is shown in Fig. 6.13. The emission is found to be increasing with photon energy in steps, as expected. Finally, it is found to be saturated for an energy at which all electrons occupy the lowest energy level of the system and can participate in emission process. Similarly, Fig. 6.14 shows the variation of the photoelectric current density with the film thickness taking broadening of the Landau levels with various broadening parameters. The PE current density has been found to oscillate with the film thickness. It is found that the PE emission starts at about 6 nm of film thickness, attains a peak value at d=8 nm, and finally assumes a steady value through small oscillations. It is also observed that the current densities are found to be decreasing with increasing value of broadening parameter.

Fig. 6.15 shows the variation of the PE current density as a function of incident photon energy for no broadening and with broadening i.e. Δ=0, 0.03 eV, 0.05 eV. The broadening diminishes the level of PE current due to enhancement of scattering. PE current density variations with and without broadenings are similar, i.e. step in the nature. This is the consequence of

1DEG formed due to quantization in QWWs. Furthermore, it is also noted that the PE current density starts from the same photon energy for $\Delta = 0$ and 0.03eV. However, the Fermi level reduces further from 0.15eV when broadening is included. Hence, the highest subband contribution to the PE current density for $\Delta = 0.03eV$ is higher than that of the broadening with $\Delta = 0.05eV$. Therefore, the PE current density starts from the next lower subband for the higher value of broadening parameter.

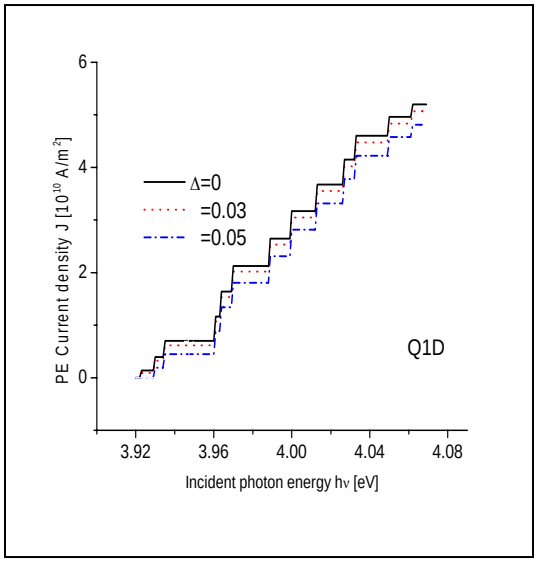

Fig. 6.15 Variation of photoelectric current density with incident photon energy of geometrically confined Q1D system, with and without broadening (Δ=0, 0.03 eV, 0.05 eV).

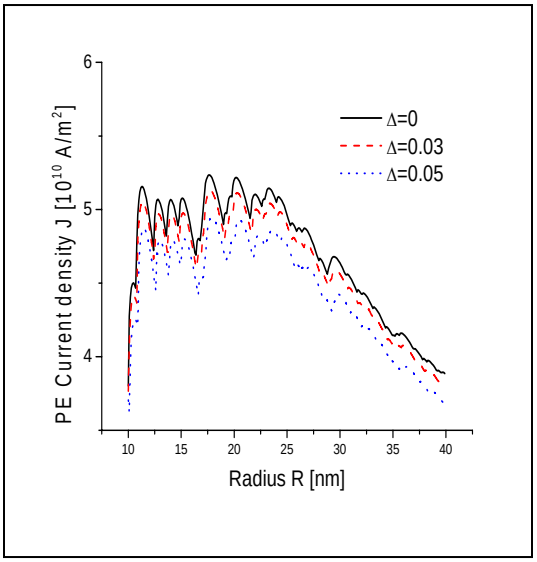

Fig. 6.16 Variation of photoelectric current density with radius of geometrically confined Q1D system, with and without broadening (Δ=0, 0.03 eV, 0.05 eV), the photon energy being 4.07 eV.

The dimensional dependence of the PE current density has been shown in Fig. 6.16. The variation of the current density versus the wire radius is shown in the Fig. 6.16 for various broadening parametric values, Δ=0, 0.03 eV, 0.05 eV. The variation of PE current density is found to be oscillatory in nature following the similar periodicity both in the absence as well as in the presence of broadening. The predominance of broadening appears when the dimension of the system decreases. The Fig 6.16 shows that the energy level broadening decreases the magnitude of the PE current density. Similar results have been reported earlier in the case of geometrically confined quasi-two-dimensional system [Mutsuddi, Bose and Sarkar, 2004].

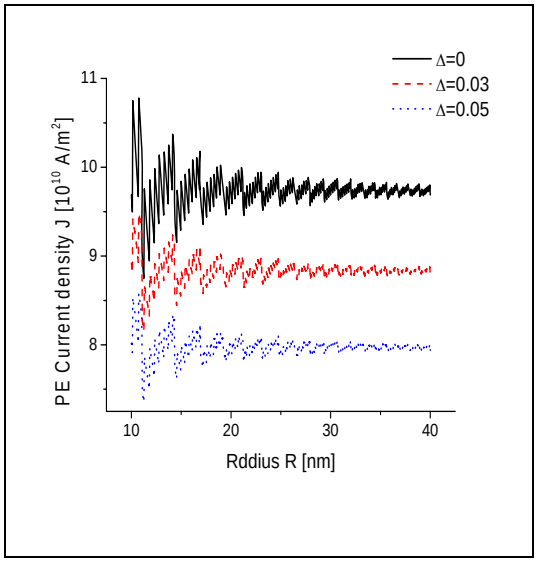

Fig. 6.17 Variation of PE current density with radius of magnetically confined QD, with and without broadening (Δ=0, 0.03 eV, 0.05 eV) the photon energy being 4.07 eV.

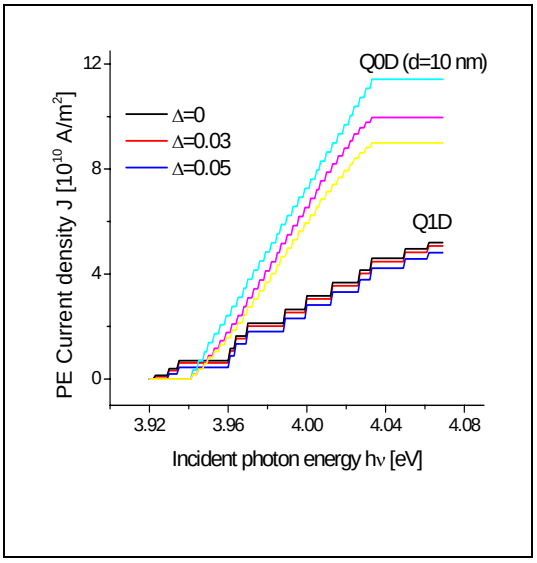

Fig. 6.18 Variation of photoelectric current density with incident photon energy of geometrically confined GaAs QWW and magnetically confined GaAs QD, with and without broadening (Δ=0, 0.03 eV, 0.05 eV).

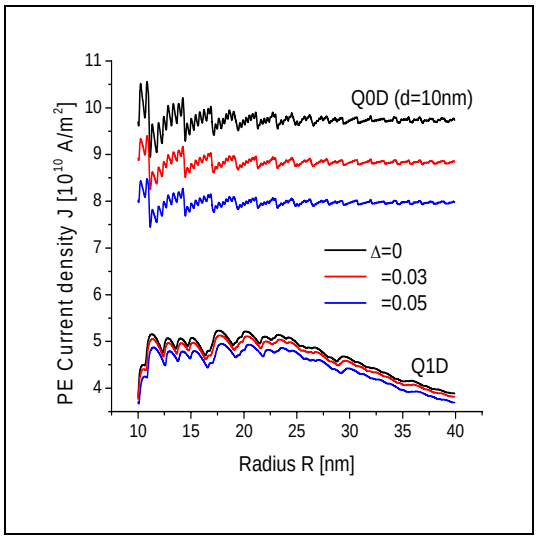

Fig. 6.19 Variation of photoelectric current density with radius of lowest Landau level magnetically confined GaAs QD and geometrically confined GaAs QWW, with and without broadening (Δ=0, 0.03 eV, 0.05 eV) and photon energy being 4.07 eV.

The oscillatory nature of variation of the PE current density as a function of the radius of the lowest Landau level is shown in Fig. 6.17, for magnetically confinement system, for both the presence and absence of broadening. The Fig. 6.17 shows that the magnetic quantization number of the highest occupied energy level causes more oscillations. The abrupt fall in PE emission occurs due to change in size quantization number of the highest occupied energy levels. Landau level broadening also causes similar reduction in the magnitude of the current density, but the oscillatory nature however remains almost same.

The comparative studies between the magnetically confined and geometrically confined systems are also done.

Fig. 6.18 shows the comparative variation of the current density with incident photon energy of GaAs QWW and magnetically confined QD. It can be seen that Q0D current density is increasing with photon energy in small steps and greater slope than Q1D. For Q1D, PE emission starts at lower photon energy, but finally the current density assumes only about half of the value achieved in the case of Q0D. As it is clear from the figure, the reduction in the current density due to broadening is more pronounced in Q0D than Q1D.

Fig. 6.19 shows the comparative variation of current density with the radius of QWW and QD. As QD is magnetically confined, here radius is of the lowest Landau level. The Fig. 7.19 shows that for the same radius of the QD and QWW, the PE current density in QD is much higher than QWW and is expected due to the higher degree of carrier confinement. The effect of broadening on PE emission is also more prominent in QD.

6.4 Conclusions

The energy is found to be increasing with the increase in the Landau level as well as with the magnetic field in the case of magnetically confined Q1D and also for QD system.

The energy in the case of geometrical confinement is observed to be decaying with the higher values of the radius of the QWW.

The energy is found to be higher in the case of geometrically confined dot as compared to that of the magnetically confined dot at lower values of the

radius of QWW. The dimensionality of the energy value disappears in the higher values of the radius in both the cases of quantization.
The PE current density versus photo electric incident energy is observed to be step in the nature in both the cases of quantization but the height of the step is found to be large as well as irregular in the case of geometrical confinement.

Finally, the broadening of the quantized energy levels due to the presence of impurities and imperfection in the real systems is observed.

The PE curve density is found to be oscillating in the nature with the incident photon energy both in the presence and in the absence of the broadening in both the cases of quantization.

Also, the nature of the oscillation is similar with as well as without broadening, but the magnitude of the photo electric current density is observed to be reduced due to the presence of the broadening in both the cases of quantization.

Reference

Adachi S., J. Appl. Phys. 58, 2911 (1985).
Arch D.K., Wick G. and Tonane T., J. Appl. Phys. 58, 3933 (1985).
Arora V.K. and Prasad M., Phys. Stat. Sol (b) 117 (1983).
Ando T., Fowler A. B. and Stern F., Rev. Mod. Phys. 54, 437 (1982).
Blakemore J.S., Semiconductor statistics, Dover, New York (1962).
Das P.K., Bose C., Shrestha S. & Sarkar C.K., Proceeding of International conference on Communications, Devices and intelligent Systems, pg.381 (CODIS 2004)
Jog S.D. and Wallace P. R., J. Phys. C 8, 3608 (1975).
Landau L.D., S. Physik 64, 629 (1930).
Majumdar C., Maity A.B. and Chakravarti A.N., Phys. Stat. Sol. (b) 140, K7 (1987).
Mutsuddi I., Bose C. and Sarkar C.K., Phys. Stat. Sol. (b) 241, 1053-1057 (2004)
Ploog K., Crystal Growth, Properties and Applications, ed. H. Freyhardt, Springer-Verlag, Berlin and New York (1980).
Roth L.M. and Argyres P. N., Seemiconductors ans Semimetals, ed. R.K. Willardson and A.C. Beer, 1, 159 (1966).
Vander Ziel A., Solid State Physical Electronics, Prentice Hall, New Jersy, (1957).

The roots of Bessel function: Table 6.1

α_{ml}	m=**1**	**2**	**3**	**4**	**5**	**6**	**7**	**8**	**9**	**10**
l=**0**	2.40	5.52	8.65	11.79	14.93	18.07	21.21	24.35	27.49	30.63
1	3.83	7.02	10.17	13.32	16.47	19.62	22.76	25.90	29.05	32.19
2	5.14	8.42	11.62	14.80	17.96	20.12	24.27	27.42	30.57	33.72
3	6.38	9.76	13.02	16.22	19.41	22.58	25.75	28.91	32.06	35.22
4	7.59	11.06	14.37	17.62	20.83	24.02	27.20	30.37	33.54	36.70
5	8.77	12.34	15.70	18.98	22.22	25.43	28.63	31.81	34.99	38.16
6	9.94	13.59	17.00	20.32	23.59	26.82	30.03	33.23	36.42	39.60
7	11.09	14.82	18.29	21.64	24.93	28.19	31.42	34.64	37.84	41.03
8	12.23	16.04	19.55	22.95	26.27	29.55	32.90	36.03	39.24	42.44
9	13.35	17.24	20.81	24.23	27.58	30.89	34.15	37.40	40.63	43.84
10	14.48	18.43	22.05	25.51	28.89	32.21	35.50	38.78	42.00	45.23
11	15.59	19.62	23.28	26.77	30.18	33.53	36.83	40.12	43.37	46.61
12	16.70	20.79	24.49	28.03	31.46	34.83	38.16	41.45	44.72	47.97
13	17.80	21.96	25.71	29.27	32.73	36.12	39.47	42.78	46.07	49.33
14	18.9	23.12	26.91	30.50	33.99	37.41	40.77	44.10	47.40	50.68
15	19.99	24.27	28.10	31.73	35.25	38.68	42.07	45.41	48.73	52.02
16	21.09	25.42	29.29	32.95	36.49	39.95	43.36	64.72	50.04	53.35
17	22.17	26.56	30.47	34.17	37.73	41.21	44.63	48.01	51.36	54.67

Conclusions

Bulk material such as GaN is a very important material in the electronic devices due to its large band gap and strong bond strength. The problem of using GaN material is that it is not available in a single crystal form. So it has to be grown on some substrates such as sapphire, with a large lattice mismatch causing very high density of dislocations to be present in the interface, a layer between GaN and the substrate. Hence, we have applied Look's two-layer model to calculate various electronic and thermal transport parameters such as mobility, Seebeck coefficient, thermal conductivity due to electrons and the thermoelectric figure of merit and compared our results with experimentally available data which are found to be satisfactory also. However, the thermal conductivity due to lattice is calculated by using Callaway's Phenomenological theory.

We have also calculated the ac microwave mobility variation with temperatures and frequency of the bulk GaN, grown on a substrate as sapphire due to the higher utility of microwave devices in fast communication and amplification.

The effect of phonon scattering mechanisms such as acoustic phonon via deformation potential, piezoelectric and polar optical phonon scattering and nonphonon scattering mechanisms such as ionized impurity and neutral impurity scattering mechanisms on the above parameters are also observed. The presence of large dislocations causing the scattering due to dislocations to be dominant in the interfacial layer is also included in our calculations.

The characteristic properties of device systems formed by spatial quantization as Q2D and Q1D systems formed on the heterojunctions of GaAs/AlGaAs and GaInAs/InP systems are also observed. The effects of quantization on the dc and ac mobilities of the systems are calculated and compared. It is found that the mobility of Q1D system is much more improved as compared to that of the Q2D system. It is expected due to the less scattering mechanisms and the quantization of one more dimension of energy relation in the case of Q1D system as compared to that of Q2D.

Due to a perfect latticed matched interface at the heterojunction there would be no dislocations at the interface. However, we have also drawn our attention on the surface roughness scattering mechanism in both the Q2D and Q1D systems apart from other phonon scattering mechanisms, such as

acoustic phonon via deformation potential and piezoelectric scattering mechanisms and nonphonon scattering mechanisms, such as ionized impurity, both back ground and remote. Similarly, due to GaInAs, a ternary-alloy semiconductor we have also included the alloy disorder scattering mechanism in the material.

Realizing to the importance of Q1D transport for high mobility devices we have also included Q1D system formed by magnetic quantization of energy levels on a semiconductor system and the behavior of the system in the presence of temperature gradient along the magnetic field. Under the situation the system behaves as quasi one dimensional (Q1D) system.

MCT being a narrow band gap semiconductor, the band structure is found to be nonparabolic in nature. In keeping the recent report of Chen and Sher the hyperbolic band structure is also included along with nonparabolic and parabolic band structures in our calculations. The effect of the band structures on the various electric and thermal transport properties, such as conductivity, Seebeck coefficient, thermal conductivity due to electron and the figure of merit of the material is observed. However, the thermal conductivity due to lattice is calculated taking the phonon boundary scattering.

Selection of MCT for thermoelectric devices is due to its low effect mass also. The low effective mass enhances the mobility and reduces the Joules heating, which is an inherent property needed for such types of devices such as cooler, refrigerator etc.

The effect of various scattering mechanisms such as acoustic phonon via potential deformation, piezoelectric phonon, ionized impurity, alloy disorder and polar optical phonon scattering mechanisms on the above transport parameters is also observed in the case of Q1D MCT system.

The effects of degeneracy arising due to the presence of dense concentration of the carries on the Q1D MCT system and their effect on the transport parameters are also observed. The magnetic field and temperature dependent such transport parameters are found to be very interesting.

Finally, the utility of the low dimension devices in optoelectronics area is also observed, taking consideration of QWW and QD formed in GaAs. The photo electric (PE) current density of the systems is calculated with theoretical

model of magnetically confined Q1D and Q0D systems. For magnetically confined Q0D system, the thickness of the sample is taken equal to that of the deBroglie wavelength or lesser than that, the method is called the magnetic size quantization.

We have also considered a geometrically confined system with the dimensions exactly as that of the magnetically confined system and observed the PE current density of the system too. The values of photo electric emission due to the two systems in both types of confined mechanisms are also compared.

Due to the practical limitations, the presence of impurities and imperfections in Q1D and Q0D systems, quantized energy levels get broadened. The broadening of the quantized energy levels on the photoelectric emission of the system also is observed. The effect of the broadening on the photo emission properties of the materials are also observed and presented in our work.

Future Scopes

High electric field i.e. hot electron transport can be studied in the case of n-GaN grown on sapphire, considering two-layer model.

Different transport phenomena, such as conductivity, mobility, Seebeck coefficient and the thermoelectric figure of merit can be studied in the heterojunction of GaN and related materials.

The various transport phenomena as mentioned above can be studied in the case of n-GaN grown on sapphire, considering two-layer model in the presence of high magnetic field, forming quasi-one dimensional electron gas (1D EG).

The thermoelectric figure of merit of heterojunctions formed by AlGaAs/GaAs and GaInAs/InP can be calculated.

High frequency ac conductivity of MCT, in the presence of high magnetic field can be investigated.